

Nanolaminate Coatings to Improve Long-Term Stability of Plasmonic Structures in  
Physiological Environments

Monisha Gnanachandra Daniel

Thesis submitted to the faculty of the Virginia Polytechnic Institute and State University  
in partial fulfillment of the requirements for the degree of

Master of Science  
In  
Electrical Engineering

Wei Zhou, Chair  
Michael S. Hsiao  
Daniel J. Stilwell

May 9, 2017  
Blacksburg, VA

Keywords:  $\text{Al}_2\text{O}_3$  /  $\text{HfO}_2$  Nanolaminate Coatings, Atomic Layer Deposition, Plasmonics,  
In-situ Testing, Stability Improvement

Copyright 2017 Monisha Gnanachandra Daniel

# **Nanolaminate Coatings to Improve Long-Term Stability of Plasmonic Structures in Physiological Environments**

Monisha Gnanachandra Daniel

## **ABSTRACT**

The unprecedented ability of plasmonic metal nano-structures to concentrate light into deep-subwavelength volumes has propelled their use in a vast array of nanophotonics technologies and research endeavors. They are used in sensing, super-resolution imaging, SPP lithography, SPP assisted absorption, SPP-based antennas, light manipulation, etc. To take full advantage of the attractive capabilities of CMOS compatible low-cost plasmonic structures based on Al and Cu, nanolaminate coatings are investigated to improve their long-term stability in corrosive physiological environments. The structures are fabricated using phase-shifting PDMS masks, e-beam deposition, RIE, Atomic Layer Deposition and Rapid Thermal Annealing. An alternate approach using Nanosphere Lithography (NSL) was also investigated. Films were examined using ellipsometry, atomic force microscopy and transmission measurements. Accelerated in-situ tests of  $\text{HfO}_2/\text{Al}_2\text{O}_3$  nanolaminate shells in a mildly pH environment with temperatures akin to physiological environments emulated using PBS show greatly enhanced endurance, with stable structures that last for more than one year.

# **Nanolaminate Coatings to Improve Long-Term Stability of Plasmonic Structures in Physiological Environments**

Monisha Gnanachandra Daniel

## **GENERAL AUDIENCE ABSTRACT**

When light (electromagnetic radiation) interacts with the free (conduction) electrons of a metallic nanostructure it leads to a coupling resulting in collective excitations (oscillations) that lead to strong enhancements of the local electromagnetic fields surrounding the nanoparticles, this phenomenon is called Localized Surface Plasmon Resonance (LSPR) and plasmonics are structures that are capable of exhibiting this phenomenon. The condition for LSPR to occur is that the dimension scale of the structure is less than the wavelength of the electromagnetic radiation interacting with it. This implies that the structure has to be in nanoscale dimensions. LSPR based plasmonic structures are compact, sensitive and can be integrated with electronic devices and can be used in various applications like implantable biological sensors (blood pH sensing, diabetics sensing, etc.), devices that integrate several laboratory testing functionalities on a single chip, studies to determine the dynamics of chemical reactions, increasing the efficiency of solar power generation, etc. LSPR is exhibited by metallic nano-particles like gold, silver, copper and aluminum. Metals like copper corrode at a rapid rate in water at room temperature and hence nano scale structures made from them that can exhibit LSPR cannot be used in higher temperature ionic environments without a protective coating. High density, uniform coatings with less defect density can be deposited using Atomic layer deposition (ALD). In this research Atomic Layer Deposited Aluminum Oxide and Hafnium Oxide nanolaminate structures are explored to increase the long-term stability of plasmonic structures in physiological solutions. In-situ tests are carried out in a Phosphate-buffered Saline (PBS) solution with a pH value of 7.2 (simulating physiological conditions) at a temperature of 37°C (physiological temperature) and 85.1°C (accelerated testing). The results demonstrate that the dielectric nano coatings investigated in this project can increase the stability of the plasmonic structures in the corrosive physiological environment from a few days to more than one year.

## **Acknowledgements**

I would like to thank my advisor, Dr. Wei Zhou for his direction, constant support, encouragement, feedback and patience through this endeavor. I also thank him for being a role model to me in work ethics and perseverance. I would also like to thank Dr. Michael Hsiao and Dr. Daniel Stilwell for graciously serving on my thesis committee. Last, but not the least by any means, I would like to thank my friends (especially Joshua Christopher and Balakrishnan Sambathkumar, who have been my pillars of support) and family who have made my stay at graduate school enjoyable and the people in my research group especially Junyeob Song who was my collaborator for fabrication and Seied Ali Safiabadi Tali who was my collaborator for Raman measurements, it was a great pleasure knowing these nice people and working with them.

## Table of Contents

	Acknowledgements.....	iv
	Table of Contents.....	v
	List of Figures.....	vi
	List of Tables.....	x
1	Introduction.....	1
	1.1 Plasmonics.....	1
	1.2 Background and Significance.....	4
2	Hypothesis.....	16
3	Methodology.....	21
	3.1 Initial Testing.....	21
	3.2 Ellipsometry Data- Fit Improvement.....	26
	3.2.1 Slow Annealing.....	28
	3.2.2 General Oscillator (GenOsc) Method.....	34
	3.2.3 Accounting for Surface Roughness.....	35
	3.3 Filmetrics Measurements.....	39
	3.4 Raman Spectroscopy.....	40
	3.5 Thin Film Stability Test.....	42
4	Fabrication.....	44
	4.1 Self-Assembly Process: Nano-Sphere Lithography (NSL).....	44
	4.2 Top-down approach: Using E-Beam Deposition.....	49
5	Testing.....	57
6	Results and Discussion.....	61
	6.1 Dark Current.....	61
	6.2 Pure Cu 1X PBS Test.....	62
	6.3 Initial Transmission Measurements.....	63
	6.4 Effect of Annealing Temperature.....	64
	6.5 Effect of Sample Composition.....	69
	6.6 Effect of Coating Thickness.....	72
7	Conclusion.....	74
8	Future Work.....	76
	References.....	78
	Citations of Copyrighted Works.....	82

## List of Figures

### Chapter 1. Introduction

- Figure 1** (a) SPP, which is the collective interaction between free charges on a metal surface and electromagnetic fields and (b) evanescent field of an SPP surface-bound wave. ( $\delta_d$ =Skin depth of dielectric,  $\delta_m$ =Skin depth of metal). B. Lee et al., “The use of plasmonics in light beaming and focusing”, *Progress in Quantum Electronics* 34 (2010) 47–87. Used under fair use, 2017.....3
- Figure 2** The dispersion relation of the free electron gas. Electromagnetic wave propagation is allowed only for  $\omega > \omega_p$ . Stefan A. Maier, “Plasmonics: Fundamentals and Applications”, Published in 2007. Used under fair use, 2017..... 4
- Figure 3** (a) Schematic representation of a SPP biosensor, and (b) SPP resonance dependence on molecular concentration. Dragoman, “Plasmonics: Applications to nanoscale terahertz and optical devices, *Progress in Quantum Electronics* 32 (2008) 1–41. Used under fair use, 2017.....5
- Figure 4** Moore’s Law over the years. M. Mitchell Waldrop, “The chips are down for Moore’s law”, *Nature News*, Nature Publishing Group, Feb 9, 2016. Used with permission from Nature Publishing Group. License attached.....7
- Figure 5** Schematic representation of surface plasmon polaritonic lithography. Luo, et al., “Surface plasmon resonant interference nanolithography technique”, *Applied Physics Letters*, Vol. 84, No. 23, 7 June 2004. Used under fair use, 2017.....8
- Figure 6** Basic principle behind LSPR based sensors for detection of a particular molecule (analyte). Ramaccia, et al., “Core-shell super-spherical nanoparticles for LSPR-based sensing platforms”, *iee journal of selected topics in quantum electronics*, Vol. 23, No. 2, March/April 2017. Used under fair use, 2017.....9
- Figure 7** Parallel monochromatic-illumination-based refractive index sensing in multiple nanochannels. Joachim Fritzsche et al., *Nano Letters* 2016, 16, 7857–7864. Used under fair use, 2017.....10
- Figure 8** Textured silicon solar cell. Wen-Jeng Ho, et al., “Performance-Enhanced Textured Silicon Solar Cells Based on Plasmonic Light Scattering Using Silver and Indium Nanoparticles”, *Materials* 2015, 8(10), 6668-6676. Used under fair use, 2017.....10
- Figure 9** Optical microscope image of copper after 5.3 days of corrosion in 22 °C water. Yersak, et al., “Characterization of Thin Film Dissolution in Water with in Situ Monitoring of Film

Thickness Using Reflectometry”, ACS Applied Materials & Interfaces, 2016, 8, 17622–17630. Used under fair use, 2017.....12

**Chapter 2. Hypothesis**

**Figure 10** Comparison of step coverage of CVD, ALD and PVD.....17

**Figure 11** Etch rate comparison of Al<sub>2</sub>O<sub>3</sub>, HfO<sub>2</sub> and the Nanolaminate structure in BOE..... 19

**Chapter 3. Methodology**

**Figure 12** J.A.Woollam Co., Inc. Variable Angle Spectroscopic Ellipsometer (VASE) used in the project.....21

**Figure 13** Bare Silicon Characterization using ellipsometry.....22

**Figure 14** Coating Profile.....23

**Figure 15** Chamber Pressure Curves during ALD.....24

**Figure 16** Thin Film Characterization Annealing Recipes and Graphs.....25

**Figure 17** Slow Annealing Recipes and Graphs.....33

**Figure 18** Ellipsometry MSE improvement: GenOsc Model with three Oscillators for Pure Al<sub>2</sub>O<sub>3</sub> annealed at 900°C..... 35

**Figure 19** Graphical Summary of Thin Film Characterization results using Ellipsometry.....37

**Figure 20** Filmetrics Measurement of pure Al<sub>2</sub>O<sub>3</sub> annealed at 150°C.....39

**Figure 21** Raman Spectroscopy data showing crystallization state of the samples.....41

**Figure 22** Preliminary Results after soaking in 10X PBS at 37°C for 7 days. Dashed line indicates initial film thickness.....43

**Figure 23** Preliminary Results after soaking in 10X PBS at 37°C for 7 days. Dashed line indicates initial refractive index.....43

**Chapter 4. Fabrication**

**Figure 24** Nanoscale characteristics of the main lithographic techniques in the top-down approach. Dragoman, “Plasmonics: Applications to nanoscale terahertz and optical devices, Progress in Quantum Electronics 32 (2008) 1–41. Used under fair use, 2017..... 44

**Figure 25** General Schematics of NSL. “Nanoparticle fabrication by geometrically confined nanosphere lithography”, J. Micro/Nanolith. MEMS MOEMS. 12(3), 031106 (Jul 26, 2013). Used under fair use, 2017.....45

<b>Figure 26</b> Initial attempts showing multilayer formation instead of the desired mono-layer PS mask.....	46
<b>Figure 27</b> 20X magnification microscope image of uniform PS mask distribution.....	47
<b>Figure 28</b> Schematics of the HCL fabrication scheme.....	48
<b>Figure 29</b> SEM Images of deposited Polystyrene beads. (a) 11.2 KX magnification image showing formation of crack in the substrate upon etching due to insufficient curing of the substrate, it was fixed by hard baking after SU8 coating at 180°C for 5 minutes. (b) 40.62 KX magnification of PS deposited on substrate (c) and (d) 5.01 KX magnification images of PS distribution (c) shows formation of a cluster, (d) shows fairly uniform distribution.....	49
<b>Figure 30</b> Schematics of the Fabrication Process using e-beam deposition.....	51
<b>Figure 31</b> Fabricated samples soaked in chrome etchant 1020. It can be seen that some Gold nanohole array masks are detached from the substrate .....	52
<b>Figure 32</b> 112.52KX magnification SEM image of Fabricated Hole Mask Array.....	53
<b>Figure 33</b> (a) Samples taped to the chuck to be mounted for e-beam deposition of Cu. (b) Samples mounted inside the e-beam chamber for deposition. The Cu crucible is mounted in the bottom of the chamber. (c) Copper coated samples before tape-out.....	54
<b>Figure 34</b> Fabricated sample in a petri dish. The plasmonic structure is located in the transparent looking square in the center, where the Au nano hole array mask has been removed. The area exhibits diffraction under light.....	54
<b>Figure 35</b> Cambridge Nano Tech’s Savannah ALD software screen used for programming and monitoring the deposition process. Al <sub>2</sub> O <sub>3</sub> deposition is shown here.....	56
<b>Figure 36</b> Recipe and Graph for Annealing at 250°C.....	56

**Chapter 5. Testing**

<b>Figure 37</b> Samples undergoing accelerated aging at higher temperatures in an incubator.....	58
---	----

**Chapter 6. Results and Discussion**

<b>Figure 38</b> Test set-up (a) Test set-up showing the light source, microscope and spectrometer. (b) Measurement of samples affixed to petri-dish immersion microscope.....	59
<b>Figure 39</b> Sample dark current measurement.....	61
<b>Figure 40</b> Copper real-time transmission measurements and graphical summary of the measurement. (a) Real-time Cu transmission measurement at 0 hour, 2 hours and 1 day.	

(b) Graphical representation of the measured transmission values.....	62
<b>Figure 41</b> Initial normalized transmittance of samples.....	63
<b>Figure 42</b> Normalized extinction of pure $\text{Al}_2\text{O}_3$ annealed at different temperatures in 1X PBS solution at 37°C at various time intervals.....	64
<b>Figure 43</b> Normalized extinction of pure $\text{Al}_2\text{O}_3$ annealed at different temperatures in 1X PBS solution at 85.1°C at various time intervals.....	65
<b>Figure 44</b> Normalized extinction of pure $\text{HfO}_2$ annealed at different temperatures in 1X PBS solution at 37°C at various time intervals.....	66
<b>Figure 45</b> Normalized extinction of pure $\text{HfO}_2$ annealed at different temperatures in 1X PBS solution at 85.1°C at various time intervals.....	66
<b>Figure 46</b> Normalized extinction of $\text{Al}_2\text{O}_3$ and $\text{HfO}_2$ nanolaminate structure in 3 5 5 5 2 ratio annealed at different temperatures in 1X PBS solution at 37°C at various time intervals.....	67
<b>Figure 47</b> Normalized extinction of $\text{Al}_2\text{O}_3$ and $\text{HfO}_2$ nanolaminate structure in 3 5 5 5 2 ratio annealed at different temperatures in 1X PBS solution at 85.1°C at various time intervals.....	68
<b>Figure 48</b> Normalized extinction of different sample compositions annealed at 600°C in 1X PBS solution at 37°C at various time intervals.....	69
<b>Figure 49</b> Normalized extinction of different sample compositions annealed at 600°C in 1X PBS solution at 85.1°C at various time intervals.....	69
<b>Figure 50</b> Normalized extinction of different sample compositions annealed at 350°C in 1X PBS solution at 37°C at various time intervals.....	71
<b>Figure 51</b> Normalized extinction of different sample compositions annealed at 350°C in 1X PBS solution at 85.1°C at various time intervals.....	71
<b>Figure 52</b> Normalized extinction of samples of different thicknesses with $\text{Al}_2\text{O}_3$ and $\text{HfO}_2$ in 3 5 5 5 2 ratio annealed at 600°C in 1X PBS solution at 37°C at various time intervals.....	72
<b>Figure 53</b> Normalized extinction of samples of different thicknesses with $\text{Al}_2\text{O}_3$ and $\text{HfO}_2$ in 3 5 5 5 2 ratio annealed at 350°C in 1X PBS solution at 37°C at various time intervals,.....	73
<b>Figure 54</b> Normalized extinction of samples of different thicknesses with $\text{Al}_2\text{O}_3$ and $\text{HfO}_2$ in 3 5 5 5 2 ratio annealed at 350°C in 1X PBS solution at 85.1°C at various time intervals.....	73

## List of Tables

<b>Table 1</b>	Testing: Thin Film Characterization (16 samples).....	23
<b>Table 2</b>	Microscope Images of Samples.....	31
<b>Table 3</b>	20X Magnified Microscopic Images showing effect of Slow anneal and Rapid Anneal.....	34
<b>Table 4</b>	Ellipsometry fit improvement of Al <sub>2</sub> O <sub>3</sub> annealed at 900°C.....	36
<b>Table 5</b>	Ellipsometry Data Summary.....	36
<b>Table 6</b>	Sample Description.....	37
<b>Table 7</b>	Comparison of thickness measured using ellipsometry and Filmetrics.....	40
<b>Table 8</b>	Samples fabricated for testing in PBS solution. The numbers within parenthesis denote the label given to the sample.....	50
<b>Table 9</b>	Recipe for 150°C growth of Al <sub>2</sub> O <sub>3</sub> and HfO <sub>2</sub> by ALD.....	55
<b>Table 10</b>	Cu transmittance measurement data summary.....	63

# 1. Introduction

## 1.1. Plasmonics

At high frequencies the conduction electrons of metals are free to flow around while the relatively massive ions remain more or less stationary and hence metals act like plasma. A resonance frequency can be obtained by solving this in a plasma problem with incident electromagnetic waves. Below the resonance frequency, the waves oscillate slowly enough for the electrons to follow. Thus, the metal behaves as a good conductor because the currents that can be excited can properly cancel out the incident waves. However, above the resonant frequency, the inertia of the electrons prevents the electrons from oscillating in proper phase with the incident wave. Thus, the currents cannot be excited properly to eliminate the incident wave and now the wave can pass through the metal like it was a vacuum (a dispersive and lossy vacuum).

In general dielectric constant is a complex function of angular frequency  $\omega$  of the form

$$\epsilon(\omega) = \epsilon_1(\omega) + i\epsilon_2(\omega)$$

The imaginary part  $\epsilon_2$  of the dielectric function determines the amount of absorption inside the medium and the real part  $\epsilon_1$  determines the amount of polarization.

Using the dispersive relation of travelling waves

$$\omega^2 = \omega_p^2 + K^2 c^2$$

Where,

$\omega$  = Angular frequency

$\omega_p$  = Plasma frequency

$K$  = Wave vector

$c$  = Speed of light

Solving for the permittivity in the above equation assuming vacuum permeability ( $\epsilon_0$ ) it can be obtained

$$\epsilon = \epsilon_0 \left(1 - \frac{\omega_p^2}{\omega^2}\right)$$

Thus the equivalent permittivity in which plasmonic behavior is exhibited requires that the permittivity becomes negative below resonance and positive above resonance. The simplest geometry capable of sustaining a Surface Plasmon Polaritons (SPP) is an interface between a substance with positive real dielectric constant and a substance whose real part of dielectric constant  $\epsilon_1$  is negative (real part of the dielectric constant has to change sign across the interface). The requirement of metallic character implies that  $\text{Re}[\epsilon_1] < 0$ . Hence they are capable of sustaining SPP and exhibiting plasmonic behavior when the wavelength of the incident electromagnetic radiation is greater than the nano-metal's size. When light hits small noble metal nano-particles it can couple to its conduction electrons and confine the light. The fundamental physical excitation is called Plasmon and SPP can be defined as infrared or visible-frequency electro-magnetic waves, which travel along a metal-dielectric or metal-air interface. The wave involves both charge motion in the metal ("surface plasmon") and electromagnetic waves in the air or dielectric (polariton). The electromagnetic wave's field intensity decays exponentially with distance from the interface.

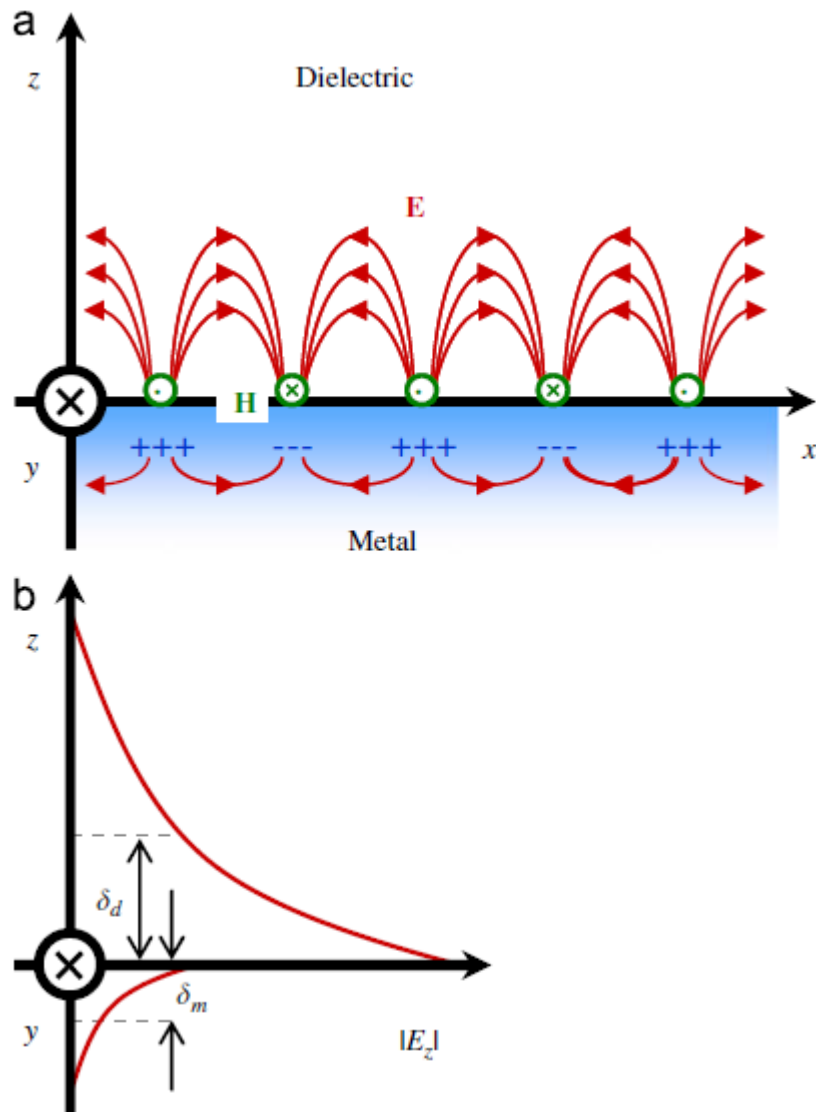


**Figure 1** (a) SPP, which is the collective interaction between free charges on a metal surface and electromagnetic fields and (b) evanescent field of an SPP surface-bound wave. ( $\delta_d$ =Skin depth of dielectric,  $\delta_m$ =Skin depth of metal). B. Lee et al., “The use of plasmonics in light beaming and focusing”, Progress in Quantum Electronics 34 (2010) 47–87. Used under fair use, 2017

In theory a number of metals like Li, Na, Al, In, Ga and Cu) meet the criterion for LSPR (a large negative real and a small imaginary dielectric function) and should support plasmon resonances for at least part of the UV-vis-NIR region [1] [2]. However, most of these metals are either unstable, difficult to work with, or prone to surface oxidation that can significantly affect the optical properties. There are few known metals which exhibit resonance in the visible region: Cu,

Au, Pd, Pt, and Ag. Au and Ag exhibit strong resonance, while Pd and Pt exhibit weak resonance. Cu exhibits good resonance properties, but is not stable due to formation of the surface oxides; the presence of copper oxides can greatly affect the LSPR [3]. Al exhibits resonance in the UV region. Plasmonic properties can be engineered by changing the particle size, shape (corner sharpness, geometrical shape), interparticle gaps, internal structure (crystallinity, hollow versus solid) and elemental composition (alloys, multi-metal core-shell structure) [4].

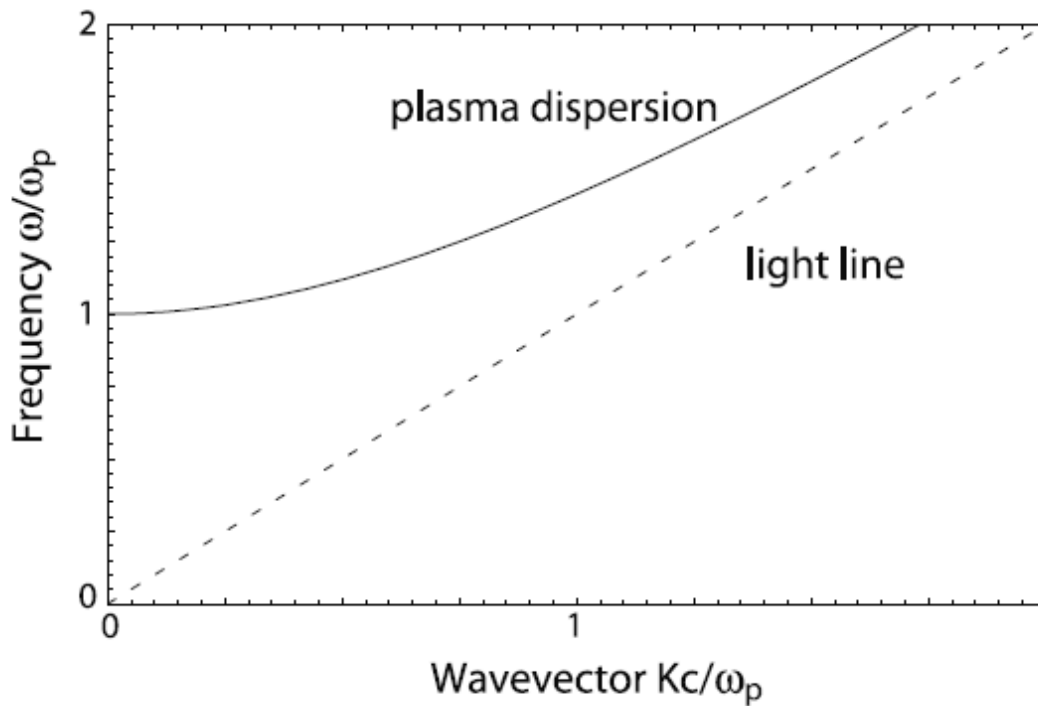


**Figure 2** The dispersion relation of the free electron gas. Electromagnetic wave propagation is allowed only for  $\omega > \omega_p$ . Stefan A. Maier, “Plasmonics: Fundamentals and Applications”, Published in 2007. Used under fair use, 2017

## 1.2. Background and Significance

Plasmonic metal nano-structures are used in a host of nanophotonics technologies and research activities due to their exceptional ability to concentrate light into deep-subwavelength volumes. They are used in applications such as sensing, super-resolution imaging, SPP lithography, SPP assisted absorption, SPP-based antennas, light manipulation, etc. In this project nanolaminate

coatings to improve the long-term stability of Cu plasmonic structures in corrosive physiological environments are investigated to take full advantage of the attractive capabilities of CMOS compatible low-cost plasmonic structures based on Cu. The accelerated in-situ tests of  $\text{HfO}_2/\text{Al}_2\text{O}_3$  nanolaminate shells in a mildly pH environment (emulated by using 1X PBS solution) in the temperature of the physiological environment ( $37^\circ\text{C}$ ) has demonstrated greatly enhanced endurance, with stable structures that last for more than one year.

The SPP resonant reflectivity position depends on the molecule type, while the reflectivity value at resonance is determined by the thickness of the molecular layer deposited on the metal surface. The SPP reflectivity behavior is the basic concept for SPP based sensing in biomedical sciences [5]. It can be used to monitor enzyme–substrate interaction, DNA hybridization and other biomolecular processes and the real-time monitoring of the kinetics of biomolecular pairs. The momentum matching needed to excite the SPP with electromagnetic radiation can be achieved by using a prism or a grating. The sensitivity of SPP sensors can be defined as the first derivative of the parameter to be monitored (wavelength, resonant angle, etc.) with respect to the parameter to be measured (concentration, refractive index, overlayer thickness, etc.).

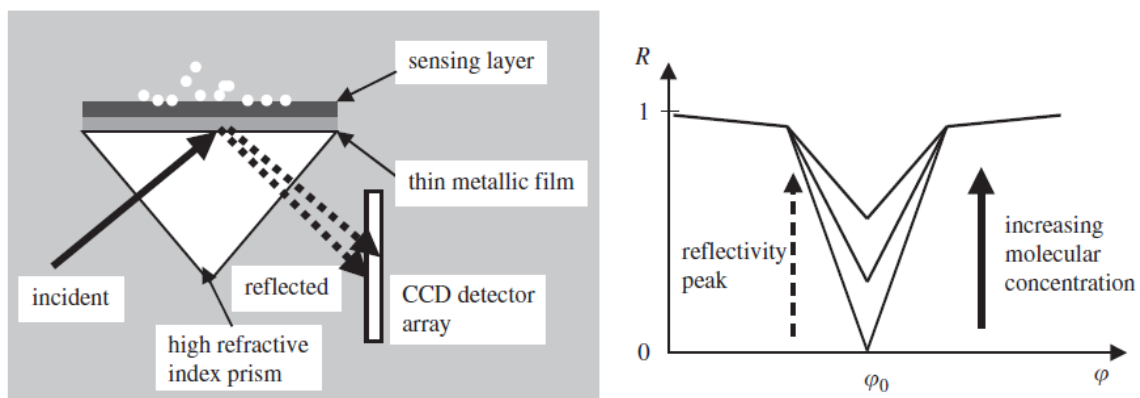


**Figure 3** (a) Schematic representation of a SPP biosensor, (b) SPP resonance dependence on molecular concentration. Dragoman, “Plasmonics: Applications to nanoscale terahertz and optical devices, Progress in Quantum Electronics 32 (2008) 1–41. Used under fair use, 2017

A surface plasmon could be viewed as a compressed quantum of light. Plasmonic devices are almost as compact as nanoelectronic components, but at the same time, they enable data transfer rates up to four orders of magnitude higher than electrical wires. Replacing even some of the electrical interconnects on a chip with plasmonic (nanophotonic) components would give a much-needed boost to microprocessor performance. Thus plasmonics can be used to increase the speed limit for intra-chip communications in microprocessors in the future [6] [7].

The active/passive plasmonic devices are analogous to and can play the same role as photonic devices, such as emitters (SPASER (Surface Plasmon Amplification by Stimulated Emission of Radiation) [8] [9]), detectors, waveguides, splitters, mirrors, lenses, resonators, etc. However, the SPP devices are not as advanced as photonic devices and are still in their nascent stages. Some SPP devices can also be integrated with photonic devices to enhance their performances (Example: SPP waveguide).

Moore's Law is the observation made in 1965 by Gordon Moore, co-founder of Intel that the number of transistors per square inch on integrated circuits has doubled every year since the integrated circuit was invented. Moore predicted that this trend would continue for the foreseeable future. In subsequent years, the pace slowed down a bit, but data density has doubled approximately every 18 months, and this is the current definition of Moore's Law. To improve the resolution of patterning, allowing circuit features to shrink shorter wavelength sources are needed. Since, according to the Rayleigh criterion, diffraction effects limit optical-lithography feature sizes to half the wavelength ( $\lambda/2$ ) of the light used

$$\text{Resolution} = \frac{k * \lambda}{NA}$$

Where, NA= Numerical Aperture

k = Proportionality Constant

The main limits to Moore's law are lithography and the need for very short wavelengths of light to pattern the minimum feature size and materials (for example the maximum current density in interconnects between transistors recently led to copper replacing aluminum as the conductor).

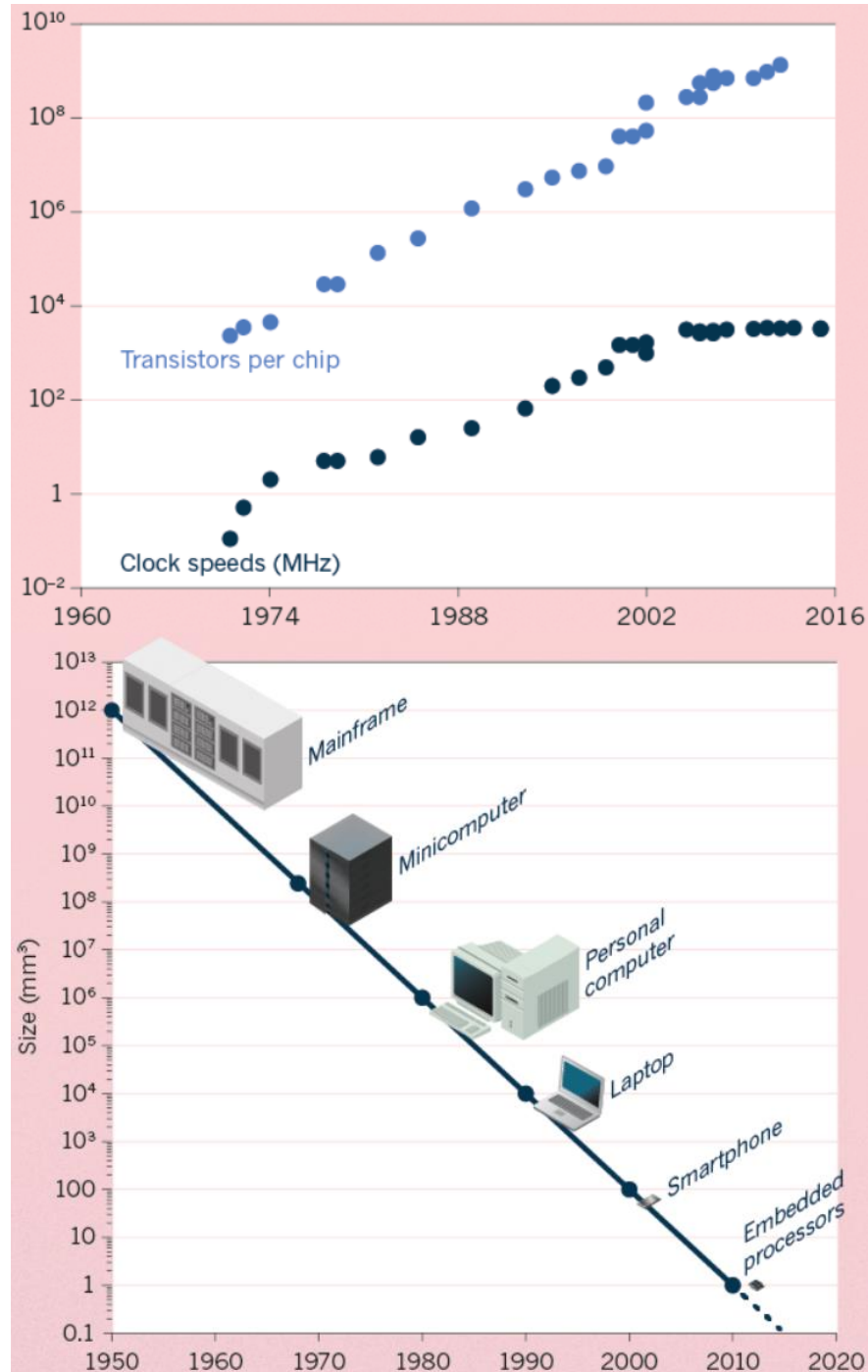


**Figure 4** Moore's Law over the years. M. Mitchell Waldrop, "The chips are down for Moore's law", Nature News, Nature Publishing Group, Feb 9, 2016. Used with permission from Nature Publishing Group. License attached

Keeping up with Moore's Law over the past four decades has seen lithography wavelengths drop from the 436 and 365 nm produced by mercury arc lamps to 248 nm by the krypton fluoride excimer laser to a 193-nm source with the argon fluoride laser, which is used to produce today's 45- and 32-nm IC technologies.

Despite the trend in reducing exposure wavelengths, today's aggressive feature sizes are still falling farther and farther below the available exposure sources, complicating the imaging challenges. Preserving Moore's law is pushing photolithography to its limits. Surface plasmon resonant interference nanolithography technique [10], with high spatial resolution (comparable to X-Ray) could be a possible solution to get around this diffraction limit. With the aid of a periodic corrugation or a prism, illumination light can couple with surface plasmon SP to obtain a new state named SPP, which has high field intensity and a much shorter wavelength compared to that of the illuminating light. The existing SPP resolution limit values of NA and  $k$  stand at 1.4 and 0.25 respectively.

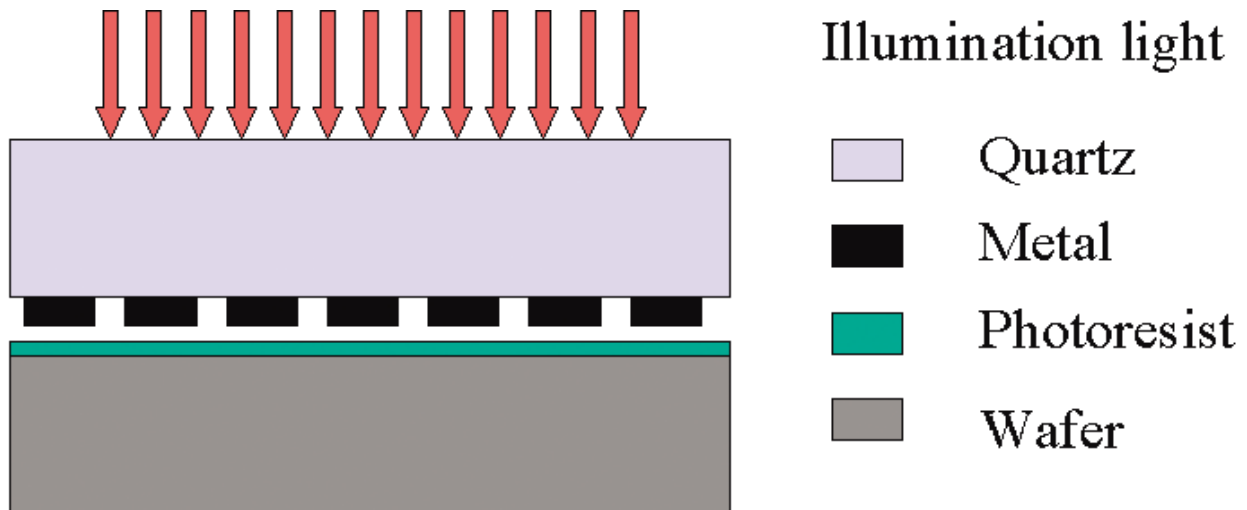


**Figure 5** Schematic representation of surface plasmon polaritonic lithography. Luo, et al., "Surface plasmon resonant interference nanolithography technique", Applied Physics Letters, Vol. 84, No. 23, 7 June 2004. Used under fair use, 2017

The basic principle behind LSPR sensors is that the particle we are trying to sense or the refractive index of the medium which we are trying to detect causes a change in the resonant response of the LSPR sensor that could be measured using transmission or reflectivity measurements. The change could be a wavelength shift, amplitude change or broadening of the resonance peak. For example as illustrated in one of the papers, when an analyte interacts with a ligand on the surface of a metal nanoparticle, we can observe a red-shift of the plasmon peak in the extinction spectrum [11].

The combination of plasmonics and Raman spectroscopy has led to advances in few-molecule investigations by concentrating light in plasmonic hot spots. Nanoplasmonics also allows label-free optical sensing and spectroscopy at the single nanoparticle level by exploiting plasmonic excitations in metal nanoparticles. This can be used for lab on chip applications like in situ measurements of local buffer concentrations inside a nanofluidic channel and real-time binding kinetics of alkanethiol molecules to a single plasmonic nanonantenna sensor in a single nanochannel [12].

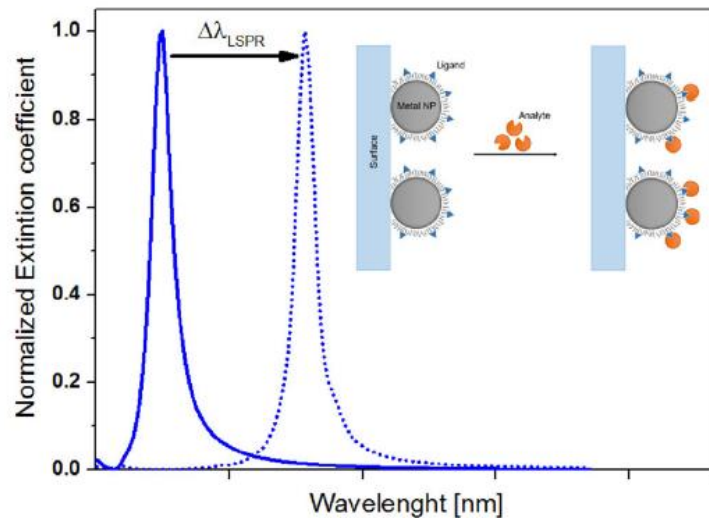


**Figure 6** Basic principle behind LSPR based sensors for detection of a particular molecule (analyte). Ramaccia, et al., “Core-shell super-spherical nanoparticles for LSPR-based sensing platforms”, *IEEE Journal of Selected Topics in Quantum Electronics*, Vol. 23, No. 2, March/April 2017. Used under fair use, 2017

In the sample lab on a chip application shown below, the channel connected at only one end acts as the reference. The nanoplasmonic sensors in the different channels can be activated to sense different components in the system. A Charge Coupled Device (CCD) acquires the response of the nano-particles on-chip. On-chip signal processing using the measured reference signal helps in removing the undesirable noise signals from the response. The shift in the resonance wavelength is a function of the refractive index of the material passing through the plasmonic sensor particles.

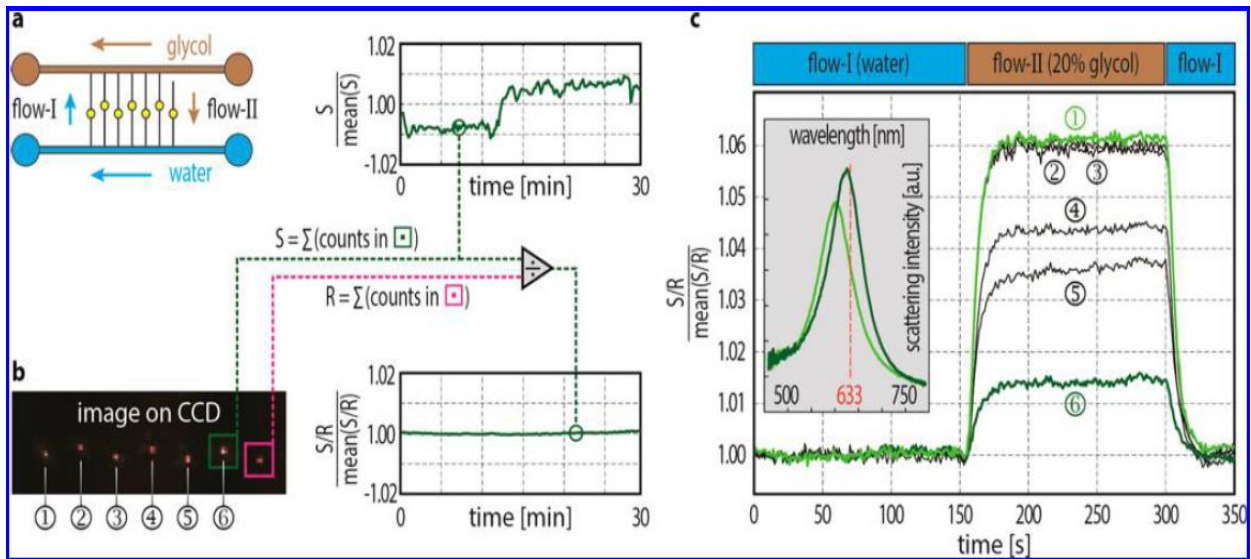


**Figure 7** Parallel monochromatic-illumination-based refractive index sensing in multiple nanochannels. Joachim Fritzsche et al., Nano Letters 2016, 16, 7857–7864. Used under fair use, 2017

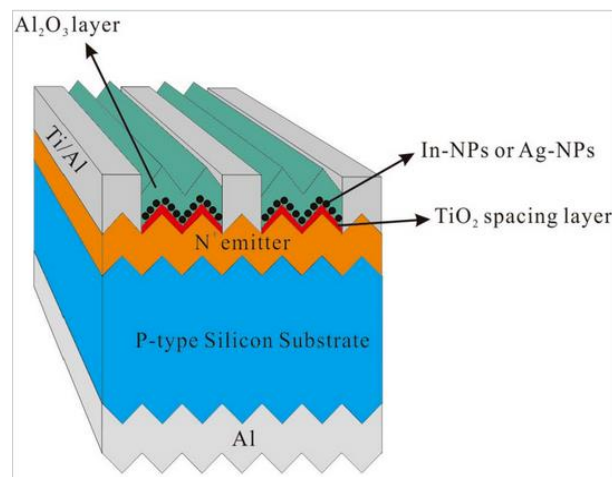


**Figure 8** Textured silicon solar cell. Wen-Jeng Ho, et al., “Performance-Enhanced Textured Silicon Solar Cells Based on Plasmonic Light Scattering Using Silver and Indium Nanoparticles”, Materials 2015, 8(10), 6668-6676. Used under fair use, 2017

Plasmonic nanoparticles integrated into textured c-Si solar cells have been shown to increase the absorption and enhance the short-circuit current density of the solar cell [13]. Attaching plasmonic nanoparticles on the periodic metallic grooves of the nano-photodiode results in more light being received [14], as expected the coupling efficiency of converting incident light into a sub-wavelength metal hole is increased. Thus plasmonic structures can also be used to increase the power conversion efficiency in solar cells. The conversion efficiency of cells with embedded In-NPs (14.85%) has been shown to exceed that of cells with embedded Ag-NPs (14.32%), due to the broadband plasmonic light scattering of the In-NPs [13].

The nanoplasmonic structures capable of being used in a whole lot of applications as outlined above, due to their capability of enhancing electromagnetic waves, go around the diffraction limit, sensitivity to variations in their environment, etc. being a nanometal is still in its nascent stages and is a growing field. Some of the major challenges associated with them are their sensitivity to defects, difficulty in large scale fabrication of defect free plasmonic structures, the exponential decay of the polariton's field intensity with the distance from the metal-air/insulator interface and the tendency of nanometals (other than gold, which is not CMOS compatible) to oxidize. Copper displays an intense and narrow LSPR peak that is comparable to Gold and Silver, while the plasmonic properties of Pt and Pd exhibit broader and weaker LSPR when compared to Ag. The LSPR  $\lambda_{\max}$  of Au (787 nm) > Cu (698 nm) > Ag (639 nm) for nanoparticles of the same geometry. Cu is also CMOS compatible and is much cheaper than the noble metals. It is the most abundantly used metal in electronics applications due to its high conductivity and low cost, but due to its proneness to surface oxidation, the plasmonic properties of Cu have not received much attention as compared to Ag and Au. Studies have shown that metal films of copper corrode at a fast rate of 1.1 to 2.5 nm/day in water at room temperature [15]. Figure 9 shows the optical microscope image of copper after 5.3 days of corrosion in 22 °C water. In the image small dark

regions are likely due to localized oxidation of copper. Large dark regions are clusters of localized oxidized copper. Copper corrosion is dependent on solutes in water [16] [17] [18], the pH of water [17] [19], and the water temperature [16] [20]. Copper metal is prone to surface oxidation even at ambient laboratory atmosphere and room temperature, forming  $\text{Cu}_2\text{O}$  (dominant product) and  $\text{CuO}$  (minor product) [21]. As nanoscale copper suffers rapid corrosion at higher temperatures and in ionic environments it is unsuitable for high temperature applications without some form of protective barrier. To solve this problem, it is proposed to use thin film ALD dielectric coatings as a corrosion barrier to protect the plasmonic structures and enhance their life-time in high temperature and corrosive environments. It is specifically important for implantable applications as in addition to cost and reliability factors, it will be more inconvenient for long-term use like diabetes monitoring.

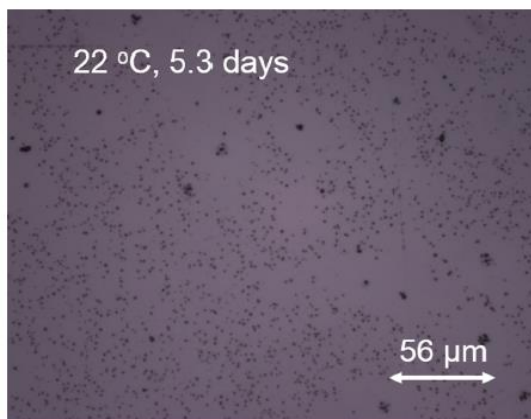


**Figure 9** Optical microscope image of copper after 5.3 days of corrosion in 22 °C water. Yersak, et al., “Characterization of Thin Film Dissolution in Water with in Situ Monitoring of Film Thickness Using Reflectometry”, ACS Applied Materials & Interfaces, 2016, 8, 17622–17630. Used under fair use, 2017

Improvements of the barrier performance protecting the structure underneath from corrosion should focus on reducing the number of defects while also improving the intrinsic barrier performance of the protective layer. Research exists to show that Aluminum Oxide ( $\text{Al}_2\text{O}_3$ ) ALD films with thicknesses of  $>10$  nm have equivalent barrier properties to glass on a copper substrate [22]. But  $\text{Al}_2\text{O}_3$  ALD film alone is insufficient to prevent copper corrosion because of the

dissolution of the  $\text{Al}_2\text{O}_3$  film in water.  $\text{TiO}_2$  films by themselves do not prevent the water corrosion of copper.  $\text{Al}_2\text{O}_3$  films with a  $\text{TiO}_2$  capping layer have been reported to be much more resilient to dissolution in water and much better at preventing the water corrosion of copper.  $\text{TiO}_2$  capping layers with thicknesses of  $\sim 20$  nm on the  $\text{Al}_2\text{O}_3$  adhesion layers with thickness  $\sim 20$  nm protected the copper for  $\sim 80$  days in water at  $90^\circ\text{C}$  [23]. It has also been demonstrated by research that Si nanowires coated with aluminum oxide ( $\text{Al}_2\text{O}_3$ ) in core shell configuration have long-term stability extending beyond 100 days in physiological solutions at  $37^\circ\text{C}$  in samples coated with just 10 nm thick  $\text{Al}_2\text{O}_3$  shells [24]. Nanolaminates (NLs) exhibit ultra-low moisture permeation with total equivalent  $\text{Al}_2\text{O}_3$  thickness thinner than in neat  $\text{Al}_2\text{O}_3$ . Capping  $\text{Al}_2\text{O}_3$  with 20 nm of  $\text{ZrO}_2$  has been shown to increase the time to failure due to corrosion by water [25]. 100 nm thick and 130 nm thick  $\text{Al}_2\text{O}_3/\text{ZrO}_2$  nano-laminates have permeation rates for both water and oxygen that are about one-half and one-fifth the values for 100 nm thick and 130 nm thick neat  $\text{Al}_2\text{O}_3$  layers, respectively [26]. All these data point to the fact that a nanolaminate structure offers better protection against diffusion of corrosive particles than a structure consisting of a single material. Addition of a dense atomic layer deposited  $\text{Al}_2\text{O}_3$  interlayer (like the one deposited by using ALD used in this project) leads to a greatly improved corrosion resistance, since the dense  $\text{Al}_2\text{O}_3$  interlayer acts as a good sealing layer and inhibits charge transfer, diffusion of corrosive substances, and dislocation motion [27].  $\text{HfO}_2$  alone has a tendency to crystallize at lower temperatures. Crystal grain boundaries will cause faster corrosion because they provide diffusion paths for water and ions. The crystallization problem can be circumvented by using  $\text{HfO}_2$  with a glass former like  $\text{Al}_2\text{O}_3$ —giving rise to the formation of an aluminate at the interface. This then retains the stability against crystallization to close to  $1000^\circ\text{C}$ . An amorphous oxide can configure its interface bonding to minimize the number of interface defects. Thus our protective coating structure which consists of multiple layers of  $\text{Al}_2\text{O}_3$  and  $\text{HfO}_2$  woven into each other acts as a

better protective coating than the existing methods for the same thickness of coating. This is because of the fact that it is denser, prevents formation of crystals with crystal boundaries and has lesser defects, than the coatings containing only  $\text{Al}_2\text{O}_3$  or only  $\text{HfO}_2$ .

Below the critical thickness of 5 nm of pure  $\text{Al}_2\text{O}_3$ , ALD leaves open / weakly covered spots even on feature-free surface sites and that leads to increased water ingress, for 15–25 nm barrier thicknesses there is an exponential decrease in defect density with barrier thickness and consequently an exponential decrease in water permeation rate [28]. Increasing thickness affects the LSPR of plasmonic nanoparticles; the method developed in this project provides an increased stability of beyond 1 year with a thickness of just 5 nm. It also provides significant increase in stability for protective coating thicknesses of just 1 nm and 3 nm.

Scaling of complementary metal oxide semiconductor (CMOS) transistors has led to the silicon dioxide layer, used as gate dielectric, becoming very thin that its leakage current is too large; reliability of  $\text{SiO}_2$  films against electrical breakdown also declines in thin films. Thus oxides of higher dielectric constant such as hafnium oxide are being explored to be used as gate dielectric material.  $\text{HfO}_2$  is presently the preferred high K oxide over  $\text{ZrO}_2$  [29]. The fact that crystallized  $\text{HfO}_2$  does not cause higher leakage current has convinced many companies (e.g. Intel and Freescale) to favor binary oxides because of their higher K. The method developed in this project uses  $\text{HfO}_2$  and  $\text{Al}_2\text{O}_3$  as materials of the coating, these materials are CMOS compatible and the ALD process by which they are deposited is also CMOS compatible, therefore it is a low cost solution, most compatible with the existing process.  $\text{HfO}_2$  and  $\text{Al}_2\text{O}_3$  are also bio-compatible and when used in lab-on-chip applications the fabrication cost is lesser since sensing and electronic parts can be integrated. It also leads to smaller package size and hence less resistance, RC time delay and less noise coupling.

For plasma enhanced physical vapor deposition (PECVD) films, a reduction in substrate temperature from 300°C to 150°C has been reported to result in an increase in the hydrogen content in the film from ~6 to 20%. For films with hydrogen content above 3–4%, the remaining fraction of hydrogen will occur as clusters in the film and form voids in the film [30]. These voids in the protective coating would lead to permeation of the physiological solution into the plasmonic structure through the coating layers, leading to their faster oxidation, this would necessitate the growth of the protective coating film at higher temperatures, but flexible polymer substrates like PET can only be used with processes at low temperatures like 150°C, the process used in this project involves ALD at a relatively low temperature of 150°C and hence can be used on those kind of substrates also. ALD also deposits high density, high quality films (low defects) and gives the good step coverage needed for plasmonic structures. Low temperature used here also leads to lower diffusion of impurities during processing.

Conventional ex situ measurements cannot give thin film dissolution dynamics for real systems that do not experience periodic interruptions in the dissolution process. This project uses in-situ transmission measurements to evaluate the stability of the plasmonic structure under the protective coating being investigated. Transmission measurements also have the capability to measure location-dependent dissolution dynamics. Since normalized transmittance from the measurement is used, any intrinsic error in the measurement is also eliminated in the process.

## 2. Hypothesis

Improvements of the protective coating performance should focus on reducing the number of defects while also improving the intrinsic barrier performance of the hybrid layer. Increased water permeation can happen through regions of the barrier film that contain nanoscale size defects or through uniformly distributed sub-micron defects or porosity in the film (intrinsic film permeation). Intrinsic barrier film performance and the permeation through this region is assumed to be negligible in case of barrier films with macroscale defects, since films grown by ALD are fairly defect free. The pin-hole defects of the barrier film affect lower thickness films (films with thickness less than 2 nm) more than the thicker layers; because thinner films have fewer layers and a pin-hole could leave areas unprotected by the film, leading to faster corrosion of the plasmonic structure underneath. The intrinsic permeation rate has been observed to contribute approximately 3 times more to the effective water permeation than the defect assisted local permeation rate in the tested barrier films with less defects [31].

ALD allows the deposition of very dense films at low temperatures ( $<100^{\circ}\text{C}$ ) (needed when flexible substrates like PET are used), hence ALD can be used on a wide range of materials like metals, polymers, etc., and thus ALD is a good method for preparing protective coating layers on top of plasmonic devices. PECVD, LPCVD, and E-beam coatings contain more defects than ALD coatings and cannot provide a thin and conformal barrier on high aspect ratio structures. ALD substrate temperatures during deposition can be used to control the hydrogen content in the film. Reduction in substrate temperature from 300 to  $150^{\circ}\text{C}$  in plasma enhanced physical vapor deposition (PECVD) films, causes an increase in film hydrogen content from  $\sim 6$  to 20 %. For films with hydrogen content above 3–4%, the remaining hydrogen will occur as clusters and form voids in the film [30]. Thus ALD is used for preparing protective coating layers on top of the plasmonic devices used in this project.

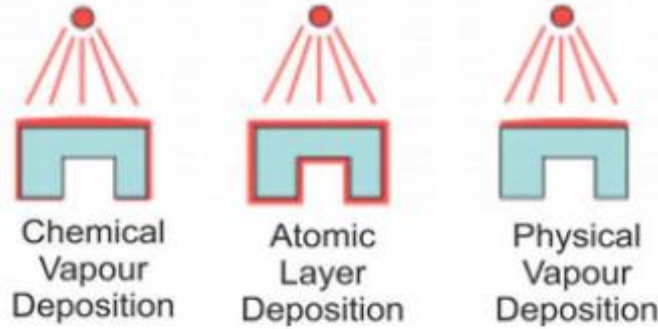


**Figure 10** Comparison of step coverage of CVD, ALD and PVD

Best diffusion barriers are obtained in nanolaminate structures containing crystalline layers sandwiched between amorphous layers [10] [11]. Nanolaminates (NLs) exhibit ultra-low moisture permeation with total equivalent  $\text{Al}_2\text{O}_3$  thickness thinner than in neat  $\text{Al}_2\text{O}_3$ , due to the formation of a continuous, tortuous network of alumina in the NL. Pure  $\text{Al}_2\text{O}_3$  is more susceptible to corrosion by condensed water because they are amorphous with hydrogen incorporated in the films during their growth by ALD [25]. When the ALD film composition is an oxy-hydroxide, the barrier energy for reaction with water is lowered and this facilitates conversion of ALD amorphous  $\text{Al}_2\text{O}_3$  thin films to hydroxide phases, especially in films grown at low temperature with significant H-content. Since these hydroxides are crystalline (albeit poorly crystalline), they are likely to be highly permeable due to more facile gas permeation along grain boundaries or along hydroxide chains. If the growth process for  $\text{Al}_2\text{O}_3$  also has a CVD component, it can adversely affect film permeation and stability. CVD can occur in an ALD process sequence, when the purge times are too short or one of the reactants is difficult to remove, e.g.,  $\text{H}_2\text{O}$  at low temperature, so that films do not grow by a layer-by-layer process but by point nucleation, when both reactants are present simultaneously. Point nucleation can result in a more faceted microstructure, which is more permeable and chemically reactive. Thus an adequate purge and wait times of 0.015 s and 20 s was used for  $\text{H}_2\text{O}$  during ALD in this project.  $\text{Al}_2\text{O}_3$  ALD nucleates

and grows efficiently on copper using trimethylaluminum (TMA) and water as the reactants. It is also established that the  $\text{Al}_2\text{O}_3$  ALD films has a low defect density [23].

Grain boundaries in sealing layers are important channels for gas permeation. The nano-laminate sealing layer has reduced defect density when compared to neat  $\text{Al}_2\text{O}_3$  film.  $\text{Al}_2\text{O}_3$  films grown at low temperatures contain more hydrogen than those grown at higher temperatures, since films grown at lower temperatures have an accumulation of Al-OH species due to incomplete precursor reaction [26]. In a material with the tendency to crystallize ( $\text{HfO}_2$ ), the multilayer structure on the nanometer scale reduces the crystallite sizes by cyclic termination of the film growth after a few nanometers. The  $\text{HfO}_2$  layer stops the accumulation of un-reacted Al-OH species and the formation of extended voids in the  $\text{Al}_2\text{O}_3$  sub-layers observed for neat  $\text{Al}_2\text{O}_3$  films. The  $\text{HfO}_2$  nano-crystal does not extend far beyond the sub-layer where it originated, due to the  $\text{Al}_2\text{O}_3$  layers in between. The  $\text{Al}_2\text{O}_3$  layer is amorphous, and thus the contact of nano-crystals in adjacent  $\text{HfO}_2$  sub-layers is avoided. Thus the formation of highly efficient permeation paths due to molecule diffusion along nano-crystal grain boundaries is successfully hindered. Densification due to the formation of a  $(\text{Hf})\text{Al}_x\text{O}_y$ -aluminate phase at the interfaces also suppresses ion and water permeation through the barrier stack. Thus the effectively suppressed void formation and suppressed formation of extended crystals as a result of the alternating multilayer structure decreases the permeability of the coating to water and hence reduces corrosion of the plasmonic structure due to water exposure and increases its life time in high temperature corrosive environments.

As a nanolaminate structure in which one component is crystalline and one component is amorphous at the process temperatures gives best protection against diffusion and considering the need for bio-compatible materials for implantable applications, the material chosen for the nanolaminate coating in this project is  $\text{Al}_2\text{O}_3$  and  $\text{HfO}_2$ .  $\text{HfO}_2$  has a crystallinity temperature ~

350°C-600°C, while Al<sub>2</sub>O<sub>3</sub> has a crystallinity temperature ~ 700°C-800°C. They also have the added advantage of being CMOS compatible. Tests indicate that unlike HfO<sub>2</sub> coating, HfO<sub>2</sub>/Al<sub>2</sub>O<sub>3</sub>/... nanolaminate multilayer coatings still can be etched away at a reasonable speed in BOE (HF based).

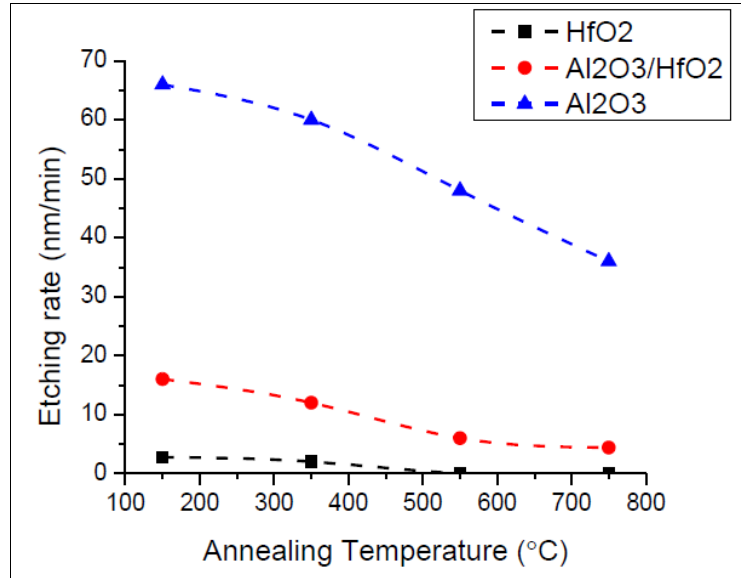


**Figure 11** Etch rate comparison of Al<sub>2</sub>O<sub>3</sub>, HfO<sub>2</sub> and the Nanolaminate structure in BOE

Aluminum and Copper were the metals considered for the plasmonic structure, since they are both CMOS compatible. Melting point of copper is at 1085°C, while the melting point of Aluminum is only 660 °C. Since copper does not melt for the crystallinity temperature range of Al<sub>2</sub>O<sub>3</sub> and is CMOS compatible it is chosen as the material for our plasmonic structure. Different samples were fabricated in order to investigate the effect of thickness of the protective coating, composition of the protective coating (stability of pure Al<sub>2</sub>O<sub>3</sub> coatings and pure HfO<sub>2</sub> coatings vs. nanolaminate coatings of different compositions) and the effect of the coating materials being amorphous, crystalline and mixture of both states (conditions obtained by using different annealing temperatures) on the stability of the plasmonic structure in physiological environments.

Annealing temperatures of 400°C in vacuum do not reduce the dissolution rate of the ALD deposited films but leads to an increase of ~33% of water dissolution rate, suggesting that dehydrogenation and resulting formations of clustered voids in the films without concurrent film crystallization and densification due to the thermal annealing process increases the effective active area for dissolution in water [32]. Hence the annealing process in this project is carried out in a nitrogen environment. ALD leaves an oxygen-rich film. When the oxidant is water, the film contains –OH groups. Annealing tries to evolve these as H<sub>2</sub>O molecules. However, as the film densifies, H<sub>2</sub>O is too large to diffuse through and H diffuses either as H<sup>+</sup> ions or H<sub>2</sub> molecules, desorbing as H<sub>2</sub> [29]. It is more difficult to nucleate HfO<sub>2</sub> on H-terminated surfaces and hence oxygen plasma etching is done to make the surface O-terminated.

### 3. Methodology

#### 3.1. Initial Testing

Ellipsometry sets polarization state of the incident beam and measures the change in polarization state of light reflected from (or transmitted through) the surface of a sample. Ellipsometry measurements are very accurate because it measures ratio of two values. Ellipsometry can be used to determine optical constants (n and k), dielectric constants ( $\epsilon_1$  and  $\epsilon_2$ ), film thickness, doping concentration, surface roughness, alloy ratio, crystallinity, etc. Ellipsometry determines these values by measuring phase difference ( $\Delta$ ) and amplitude ( $\psi$ ) as a function of wavelength. These values are related to the ratio of Fresnel reflection coefficients  $R_p$  and  $R_s$  for p- and s-polarized light, respectively.

$$\rho = \frac{R_p}{R_s} = \tan(\psi)e^{i\Delta}$$

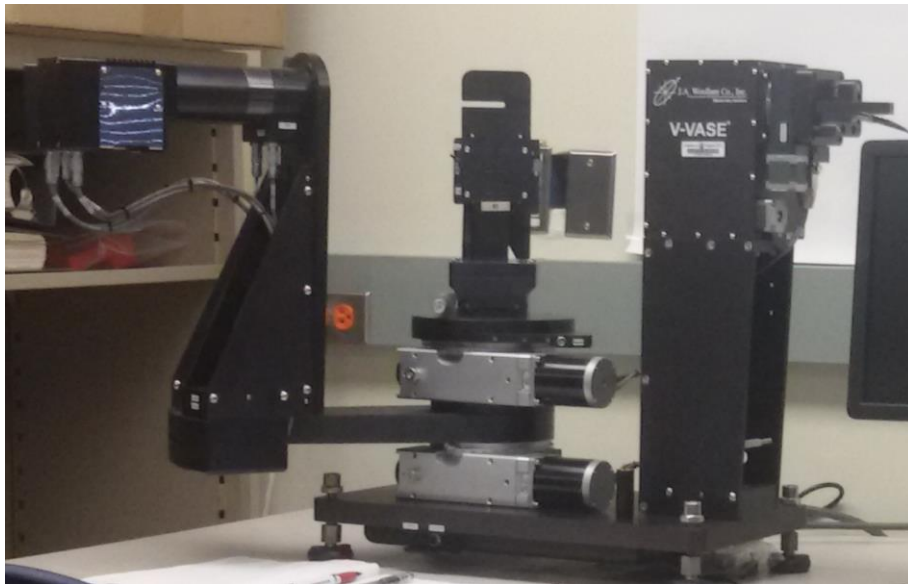


**Figure 12** J.A.Woollam Co., Inc. Variable Angle Spectroscopic Ellipsometer (VASE) used in the project

Initially bare Si wafer was characterized using Ellipsometry to measure the thickness of the native oxide ( $\text{SiO}_2$ ) on it. It was measured to be 1.916 nm. This was determined to see if a  $\text{SiO}_2$  layer has to be added to get low MSE in future measurements.

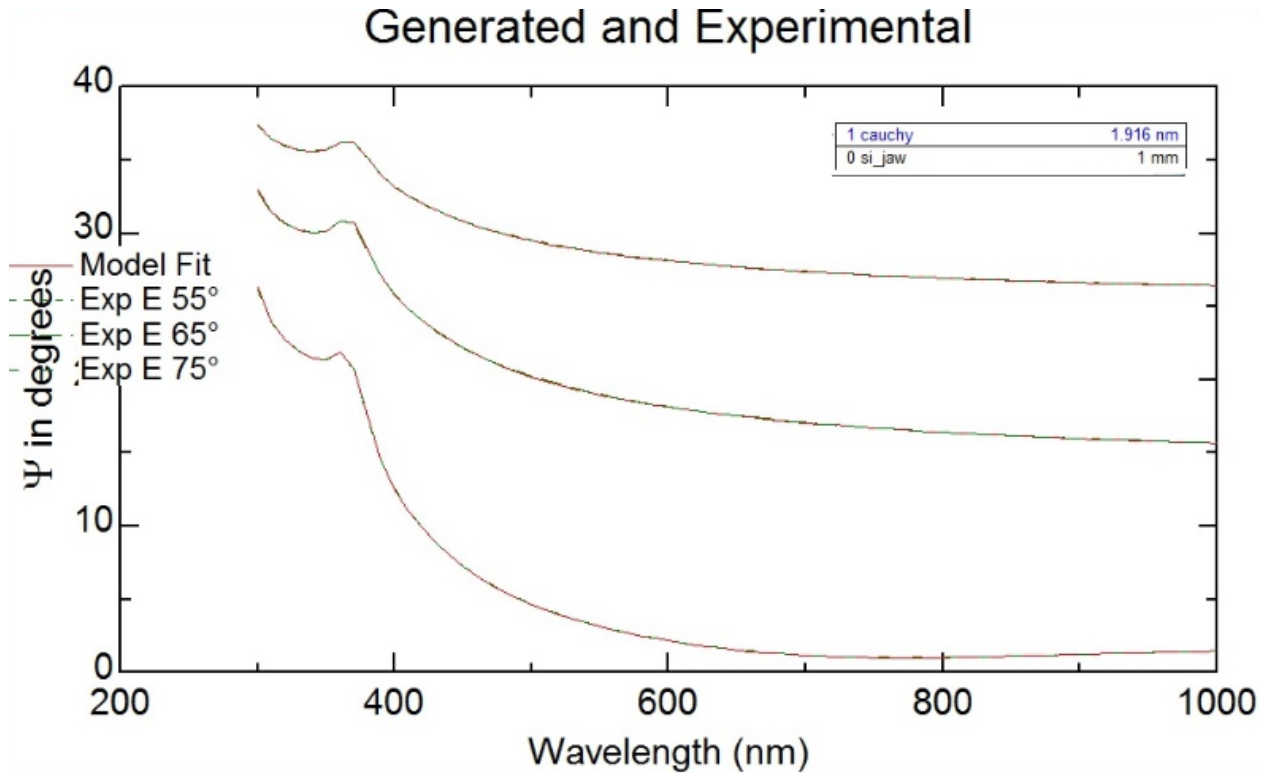


**Figure 13** Bare Silicon Characterization using ellipsometry

$\text{HfO}_2$  has a crystallinity temperature of around  $350^\circ\text{C}$ - $600^\circ\text{C}$  and  $\text{Al}_2\text{O}_3$  has a crystallinity temperature of around  $900^\circ\text{C}$ - $1050^\circ\text{C}$ . So a composite mixture of  $\text{HfO}_2$  and  $\text{Al}_2\text{O}_3$  is expected to have a crystallinity temperature tunable between the ranges of  $450^\circ\text{C}$ - $1000^\circ\text{C}$ . In order to test the thin film characteristics of the protective coatings for different annealing temperatures and compositions the following 16 test samples were fabricated.

Samples to test the effect of ratios of Al <sub>2</sub> O <sub>3</sub> and HfO <sub>2</sub> (A H A H A) on crystallinity					
Thickness 50 nm	T = 150 °C	T = 400 °C	T = 650 °C	T = 900 °C	
			3 1 1 1 2	3 1 1 1 2	
	3 5 5 5 2	3 5 5 5 2	3 5 5 5 2	3 5 5 5 2	
		5 10 10 10 5	5 10 10 10 5		
	Pure Al <sub>2</sub> O <sub>3</sub>				
	Pure HfO <sub>2</sub>				

**Table 1** Initial Testing: Thin Film Characterization (16 samples)

Al <sub>2</sub> O <sub>3</sub> : 3 Layers	More 5 Layers for different thicknesses
HfO <sub>2</sub> : 5 Layers	
Al <sub>2</sub> O <sub>3</sub> : 5 Layers	
HfO <sub>2</sub> : 5 Layers	
Al <sub>2</sub> O <sub>3</sub> : 2 Layers	
Wafer	

**Figure 14** Coating Profile

In the protective coating layers deposited the HfO<sub>2</sub> layer is sandwiched in between two Al<sub>2</sub>O<sub>3</sub> layers. Figure 14 shows the deposition pattern for a 2 nm protective coating. Two layers of Al<sub>2</sub>O<sub>3</sub> are deposited on the substrate, on top of which 5 layers of HfO<sub>2</sub> and 5 layers of Al<sub>2</sub>O<sub>3</sub> are deposited to get the desired thickness and finally 3 layers of Al<sub>2</sub>O<sub>3</sub> is deposited on top. Therefore a total of 20 layers are deposited to get a thickness of 2 nm. The precursor used for Al<sub>2</sub>O<sub>3</sub> deposition was Trimethylaluminum and H<sub>2</sub>O and the precursor used for HfO<sub>2</sub> growth is Tetrakis(Dimethylamido)Hafnium (Hf(NMe<sub>2</sub>)<sub>4</sub>) and H<sub>2</sub>O. For some annealing temperatures Al<sub>2</sub>O<sub>3</sub>

is amorphous and  $\text{HfO}_2$  is in crystal form. Each layer of  $\text{Al}_2\text{O}_3$  has a thickness of 1.04 Armstrong and each layer of  $\text{HfO}_2$  has a thickness of 1.01 Armstrong when grown at  $150^\circ\text{C}$ .

Before deposition of the thin films the wafer is washed with Acetone, IPA and DI water and further cleaned using oxygen plasma in RIE. After installation of the precursors the reactor temperature for ALD is set to  $150^\circ\text{C}$  and the deposition chamber is seasoned for 3 hours before putting the wafer inside. The precursor for Hafnium Oxide has to be heated to  $75^\circ\text{C}$  for deposition; this can be set by adjusting the temperature of the heater sleeve around the precursor. Using different variations and combinations of the recipes shown in Table 9, the different types of protective coatings were fabricated for our requirements. Growth time of 50 nm of pure  $\text{HfO}_2$  is close to 3.5 hours and the growth time of 50 nm of pure  $\text{Al}_2\text{O}_3$  is close to 1.5 hours. The rest of the structures containing a combination of  $\text{HfO}_2$  and  $\text{Al}_2\text{O}_3$  in different ratios take around 2.5 hours each to grow.

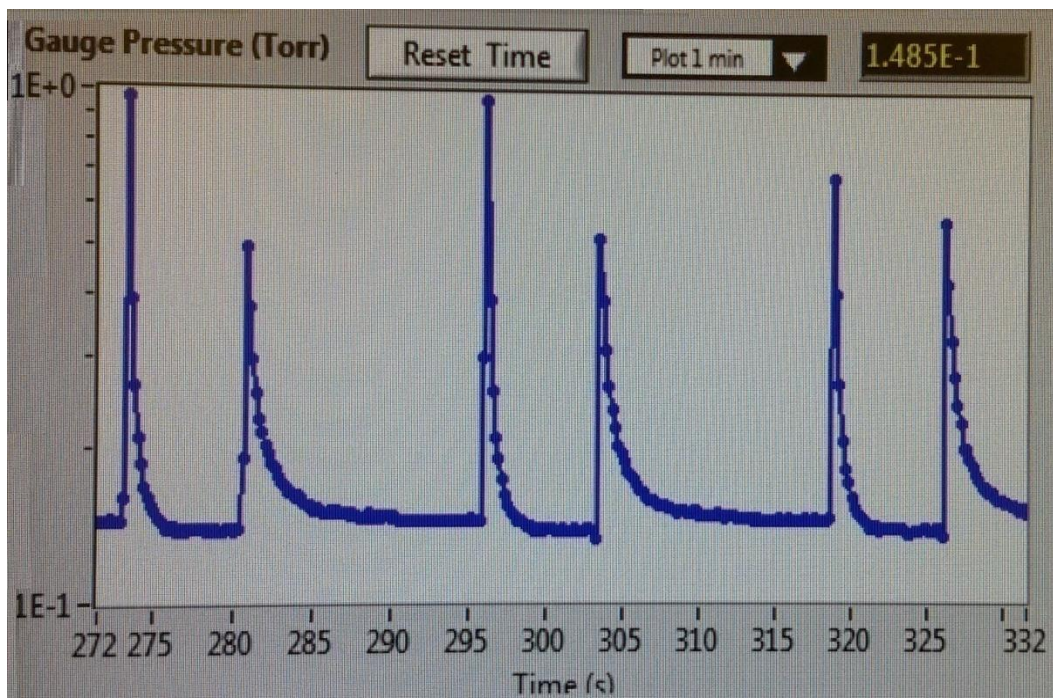
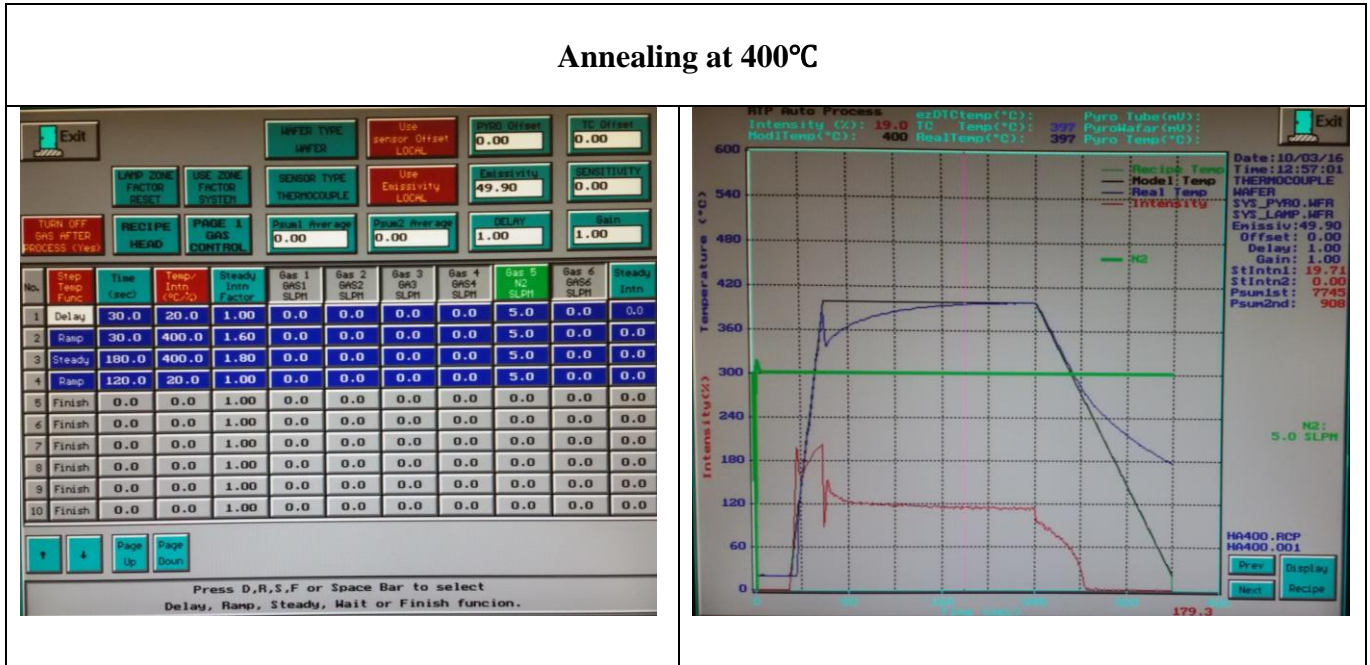


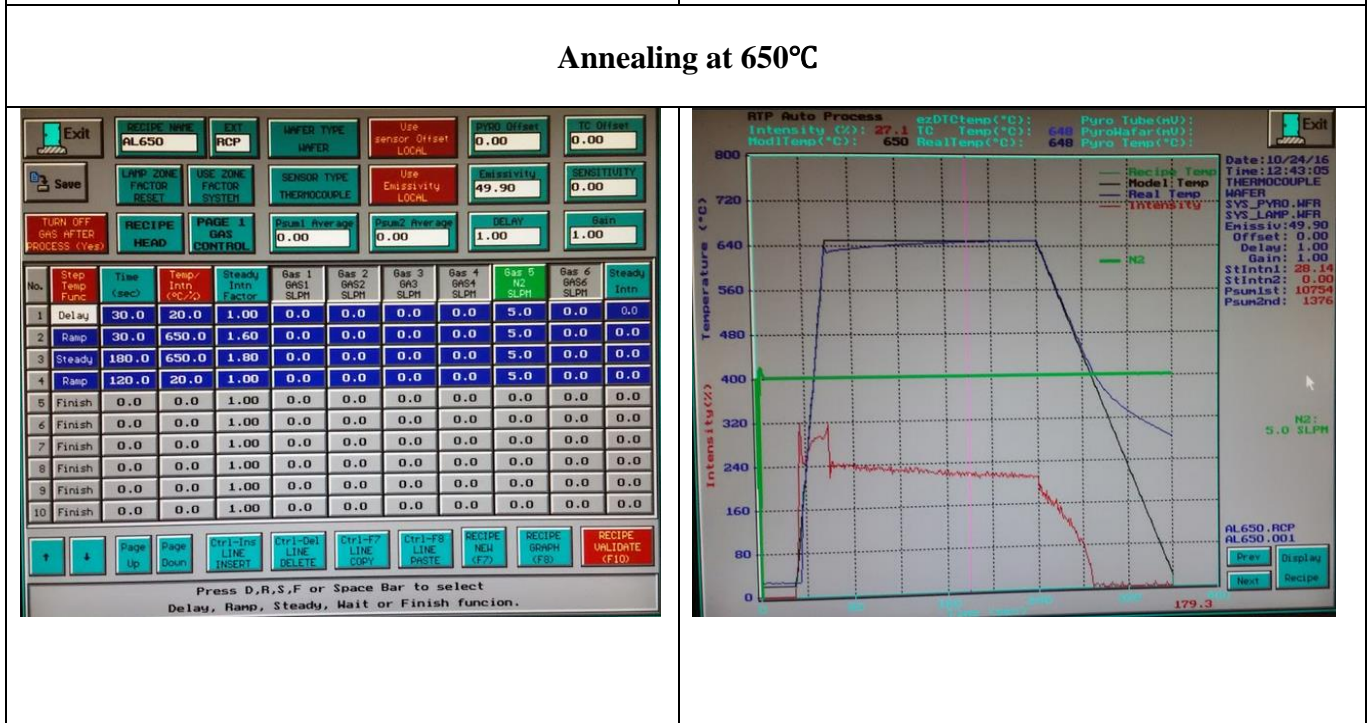
**Figure 15** Chamber Pressure Curves during ALD

Rapid Thermal Annealing (RTA) was carried out in a nitrogen environment at 400°C, 650°C and 900°C. Since the deposition itself happens at 150°C, the 150°C need not be annealed as annealing them will not lead to any structural changes. The annealing recipes and their graphs are as follows:

### Annealing at 400°C



### Annealing at 650°C



## Annealing at 900°C

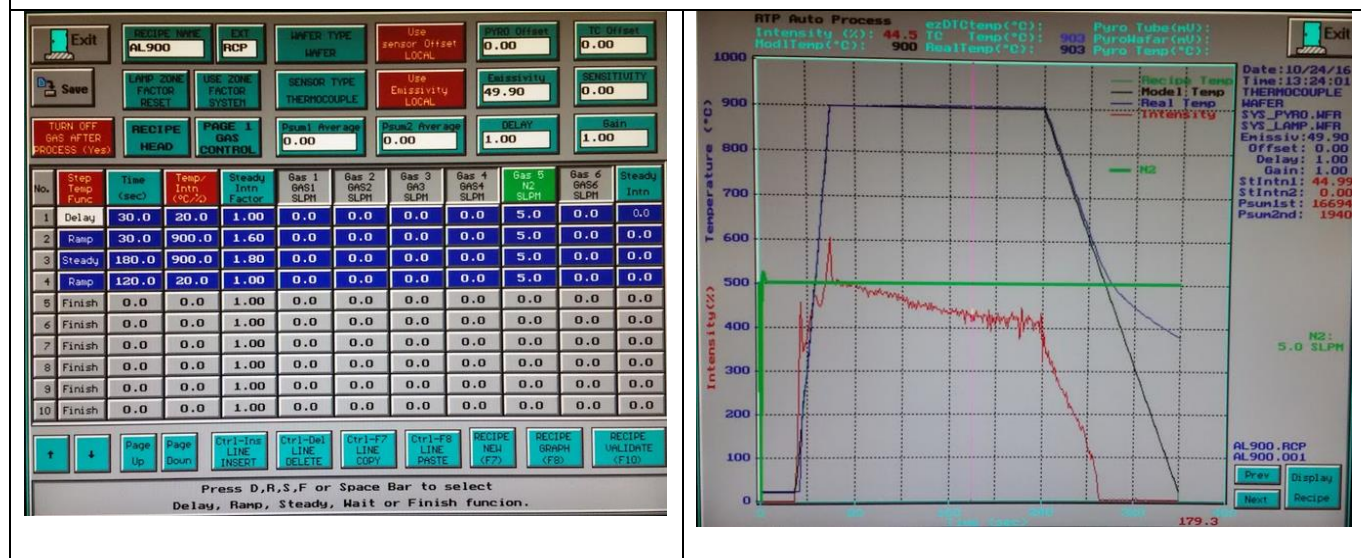


**Figure 16** Thin Film Characterization Annealing Recipes and Graphs

The basic procedure used in Ellipsometry measurements to determine the needed material properties from the experimental data consists of measurement, modeling, fitting, checking the goodness of the fit and repeating from the modeling step if the fit is not good enough. From the perspective of light beam interaction of light with a given material can be described by the wavelength,  $n$  (index of refraction) and  $k$  (extinction coefficient). From perspective of the material, interaction of light with a given material can be given by  $E$  (Energy), real and imaginary parts of dielectric function of the material. The relationship between energy and wavelength is:  $E=1240/\lambda$ , the wavelength is in nano meters. The relationship between  $n$  &  $k$  and  $\epsilon_1$  and  $\epsilon_2$  is:  $\epsilon_1 + j \epsilon_2=(n+jk)^2$  or  $\epsilon_1=n^2-k^2$  and  $\epsilon_2=2nk$ .

### 3.2. Ellipsometry Data- Fit Improvement

A good fit for thin film samples with relatively little data structure will typically have MSE (Mean Squared Error) around 1-5. It is common to see higher MSE (10-20 or higher) for thicker films, multi-layers, graded-index materials, anisotropic films and other complex samples. For any

sample, the goal is not to achieve a specific MSE value but to minimize the MSE while still meeting the following criteria:

- The model should be unique: As a guideline MSE improvements less than 20% do not justify added model complexity
- The model and fit parameters must be physically possible (example: Where  $k=0$ ,  $n$  must increase toward shorter wavelengths,  $k$  cannot be negative, etc)

Ellipsometry is sensitive to  $k$  values only up to the third decimal place ( $\sim 0.001$ ). Almost for all samples fitting only the optical constants  $n$  and  $k$  gives a better fit, because it has a fewer constraints (this method is Kramers-Kronig inconsistent). Fitting only  $n$  and  $k$  is not suitable to this project due to the following reasons:

- $n/k$  checkboxes can be checked if thickness is known. In this project thickness is one of the parameters measured using ellipsometer. Even if thickness is measured using other techniques like Filmetrics, the thickness will not be truly known to sensitivity level of ellipsometer, at same location, within same measurement area, etc. If thickness is wrong, there will be errors in  $n$  and  $k$  ( $e_1$  and  $e_2$ ).
- If the data has any noise, this causes errors in  $n$  and  $k$ .
- If this algorithm finds two possible solutions for any wavelength, there may be a jump in the curve and errors in  $n$  and  $k$ .

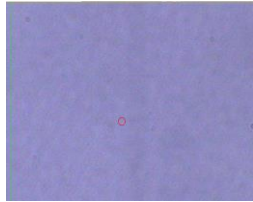
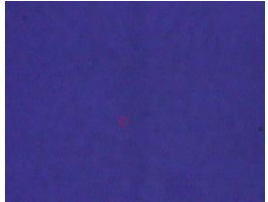
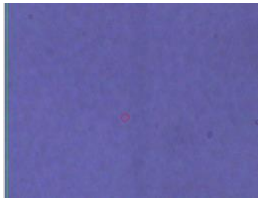
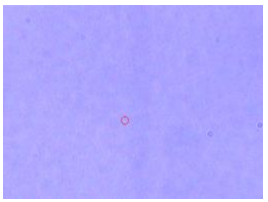
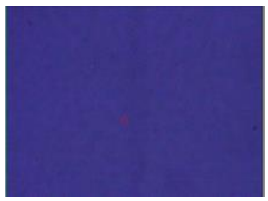
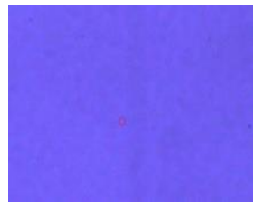
Transmission Intensity measurements can be used for band gap determination (using R & T Data (R: Reflection Intensity, T: Transmission Intensity) scan. But there is high uncertainty in the determination of the right shape of absorption for 50 nm thick  $\text{HfO}_2$  and  $\text{Al}_2\text{O}_3$  coatings since their absorption is pretty low. Also the ellipsometer in the characterization lab has the maximum energy at  $\sim 4.8$  eV (minimum wavelength producible from the light source is only 260 nm). The bandgap of films used in this project is higher than that, it is 8.8 eV for  $\text{Al}_2\text{O}_3$  and 5.8 eV for  $\text{HfO}_2$ ,

so it is not possible to find the bandgap energy with the data we gather from ellipsometry measurements in this case.

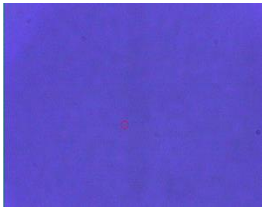
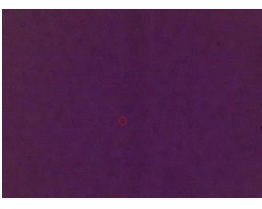
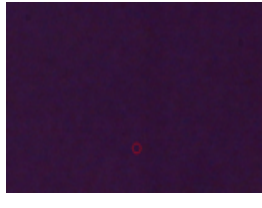
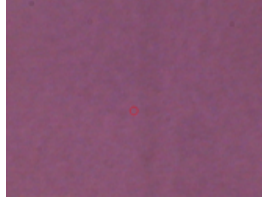
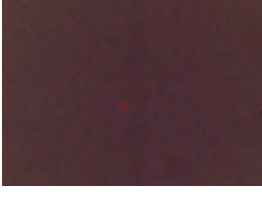
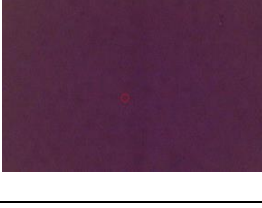
Cauchy fit can be used when the material is transparent or nearly transparent, with a small amount of absorption at the UV-end of the spectral range of interest. If there is significant absorption in the spectral range of interest, particularly if there is an absorption band in the middle of the range, Cauchy expression is insufficient to describe the optical properties of the material. An absorption band is very different from metallic absorption which usually covers a very wide spectral range. Typically absorption bands in the IR are due to molecular vibrations (such as C=O stretch), in the UV are due to electronic vibrations, in the visible regions for a dye in an organic film. In some of the samples in this project absorption happens at wavelength in the range of 300 nm to 400 nm (UV wavelength range), so it could be due to electronic vibrations. Therefore high MSE was observed for the initial fit obtained using Cauchy model and resonance is observed in refractive index and dielectric constant plots due to absorption. This high MSE could have also been a result of roughness and refractive index changes caused by air bubbles trapped on the surface, as observed in the microscopic images. The combination of solutions used to address this issue are slow annealing, using optimized General-Oscillator model and accounting for the surface roughness.

### **3.2.1. Slow Annealing**

The issue of surface roughness due to trapped air bubbles was observed only in the case of pure Al<sub>2</sub>O<sub>3</sub> films annealed at higher temperatures using a rapid rise in temperature.

Material (50 nm)	Annealing Temperature (°C)	Microscopic Image	
		20X Magnification	100X Magnification
Pure HfO <sub>2</sub> (150°C Growth)	150 °C		
Pure HfO <sub>2</sub> (150°C Growth)	400 °C		
Pure HfO <sub>2</sub> (150°C Growth)	650°C		
Pure HfO <sub>2</sub> (150°C Growth)	900°C		

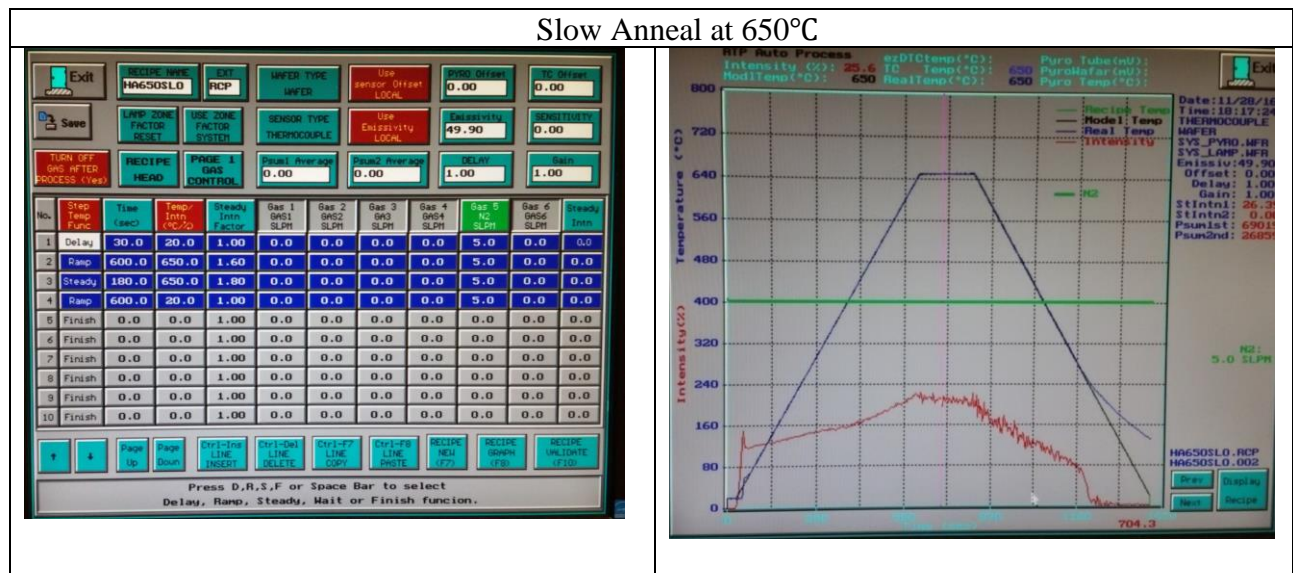
Material (50 nm)	Annealing Temperature (°C)	Microscopic Image	
		20X Magnification	100X Magnification
Pure Al <sub>2</sub> O <sub>3</sub> (150°C Growth)	150 °C		
Pure Al <sub>2</sub> O <sub>3</sub> (150°C Growth)	400 °C		
Pure Al <sub>2</sub> O <sub>3</sub> (150°C Growth)	550 °C		
Pure Al <sub>2</sub> O <sub>3</sub> (150°C Growth)	800 °C		
HfO <sub>2</sub> + Al <sub>2</sub> O <sub>3</sub> : 3 5 5 5 2 (150°C Growth)	150 °C		
HfO <sub>2</sub> + Al <sub>2</sub> O <sub>3</sub> : 3 5 5 5 2 (150°C Growth)	400 °C		
HfO <sub>2</sub> + Al <sub>2</sub> O <sub>3</sub> : 3 5 5 5 2 (150°C Growth)	650 °C		

Material (50 nm)	Annealing Temperature (°C)	Microscopic Image	
		20X Magnification	100X Magnification
HfO <sub>2</sub> + Al <sub>2</sub> O <sub>3</sub> : 3 5 5 5 2  (150°C Growth)	900 °C		
HfO <sub>2</sub> + Al <sub>2</sub> O <sub>3</sub> : 3 1 1 1 2  (150°C Growth)	400 °C		
HfO <sub>2</sub> + Al <sub>2</sub> O <sub>3</sub> : 3 1 1 1 2  (150°C Growth)	650°C		
HfO <sub>2</sub> + Al <sub>2</sub> O <sub>3</sub> : 5 10 10 10 5  (150°C Growth)	400°C		
HfO <sub>2</sub> + Al <sub>2</sub> O <sub>3</sub> : 5 10 10 10 5  (150°C Growth)	650°C		

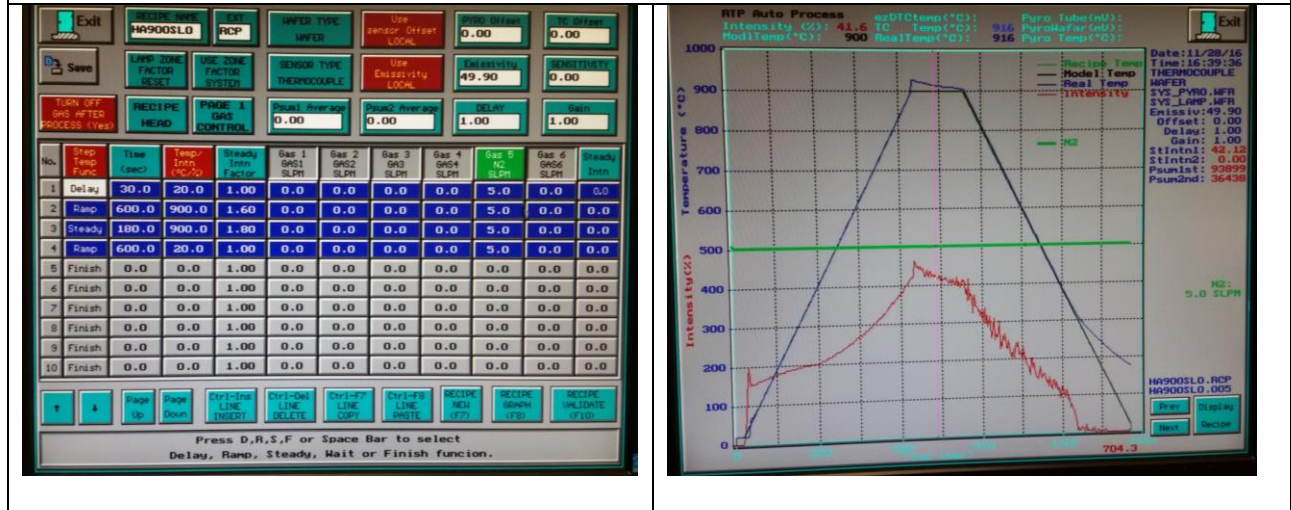
**Table 2** Microscope Images of Samples

Aluminum Oxide (amorphous) exhibits increase in the number of pores on its surface at higher annealing temperatures; this could be due to expansion and consequent expulsion of trapped gases from the amorphous Al<sub>2</sub>O<sub>3</sub> in response to the rapid increase of temperature during annealing. By comparing the samples of Aluminum Oxide annealed at 900°C grown at 150°C and 250°C it can be concluded that the film deposited by ALD at a lower temperature has more pores and its pores are

on an average larger than that of the pores grown at a higher temperature, this could be due to more oxygen content in the film deposited at lower temperatures. Thus in the samples with pure  $\text{Al}_2\text{O}_3$  coating annealed rapidly at higher temperatures there is a possibility that the high MSE is due to the increased surface roughness. It is worthwhile to note that these bubbles are not observed in samples coated with the nanolaminate structure of  $\text{Al}_2\text{O}_3$  and  $\text{HfO}_2$ , even though  $\text{Al}_2\text{O}_3$  is still amorphous. This points to the fact that  $\text{HfO}_2$  interspersed between the  $\text{Al}_2\text{O}_3$  layers effectively prevents the formation of large voids in  $\text{Al}_2\text{O}_3$ . To reduce the bubbles on the surface and the surface roughness and consequently improve the MSE of the Ellipsometry fit slow annealing with temperatures ramped up and down for 10 minutes each instead of 30 seconds was used for pure  $\text{Al}_2\text{O}_3$  samples annealed at  $650^\circ\text{C}$  and  $900^\circ\text{C}$ .

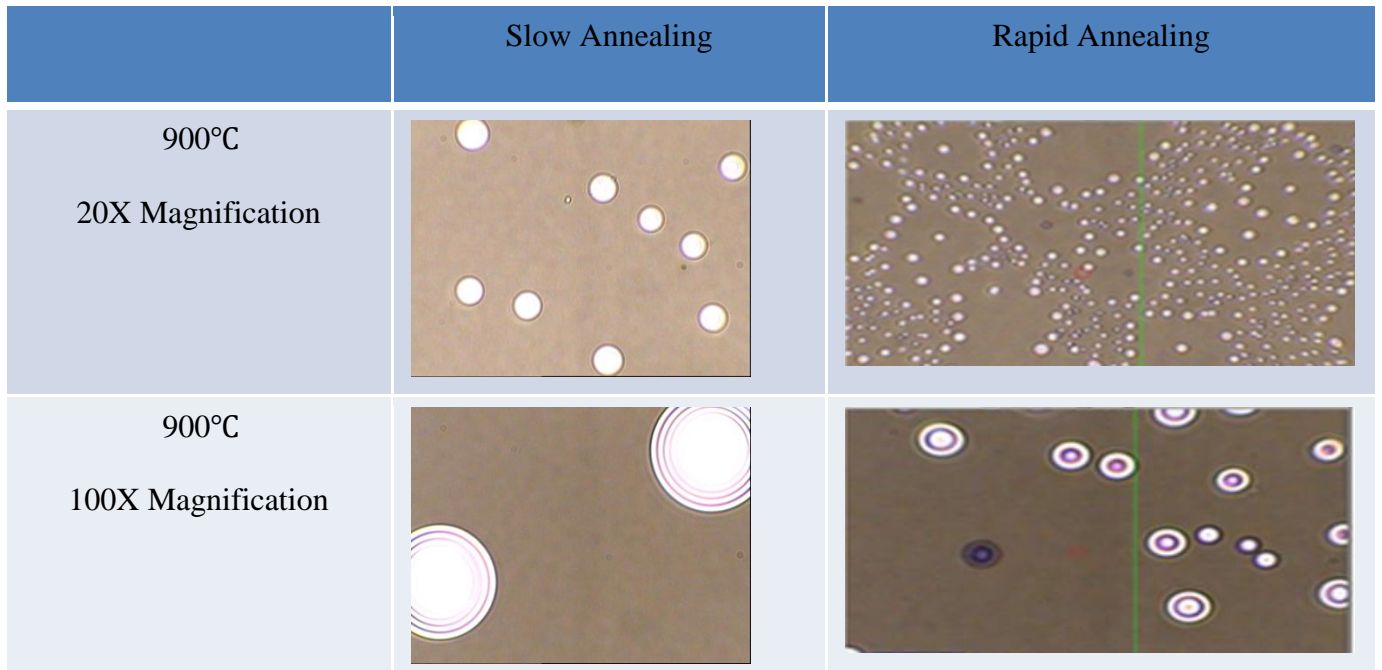


## Slow Anneal at 900°C



**Figure 17** Slow Annealing Recipes and Graphs

A significant improvement in the reduction of bubbles on the surface was observed when slow anneal with temperature ramp up time of 10 minutes was used instead of 30 seconds. This also led to improvement of MSE in ellipsometry as expected.



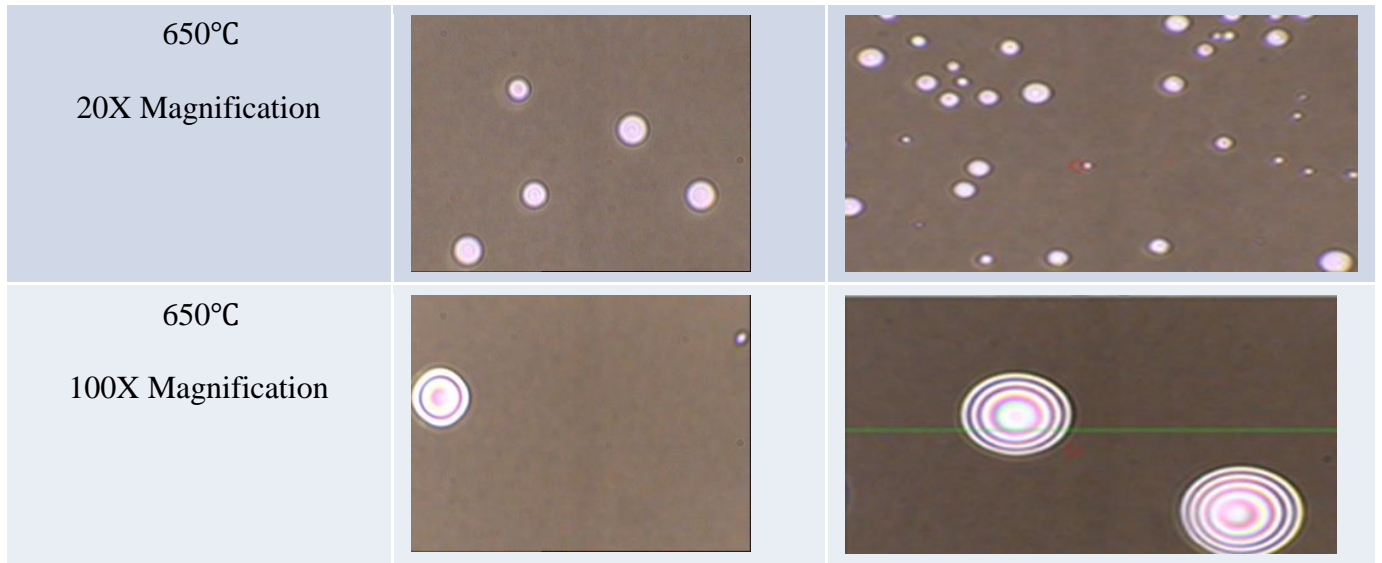


**Table 3** 20X Magnified Microscopic Images showing effect of Slow anneal and Rapid Anneal

### 3.2.2. General Oscillator (GenOsc) Method

GenOsc is a method of forming dispersion equations which contain one or more oscillators of various kinds. It can describe absorption band. Some of the oscillators it supports are Lorentz oscillator, Gaussian oscillator, Tauc-Lorentz oscillator, Drude oscillator, etc. For many oscillators, the values of  $\epsilon_2$  are described by an equation and  $\epsilon_1$  is obtained by a Kramers-Kronig transformation. Lorentz oscillator approaches 0 faster on both sides of the band when compared to the Gaussian oscillator (but both oscillators are symmetric in the  $\epsilon_2$  representation). In Lorentz and Gaussian oscillators, the absorption band is characterized by photon energy ( $E_n$ ) at the center of the band, broadening (Br) parameter (sometimes FWHM (Full Width at Half Maximum)) and amplitude (Amp), maximum value of  $\epsilon_2$ . Tauc-Lorentz Oscillator is a 4 parameter oscillator (extra: energy where  $\epsilon_2$  goes to 0), it is asymmetric (goes to 0 at one end). Drude oscillator is simply a Lorentz oscillator where the energy center is 0.

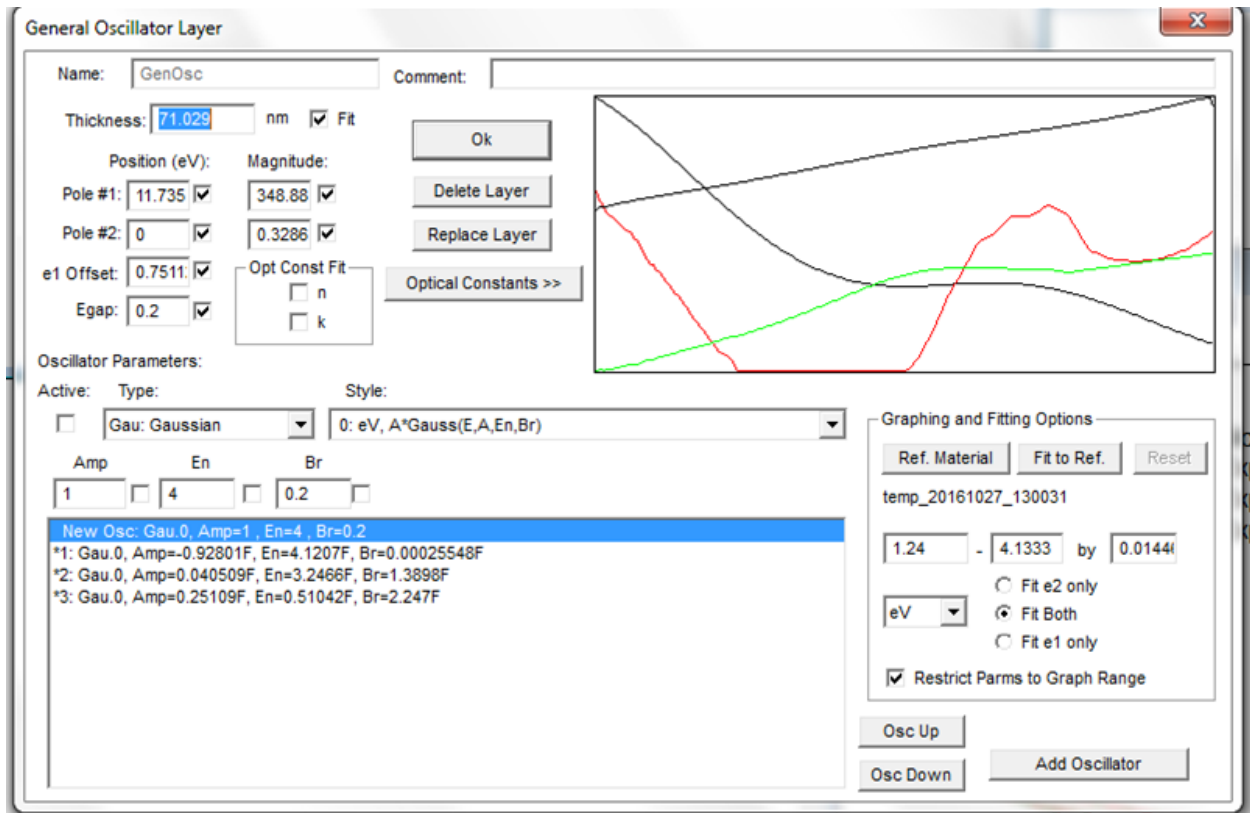


**Figure 18** Ellipsometry MSE improvement: GenOsc Model with three Oscillators for Pure  $\text{Al}_2\text{O}_3$  annealed at  $900^\circ\text{C}$

### 3.2.3. Accounting for Surface Roughness

Surface roughness layer can be accounted for in VASE using void or intermix layers. Surface roughness layer is a mixture of void and the material below in the ratio of 50:50. The surface roughness layer (srough.mat) works well for small roughness (1-10nm thick) on absorbing or high-index films. Roughness at this level has the effect of lowering the optical density at the surface. Intermix layer is a mixture of the material above and material below in the ratio of 50:50. Ellipsometry is not as sensitive to intermix as it is to roughness, because real intermixing typically has less optical contrast and real intermixing is buried below at least one layer. Void layer represents air with constant  $n=1$  and  $k=0$  at all wavelengths. Using Intermix layer instead of surface roughness layer makes the fit worse in this project and surface roughness is more pertinent to the requirement, so it can be concluded that surface roughness is better in this case.

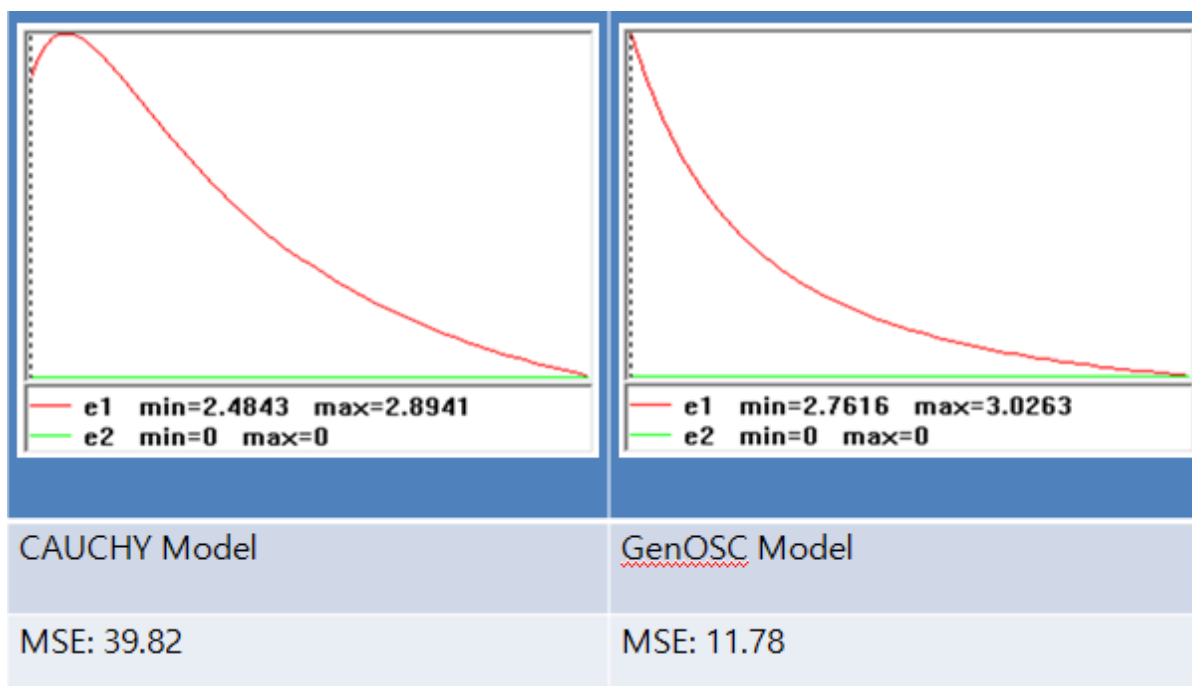


**Table 4** Ellipsometry fit improvement of Al<sub>2</sub>O<sub>3</sub> annealed at 900°C

After incorporating these improvements the ellipsometry data results obtained is summarized in Table 5 and description of each sample number is given in Table 6 and Figure 19 graphically summarizes the Ellipsometry results of thin film characterization.

Sample Number	Value at 630 nm				Thickness (nm)	MSE	Roughness	Annealing Temperature (°C)	Total thickness= Thickness + (0.5*Roughness)
	e1	e2	N	k					
1	3.3650923	0.0423161	1.8344551	0.0115337	118.650	9.335	1.509	150	119.405
2	3.7038725	0.0031159	1.9245449	0.0008095	98.895	1.745	2.772	400	100.281
3	4.1840421	0.0150105	2.0454964	0.0036692	79.768	2.824	4.114	650	81.825
4	4.3235616	0.0902047	2.0794307	0.0216897	76.534	4.994	6.854	900	79.961
5	2.6376515	0.0000000	1.6240848	0.0000000	62.751	1.035	0.000	150	62.751
6	2.6429382	0.0014059	1.6257116	0.0004324	62.267	1.932	0.000	400	62.267
7	2.5146122	0.0370365	1.5857959	0.0116776	64.608	4.568	0.000	650	64.608
8	2.6702742	0.0443097	1.6341536	0.0135574	54.763	10.650	0.235	900	54.881
9	3.3315690	0.0020385	1.8252587	0.0005584	69.599	7.465	0.000	150	69.599
10	3.3444265	0.0019509	1.8287774	0.0005334	69.914	7.077	0.000	400	69.914
11	3.3884860	0.0041616	1.8407844	0.0011304	70.187	3.379	0.000	650	70.187
12	3.5139554	0.0000000	1.8745547	0.0000000	67.537	1.253	0.000	900	67.537
13	3.2189124	0.0016531	1.7941328	0.0004607	69.468	2.724	0.000	400	69.468
14	3.2025963	0.0025369	1.7895801	0.0007088	67.478	1.496	0.000	650	67.478
15	3.4406387	0.0000000	1.8548959	0.0000000	70.271	7.700	0.000	400	70.271
16	3.4501168	0.0000000	1.8574490	0.0000000	66.902	5.865	0.000	650	66.902

**Table 5** Ellipsometry Data Summary

S.No.	Material (50 nm)	Annealing temperature
1	Pure HfO <sub>2</sub>	150 °C
2	Pure HfO <sub>2</sub>	400 °C
3	Pure HfO <sub>2</sub>	650 °C
4	Pure HfO <sub>2</sub>	900 °C
5	Pure Al <sub>2</sub> O <sub>3</sub>	150 °C
6	Pure Al <sub>2</sub> O <sub>3</sub>	400 °C
7	Pure Al <sub>2</sub> O <sub>3</sub>	650 °C
8	Pure Al <sub>2</sub> O <sub>3</sub>	900 °C
9	HfO <sub>2</sub> + Al <sub>2</sub> O <sub>3</sub> : 3 5 5 5 2	150 °C
10	HfO <sub>2</sub> + Al <sub>2</sub> O <sub>3</sub> : 3 5 5 5 2	400 °C
11	HfO <sub>2</sub> + Al <sub>2</sub> O <sub>3</sub> : 3 5 5 5 2	650 °C
12	HfO <sub>2</sub> + Al <sub>2</sub> O <sub>3</sub> : 3 5 5 5 2	900 °C
13	HfO <sub>2</sub> + Al <sub>2</sub> O <sub>3</sub> : 3 1 1 1 2	400 °C
14	HfO <sub>2</sub> + Al <sub>2</sub> O <sub>3</sub> : 3 1 1 1 2	650 °C
15	HfO <sub>2</sub> + Al <sub>2</sub> O <sub>3</sub> : 5 10 10 10 5	400 °C
16	HfO <sub>2</sub> + Al <sub>2</sub> O <sub>3</sub> : 5 10 10 10 5	650 °C

Table 6 Sample Description

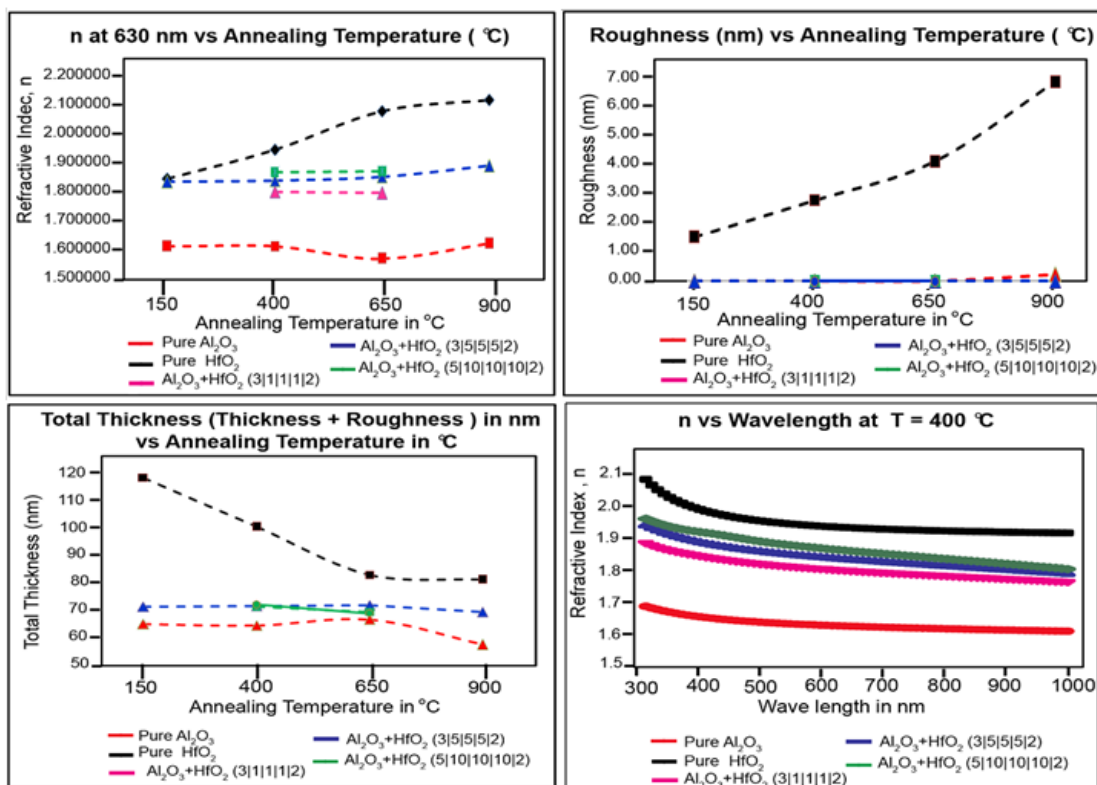


Figure 19 Graphical Summary of Thin Film Characterization results using Ellipsometry

As can be seen from the above data, the dielectric constant and refractive index values of Hafnium Oxide increases with annealing temperature, indicating a densification process which happens due to crystallization and reduction of voids in the structure and due to expulsion of trapped air and other impurities. This is validated by the thickness measurement values too (thickness is observed to decrease with increasing annealing temperatures). It is observed that the increase in dielectric constant and refractive index value and the corresponding decrease in the thickness are steeper for annealing temperatures less than 650°C and the slope is lesser beyond that. This is because the crystallization of Hafnium Oxide occurs in temperatures less than 650 °C and once crystallization occurs there is lesser scope for further densification.

The dielectric constant and refractive index values of Aluminum Oxide increases slightly with annealing temperature initially and then decreases, before increasing again, this could be due to initial expulsion of trapped gases leading to a slight decrease in volume (densification) and probably some phase change leading to a slight increase in the volume at around 650°C. It could be an erroneous measurement or bad fit due to the presence of bubbles on the surface, but it is little less likely since other fits and the Filmetrics data also show the same pattern). As the annealing temperature is increased to 900°C Aluminum Oxide starts to crystallize and densifies.

The dielectric constant and refractive index curves for samples containing both Aluminum Oxide and Hafnium Oxide have a very small slope till the annealing temperature of 650°C, since the two dielectrics act in the opposite directions (one densifies while the other rarifies). Beyond 650°C, both Aluminum Oxide and Hafnium Oxide crystallize and the overall coating density increases leading to an increase in dielectric constant and refractive index values and a decrease in thickness (with a steeper slope). The MSE value increases with annealing temperature in the pure Aluminum Oxide and Hafnium Oxide samples, but is found to decrease with increase in annealing temperature for samples containing both Aluminum Oxide and Hafnium Oxide.

For pure HfO<sub>2</sub> sample roughness increases with annealing temperature from 400°C (pointing to its crystallization), for samples containing both dielectrics roughness is mostly 0 thus pointing to the fact that the nanolaminate coating prevents crystallization of both HfO<sub>2</sub> and Al<sub>2</sub>O<sub>3</sub> layers, for Al<sub>2</sub>O<sub>3</sub> for lower temperatures roughness is 0, and for higher temperatures (at 900°C) it exhibits a small roughness, this could be due to onset of crystallization and/or due to the bubbles on the surface.

### 3.3. Filmetrics Measurements

Filmetrics using spectral reflectance measures the amount of light reflected from a thin film over a range of wavelengths, with the incident light normal (perpendicular) to the sample surface. This method is much simpler and less expensive than ellipsometry, but it is restricted to measuring less complex structures and is less accurate. In this project thickness of the coating of the pure Aluminum Oxide and Hafnium Oxide was measured using Filmetrics and compared with ellipsometry data. A sample fitting of pure Aluminum Oxide annealed at 150°C is shown in Figure 20.

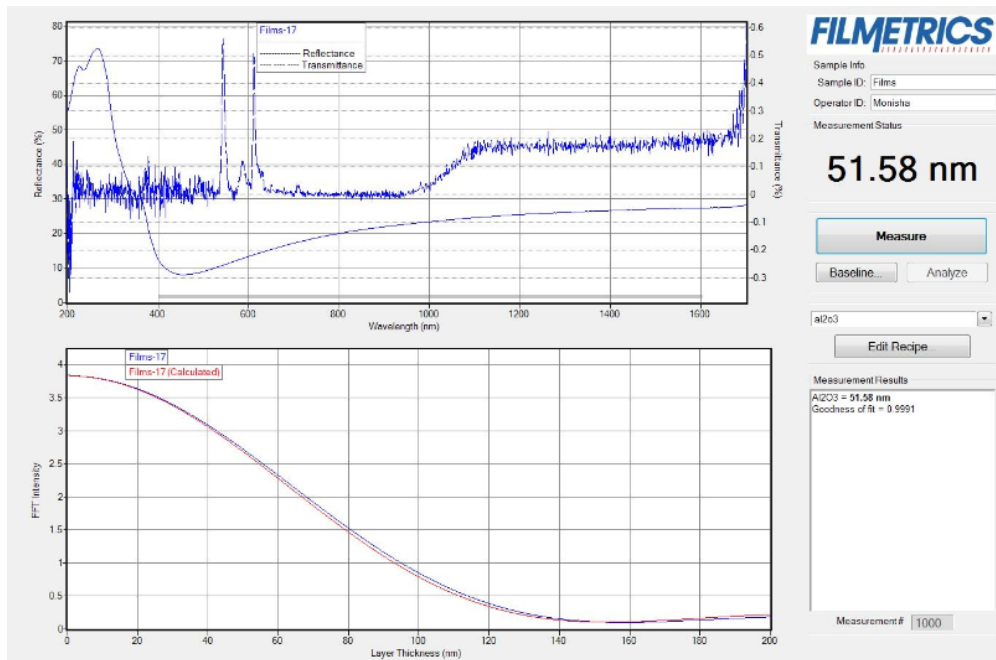


**Figure 20** Filmetrics Measurement of pure Al<sub>2</sub>O<sub>3</sub> annealed at 150°C

<b>Sample Number</b>	<b>Ellipsometry Thickness (nm)</b>	<b>Filmetrics Thickness (nm)</b>	<b>Annealing Temperature (°C)</b>
1	116.633	114.1	150
2	99.934	103	400
3	80.97	86.07	650
4	77.332	82.12	900
5	62.693	51.58	150
6	62.183	51.76	400
7	64.38	53.17	650
8	63.484	48.54	900

**Table 7** Comparison of thickness measured using ellipsometry and Filmetrics

The trends of thickness variation for different annealing temperatures are fairly consistent between ellipsometry and Filmetrics measurements. The difference between the thickness measured using ellipsometry and Filmetrics is due to the difference in the principle of measurement between the 2 methods. Ellipsometry measurements are more accurate than Filmetrics measurements by virtue of its principle of measurement.

### **3.4. Raman Spectroscopy**

Raman spectroscopy is a molecular spectroscopy method which observes the inelastically scattered light and allows for the interrogation and identification of vibration (phonon) states of molecules. Thus Raman spectroscopy is a label-free detection method that provides invaluable analytical data for molecular finger printing as well as monitoring changes in molecular bond structure (example.: state changes and stresses & strains). In this project it is used to determine the crystallization state of the samples at different annealing temperatures. The Raman spectroscopy results are shown in Figure 21.

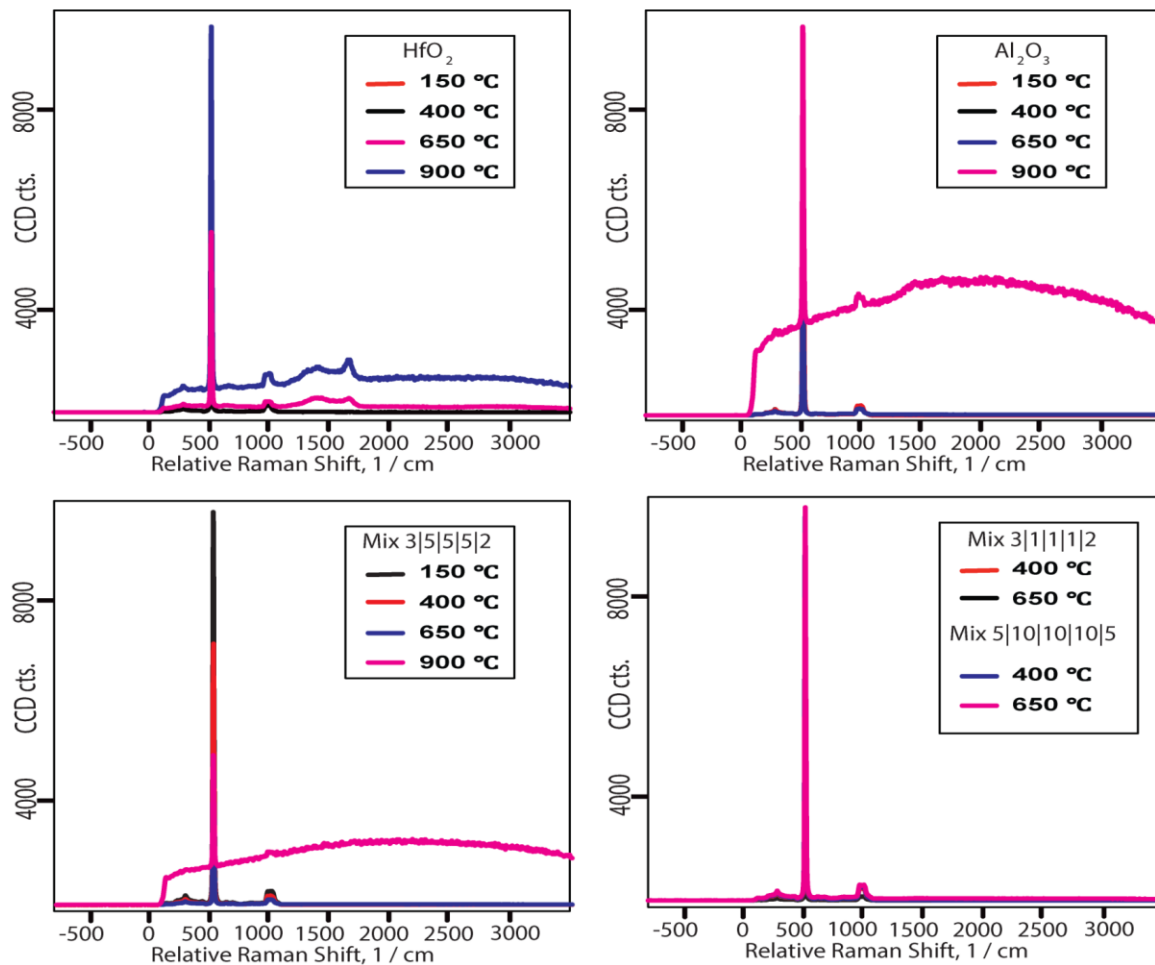


**Figure 21** Raman Spectroscopy data showing crystallization state of the samples

In the Raman spectra for all the samples the dominant peaks are of the silicon substrate at  $295\text{ cm}^{-1}$ ,  $515\text{ cm}^{-1}$  and  $950\text{ cm}^{-1}$  respectively. Even at a magnified scale, there is no sign of crystalline  $\gamma$  phase Aluminum Oxide. This indicates that Aluminum Oxide still has an amorphous morphology. This result is consistent with the existing literature and can also be verified using XRD measurements. However for the pure Aluminum Oxide sample annealed at  $900^\circ\text{C}$  though no sign of Aluminum Oxide peak is evident explicitly, the sample exhibited a broadened peak. This peak is not observed for the Aluminum Oxide samples annealed at lower temperatures. This broadened peak is related to the photoluminescence of the sample. The photoluminescence peak of Aluminum Oxide red shifts at annealing temperatures above  $800^\circ\text{C}$ . This causes the peak to

reach the detection range of the detector. The photoluminescence effect is a result of SRH radiative recombination of carriers assisted by Oxalic impurities. This effect will also be observed for higher annealing temperatures of Aluminum Oxide. Likewise photoluminescence effect is observed for pure Hafnium Oxide samples annealed at 650°C and 900°C, pointing to the crystallization of Hafnium Oxide at these annealing temperatures. For the samples containing a mixture of both Aluminum Oxide and Hafnium Oxide photoluminescence does not start until annealing at 900°C and the exhibited photoluminescence is lesser than the once observed for pure Aluminum Oxide sample. Thus the crystallization of both Aluminum Oxide and Hafnium Oxide is suppressed in a nanolaminate structure containing both the dielectrics. This in turn reduces the permeation of corrosive water and ions through the nanolaminate coating, enhancing the long-term stability of the plasmonic structure underneath.

### **3.5. Thin Film Stability Test**

Initially pure  $\text{Al}_2\text{O}_3$  films, pure  $\text{HfO}_2$  films and films consisting of a mixture of  $\text{Al}_2\text{O}_3$  and  $\text{HfO}_2$  of 12 nm thickness were tested in a 10X PBS solution (10 times accelerated testing) at 37°C (physiological temperature) for 7 days as part of thin film characterization. Film thickness and refractive index (indicator of film's density) were measured using single frequency Ellipsometry at 650 nm. It was observed that  $\text{Al}_2\text{O}_3/\text{HfO}_2$  composite thin films that were annealed at temperatures above 350°C displayed very good bio-stability, with only the top  $\text{Al}_2\text{O}_3$  layer exposed to PBS being etched away. PBS stands for Phosphate Buffered Saline. It is a salty solution of sodium chloride and sodium phosphate. The buffer in the solution helps it maintain a constant pH value; the 10X PBS solution has a pH value of 7.4 while the 1X PBS solution has a pH value of 7.2. The osmolarity and ion concentration of the PBS solution matches that of the human body and hence the solution is used to emulate the physiological environment for the

samples in this project. Pure  $\text{Al}_2\text{O}_3$  and  $\text{HfO}_2$  films had an increase in thickness after they were soaked in PBS for 7 days. This indicates that these films swelled in physiological environments.

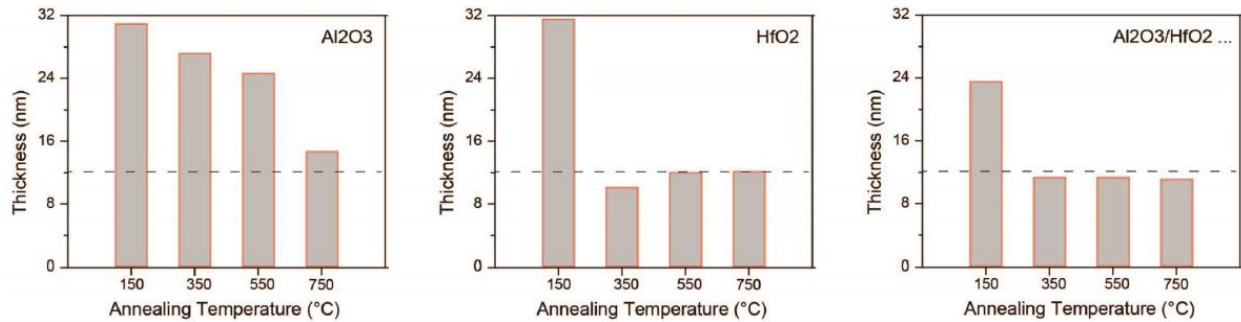


**Figure 22** Preliminary Results after soaking in 10X PBS at 37°C for 7 days. Dashed line indicates initial film thickness

Pure  $\text{Al}_2\text{O}_3$  and pure  $\text{HfO}_2$  films show a significant decrease in their refractive index after being exposed to PBS for 7 days, while the refractive index of the composite films consisting of both  $\text{Al}_2\text{O}_3$  and  $\text{HfO}_2$  that were annealed at temperatures above 350°C did not change. This demonstrates the stability of the composite film's optical and physical quality in the physiological environment. The decrease in refractive index reflects the decrease of the film's density due to the films becoming more porous (due to swelling in physiological environment). This is not good for increasing the stability of the film, since more ions can diffuse through and affect the material underneath.

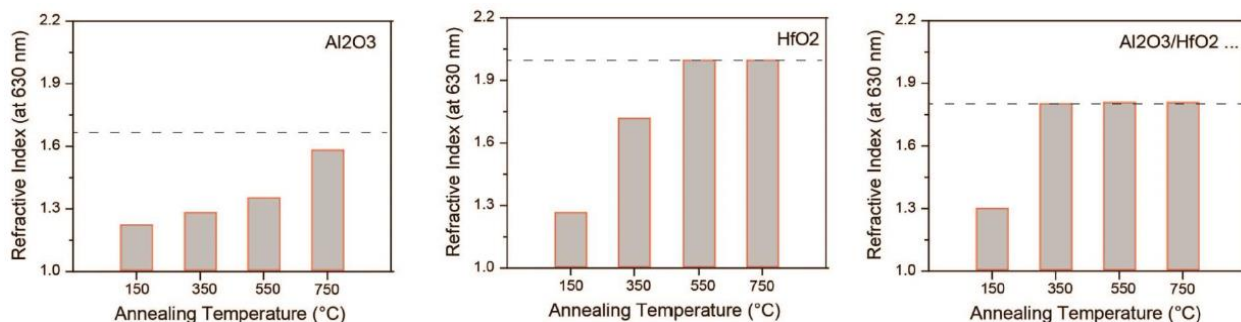


**Figure 23** Preliminary Results after soaking in 10X PBS at 37°C for 7 days. Dashed line indicates initial refractive index

## 4. Fabrication

### 4.1. Self-Assembly Process: Nano-Sphere Lithography (NSL)

Nanosized plasmonic structures can be implemented using lithographic techniques in the top-down approach like Electron Beam (EB), Focused Ion Beam (FIB), Extreme Ultraviolet (EUV) and Atomic Force (AFM) and by self-assembly process (a process by which disordered parts build an ordered structure through local chemical, physical or biochemical interactions involving surface forces, electrostatic forces, hydrophilic / hydrophobic chemical interactions, etc.). Some self-assembly processes that can be used for the fabrication of SPP devices are Langmuir–Blodgett (LB), electrostatic self-assembly techniques, chemical self-assembly methods, monolayer-protected clusters (MPC), self-assembled monolayers (SAM) and Biomolecular self-assembly techniques [33].

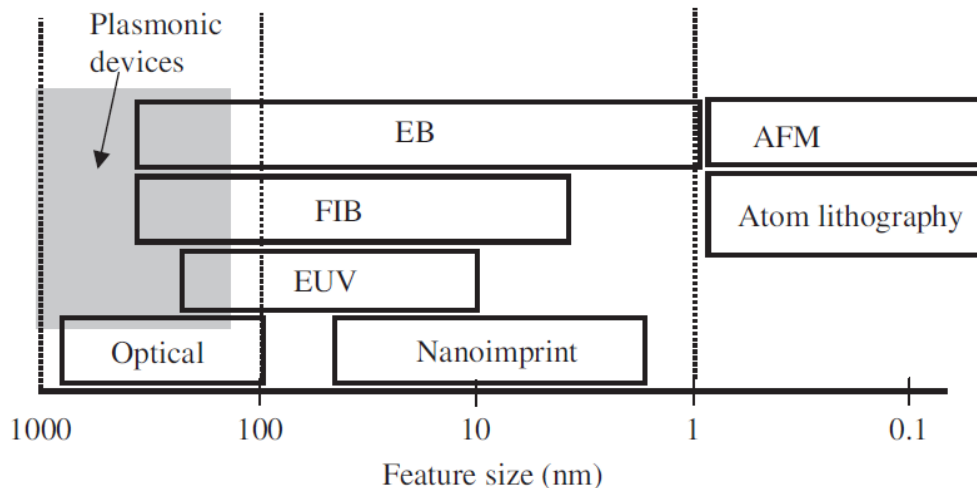


**Figure 24** Nanoscale characteristics of the main lithographic techniques in the top-down approach. Dragoman, “Plasmonics: Applications to nanoscale terahertz and optical devices, *Progress in Quantum Electronics* 32 (2008) 1–41. Used under fair use, 2017

Nanosphere Lithography (NSL) is a simple, bench-top, materials generic approach to produce high quality Periodic Particle Array (PPA) nanostructures. Using different bead diameters the separation distance between the openings can be tuned. NSL involves the preparation of a

colloidal crystal mask (CCM) made of nanospheres and the deposition of the desired material through the mask. The mask is then removed and the layer keeps the ordered patterning of the mask interstices. Advantages of Nanosphere Lithography (NSL) are that it is compatible with wafer-scale process, it has the potential to manufacture a wide variety of homogeneous 1D, 2D and 3D nanostructures [34] and it does not require expensive equipment to yield structures with comparable resolution while the conventional lithographic techniques have the disadvantages of high equipment cost, the process is comparatively complex, optical lithographic processes are limited in final resolution by the wavelength of the light used to expose the photoresist. NSL also provides excellent control of interparticle spacing and out-of-plane height to the level of a few nanometers. The quality and thickness of nanosphere mask, ensuring a monolayer formation can be controlled using spin coating by controlling the spin speed and size of the nanospheres.

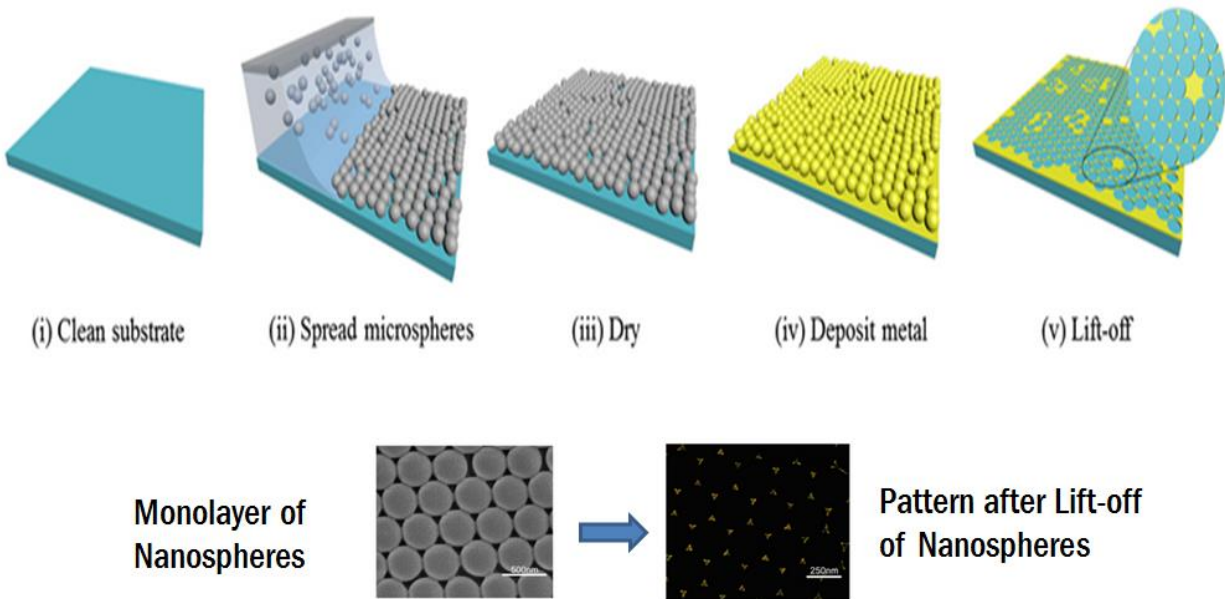


**Figure 25** General Schematics of NSL. “Nanoparticle fabrication by geometrically confined nanosphere lithography”, J. Micro/Nanolith. MEMS MOEMS. 12(3), 031106 (Jul 26, 2013). Used under fair use, 2017

The challenges encountered while trying to fabricate the plasmonic array structure using NSL are: increasing packing density of polystyrene beads, preventing cluster formation and ensuring

formation of monolayer of nano-spheres. To solve this experiments were carried out by varying the solution composition (methanol the PS solvent + PS (Polystyrene) + Triton-X the surfactant used to prevent aggregation of PS), spin speed, spin time and the amount of the solution used using the various available literature sources. The solution that gave the best density coverage was using 350  $\mu\text{L}$  for each sample from a solution containing 6 ml methanol, 3  $\mu\text{l}$  Triton-X and 105  $\mu\text{L}$  of 300 nm PS and the optimized spin-coating recipe used had the following 3 steps [35]:

- Step 1: 400 RPM for 10 seconds (to spread the beads solution evenly)
- Step 2: 800 RPM for 2 minutes (to spin away the excess bead solution)
- Step 3: 1400 RPM for 10 seconds (to spin off the excess materials from the edges)



**Figure 26** Initial attempts showing multilayer formation instead of the desired mono-layer PS mask

The surfaces fabricated using the above recipe resulted in substrates that strongly diffracted under room light to reflect a purple opal color, meaning a mono-layer formed. Limitations of NSL are that only a single layer of patterned features can be generated on a substrate at a time, it can yield only hexagonally close packed pillar patterns of limited domain size with diameters of tens of microns and uniformity over large areas is poor, this limits NSL's use to research purposes.



**Figure 27** 20X magnification microscope image of uniform PS mask distribution

To overcome these limitations another method called Hole-mask Colloidal Lithography (HCL) can be used. In contrast to NSL, a sparse monolayer of colloidal particles defines the etch mask and a sacrificial layer combined with a thin film mask with nanoholes is present in HCL. The average spacing and diameters of the holes are determined by the separation distance and size of the removed colloidal particles. The etching selectivity of the double-layer film (hole-mask + polymer) leads to a partial undercut of the polymer film, which is perfectly suited for lift-off processing. The optimized recipe prepared is as follows and is shown in Figure 28. The silicon wafers were initially cleaned with Acetone, IPA and water at 4000 RPM for 30 seconds. The cleaned samples were baked at 250°C for 15 minutes and coated with 1 layer of omnicoat (to aid in the lift-off of SU8) and 5% SU-8 (sacrificial layer). The 2 step recipe for their coating is: 500 RPM for 5 Seconds, followed by 3000 RPM for 30 seconds. After coating with Omnicoat the sample was baked at 180°C for 1 minute. After coating with SU-8, the sample was baked at 180°C for 5 minutes. The sample was exposed to UV for 5 seconds. The optimized solution composition and spin-coat recipe described above was used to coat the nano-spheres.

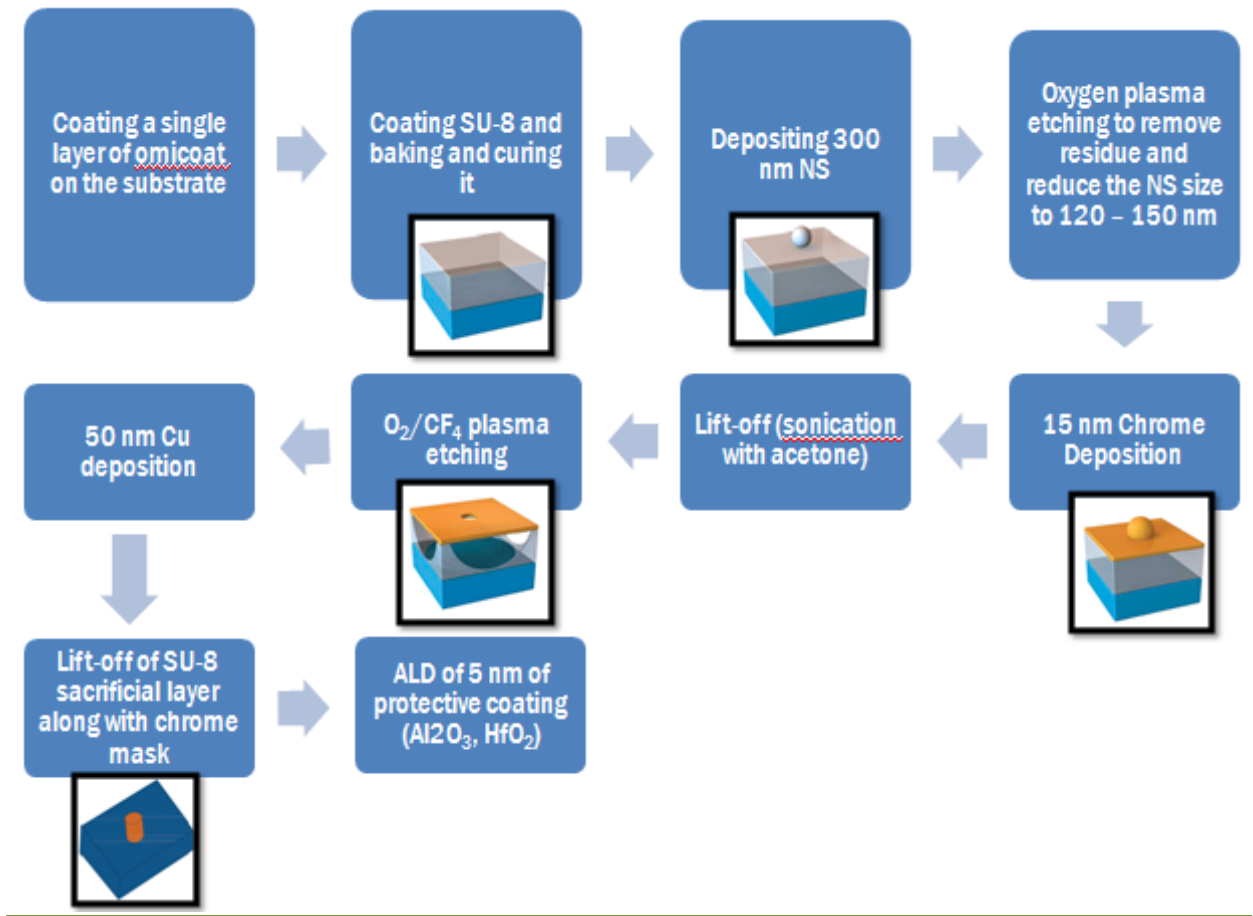


**Figure 28** Schematics of the HCL fabrication scheme

The advantages of HCL are that it gives larger area coverage, it allows for independent control over feature size and spacing, it can be used to produce elongated structures instead of discs simply by tilting the sample, with respect to the evaporation source, during the hole mask deposition [36], high fabrication speed (the fabrication time does not scale with area), simplicity (the nanofabrication process is reduced down to conventional material deposition and reactive ion etching) and thus economical viability, the substrate independence of this method increases the range of geometries and range of materials this method can be used on. The final samples were however fabricated using a top-down process, which is discussed in the next section.

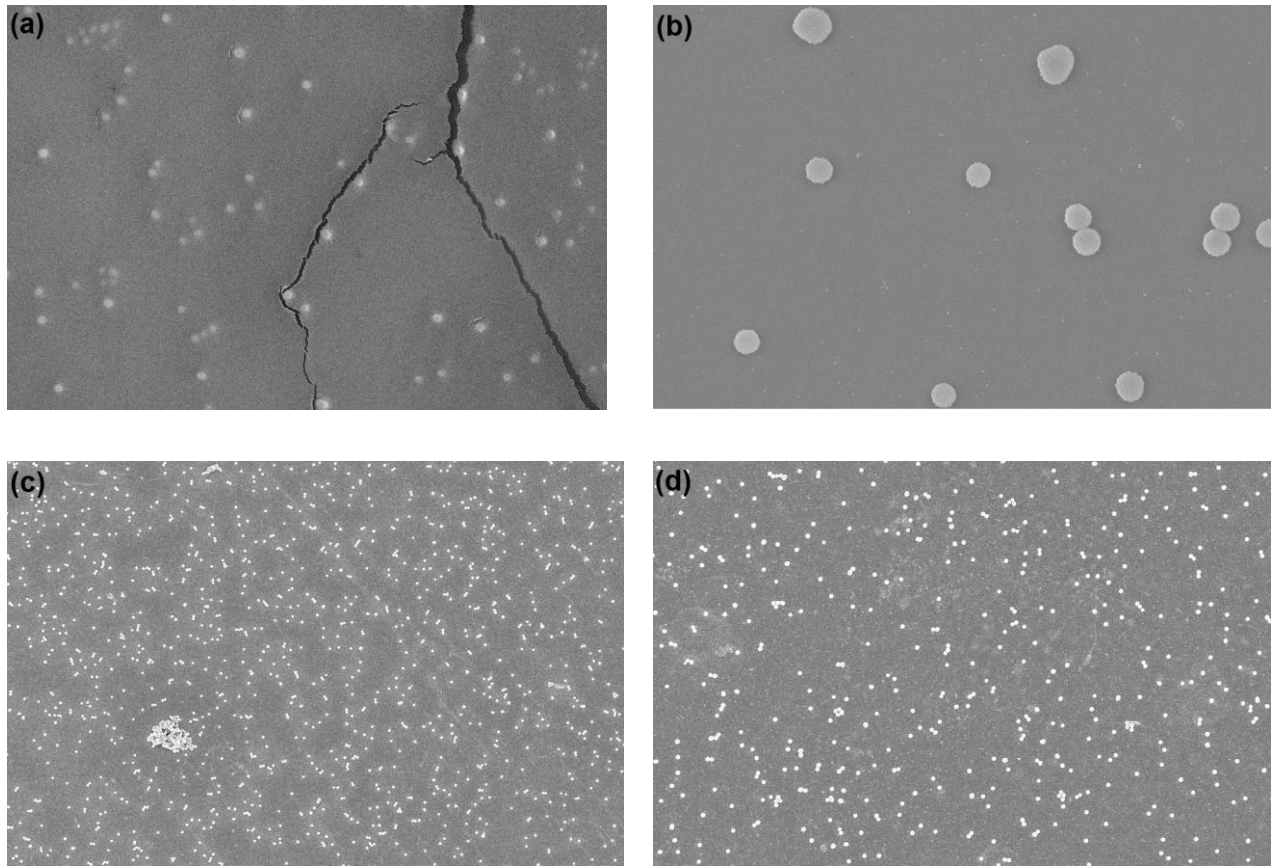


**Figure 29** SEM Images of deposited Polystyrene beads. (a) 11.2 KX magnification image showing formation of crack in the substrate upon etching due to insufficient curing of the substrate, it was fixed by hard baking after SU8 coating at 180°C for 5 minutes. (b) 40.62 KX magnification of PS deposited on substrate (c) and (d) 5.01 KX magnification images of PS distribution (c) shows formation of a cluster, (d) shows fairly uniform distribution

#### **4.2. Top-down approach: Using E-Beam Deposition**

In order to test the effect of coating material, thickness, composition of nano-laminate structure and annealing temperature (crystallinity state of coating components) on the long term stability of protective coatings in corrosive physiological environments and compare their protective coating properties, various samples with different thicknesses, annealing temperatures, coating materials and compositions as shown in Table 8 were fabricated.

Samples for the Reliability Test				
Thickness 5 nm	T= 150 °C (Both HfO <sub>2</sub> and Al <sub>2</sub> O <sub>3</sub> amorphous)	T = 250°C	T=350 °C	T = 600 °C (HfO <sub>2</sub> is crystalline, Al <sub>2</sub> O <sub>3</sub> is Amorphous)
			3 1 1 1 2 (25, 26)	3 1 1 1 2 (27, 28)
	3 5 5 5 2 (17, 18)	3 5 5 5 2 (23, 24)	3 5 5 5 2 (19, 20)	3 5 5 5 2 (21, 22)
			5 10 10 10 5 (29 & 30)	5 10 10 10 5 (31 & 32)
	Pure Al <sub>2</sub> O <sub>3</sub> (9, 10)	Pure Al <sub>2</sub> O <sub>3</sub> (15, 16)	Pure Al <sub>2</sub> O <sub>3</sub> (11, 12)	Pure Al <sub>2</sub> O <sub>3</sub> (13, 14)
	Pure HfO <sub>2</sub> (1,2)	Pure HfO <sub>2</sub> (7,8)	Pure HfO <sub>2</sub> (3,4)	Pure HfO <sub>2</sub> (5,6)
Thickness 1 nm			3 5 5 5 2 (33, 34)	3 5 5 5 2 (35)
Thickness 3 nm			3 5 5 5 2 (36, 37)	3 5 5 5 2 (38, 39)

**Table 8** Samples fabricated for testing in PBS solution. The numbers within parenthesis denote the label given to the sample

The samples 1, 3, 5, 8, 9, 11, 14, 16, 17, 20, 22, 24, 25, 27, 29, 31, 33, 35, 36 and 39 were tested in 1X PBS solution with a pH value of 7.2 at 37°C. The samples 2, 4, 6, 7, 10, 12, 13, 15, 18, 19, 21, 23, 26, 28, 30, 32, 34, 37 and 38 were tested in 1X PBS solution with a pH value of 7.2 at 85.1°C. A two step process using e-beam deposition was used for the fabrication of the Periodic Particle Array (PPA) structure. The protective coatings were deposited using Atomic Layer Deposition (ALD) and then annealed at different temperatures. The fabrication process is shown in Figure 30.

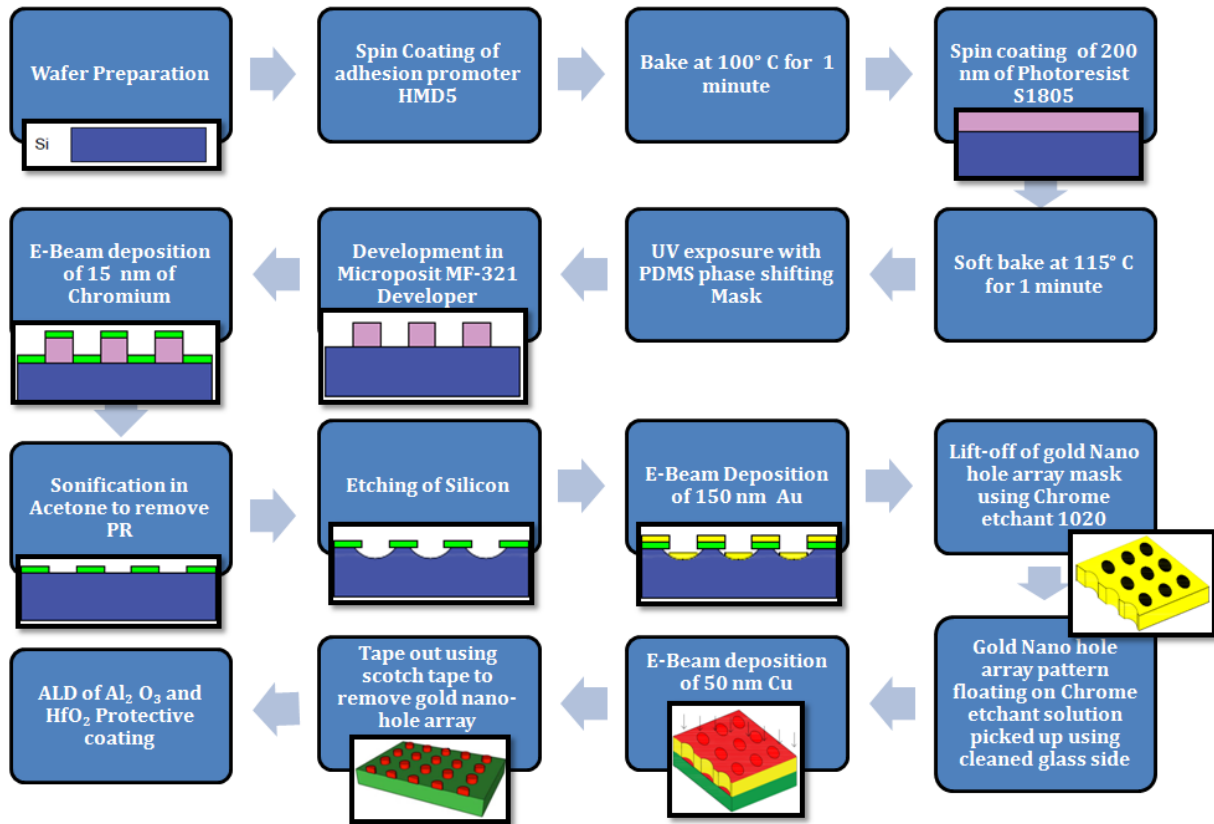


**Figure 30** Schematics of the Fabrication Process using e-beam deposition

The wafer was cleaned with acetone, IPA and DI water at 4000 RPM for 30 seconds on the spin coater and baked for 15 minutes at 250°C. Adhesion promoter Hexamethyldisilazane (HMDS) was spin-coated on top of the cleaned wafer and baked at 100 °C for 1 minute. 200 nm of positive photoresist S1805 was deposited on top of this by spin coating. The recipe used for coating of HMDS and S1805 was spinning at 500 RPM for 5 seconds to distribute the solution on the wafer followed by spinning at 3000 RPM for 30 seconds to spin off the excess solution. It was followed by a soft bake at 115 °C for 1 minute. The spin coater used was from Laurell Technologies Corporation and baking was done using IKA C-MAG HP 7 Hot Plate. The prepared sample was exposed to flood type UV exposure for 0.1 second using a PDMS phase shifting mask (Phase-shift masks are photomasks that use the positive and negative interference generated by phase differences to improve image resolution in photolithography) and Karl Suss' MA 6 / BA 6 mask

aligner. The wafer was dipped and shaken in the developer solution (Microposit MF-351) till a greenish blue diffraction pattern appeared. 15 nm of chrome was deposited by e-beam deposition using PVD 250 from Kurt J. Lesker Company at a deposition rate of  $0.5\text{\AA}/\text{second}$ . The PR was removed using sonication with acetone. Vevor Digital Ultrasonic Cleaner (Model: PS – 60A) is used for the process. The deposited chrome layer acts as mask for RIE (Reactive Ion Etching) of Silicon for 30 seconds with  $\text{O}_2$  and  $\text{CF}_4$  in the ratio of 1:6. RIE was performed using Samco's Compact RIE system. 150 nm of Au was deposited using e-beam deposition with the growth rate of  $1.5\text{\AA}/\text{second}$ . The silicon substrate containing the gold nano-hole array pattern was diced into samples of required size and quantity. The prepared sample was immersed in chrome etchant 1020 (ceric ammonium nitrate) for 2 to 3 days till the gold nano-array pattern gets detached from the silicon substrate (soak duration for lift-off depends on the hole size in the structure, the larger the holes, more the chrome etchant that can seep through and more the etching and consequently lesser the duration to lift-off).

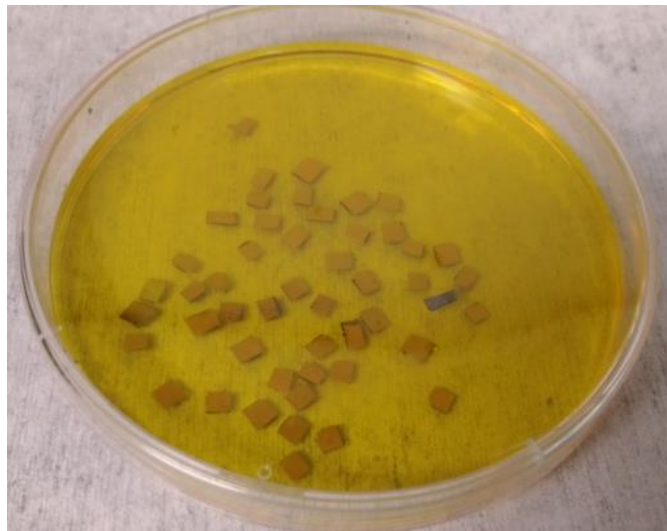


**Figure 31** Fabricated samples soaked in chrome etchant 1020. It can be seen that some Gold nanohole array masks are detached from the substrate

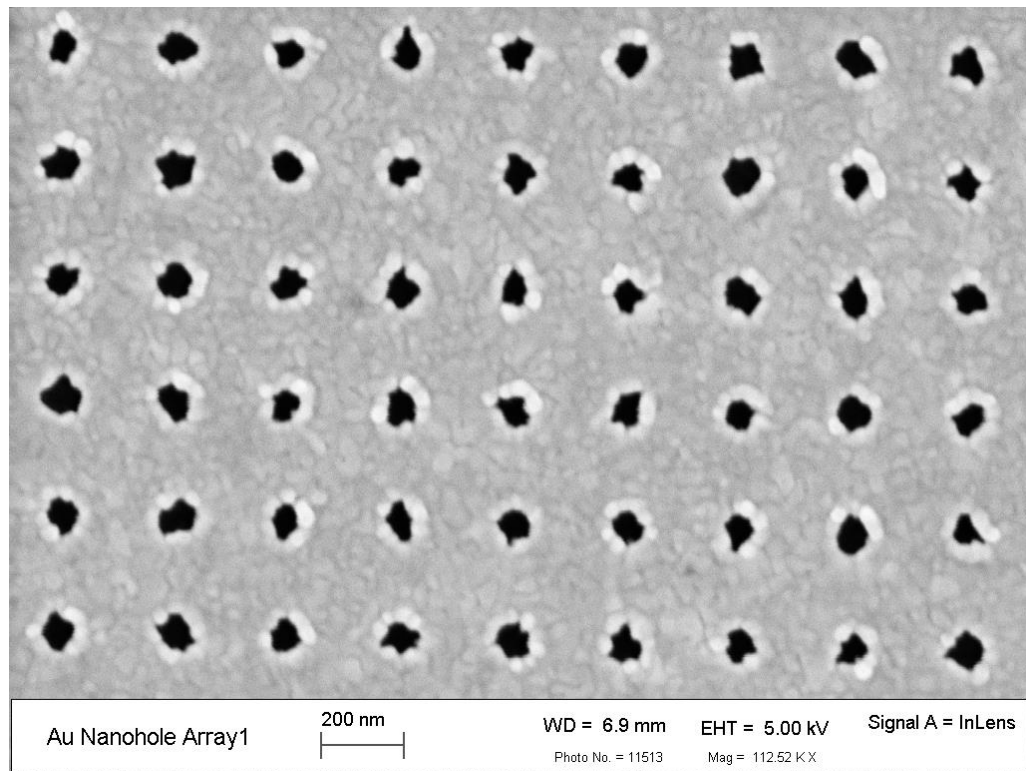


**Figure 32** 112.52KX magnification SEM image of Fabricated Hole Mask Array

The glass substrate on which the mask was to be transferred was subject to oxygen plasma treatment (20 W, 5 s, 50 sccm) and ensured to be hydrophilic (can be inspected by checking the wetting properties of DI water on the glass substrate). The petri dish containing the detached gold nano hole array mask was agitated and the surface tension of the water was used to suspend the gold nano hole array mask from the Silicon substrate. The floating gold nano-hole array mask was scooped up using the prepared glass substrate. The gold nano hole array mask transferred onto the glass substrate was dried using the hand (pipette) blower. When the gold nano hole array mask is scooped up with the glass slide, it can't be allowed to air dry because it would cause wrinkles on the nano mask. After it dried the samples were transferred to a flexible substrate for the e-beam deposition process. 50 nm of Copper was deposited using e-beam deposition. Density of Cu was  $8.92 \text{ g/cm}^3$ , Z-Factor is 0.437, tooling factor which depends on factors like the distance between

the Copper crucible and the chuck is 140. Initial growth rate (to aid in crystal growth) was set to be  $0.2 \text{ \AA/s}$  and eventually the growth rate was set to be  $1.1 \text{ \AA/s}$ .

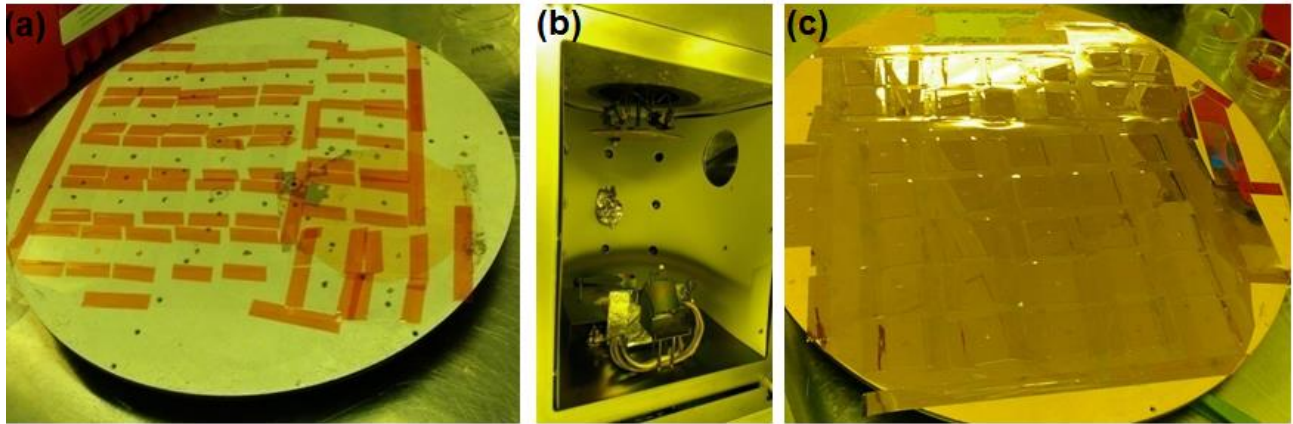


**Figure 33** (a) Samples taped to the chuck to be mounted for e-beam deposition of Cu. (b) Samples mounted inside the e-beam chamber for deposition. The Cu crucible is mounted in the bottom of the chamber. (c) Copper coated samples before tape-out

After Cu deposition the samples are unmounted from the chuck and tape out using scotch tape was done to remove the gold nano-hole array mask exposing the Copper plasmonic structure. The plasmonic nano particle in the PPA has a diameter of 150 nm and a height of 50 nm. The final sample prepared looks as shown in Figure 34.

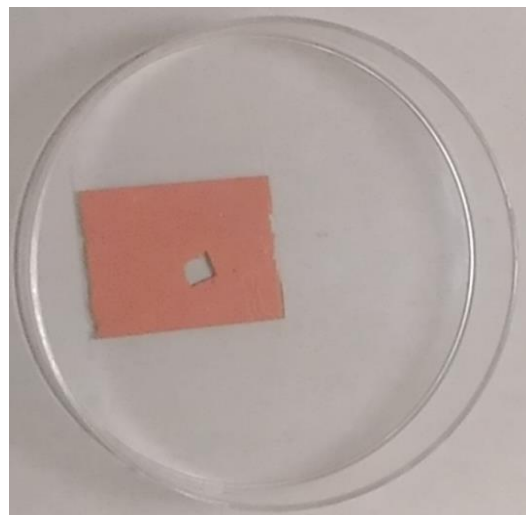


**Figure 34** Fabricated sample in a petri dish. The plasmonic structure is located in the transparent looking square in the center, where the Au nano hole array mask has been removed. The area exhibits diffraction under light

In the first stage of the process negative PR can't be used instead of positive PR (to straight away obtain the nano pillar structure instead of the nano hole structure) because negative PR (SU8) is difficult to remove and the positive PR (S1805) gives better resolution (it is optimized to give a better resolution than SU8).

HfO <sub>2</sub> Coating Recipe				Al <sub>2</sub> O <sub>3</sub> Coating Recipe			
	Instruction	#	Value		Instruction	#	Value
0	Pulse	0	0.015	0	Pulse	0	0.015
1	Wait		20	1	Wait		20
2	Pulse	1	0.15	2	Pulse	2	0.015
3	Wait		30	3	Wait		20
4	Goto	0	50	4	Goto	0	50

**Table 9** Recipe for 150°C growth of Al<sub>2</sub>O<sub>3</sub> and HfO<sub>2</sub> by ALD

The required thickness of Al<sub>2</sub>O<sub>3</sub> and HfO<sub>2</sub> (1 nm, 3 nm and 5 nm) was deposited using ALD to get a conformal layer of protective coating. Various Combinations of the above 2 recipes were used. The ALD chamber was seasoned for 1.5 hours prior to deposition to remove the residue from the previous depositions in the chamber. Protective coatings were deposited by ALD at 150°C. Hafnium Oxide's precursor Tetrakis(Dimethylamido)Hafnium (Hf(NMe<sub>2</sub>)<sub>4</sub>) was heated to 75°C for the process, while the precursor Trimethylaluminum used for Aluminum Oxide and H<sub>2</sub>O (used for deposition of both dielectrics) were used at room temperature.

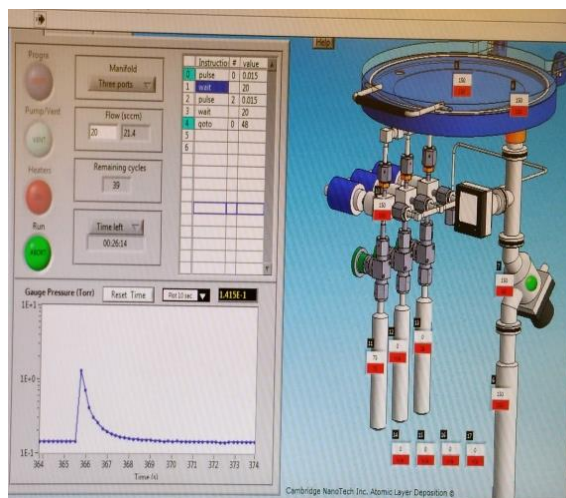


**Figure 35** Cambridge Nano Tech's Savannah ALD software screen used for programming and monitoring the deposition process. Al<sub>2</sub>O<sub>3</sub> deposition is shown here.

A sample ALD deposition process as observed from the Cambridge Nano Tech's Savannah ALD software is shown in Figure 35. Growth rate of pure HfO<sub>2</sub> is 1.01Å / cycle. Growth rate of pure Al<sub>2</sub>O<sub>3</sub> is 1.04 Å/cycle. The layers took 20 to 45 minutes to grow.

Annealing was carried out at 250°C, 350°C and 600°C using Allwin2 Corp's AccuThermo AW 610 Rapid Thermal Annealing instrument in a nitrogen environment. The chamber temperature was ramped up from room temperature to the desired annealing temperature in 30 seconds. A sample Rapid Thermal Annealing (RTA) recipe and graph for annealing at 250°C is shown in Figure 36.

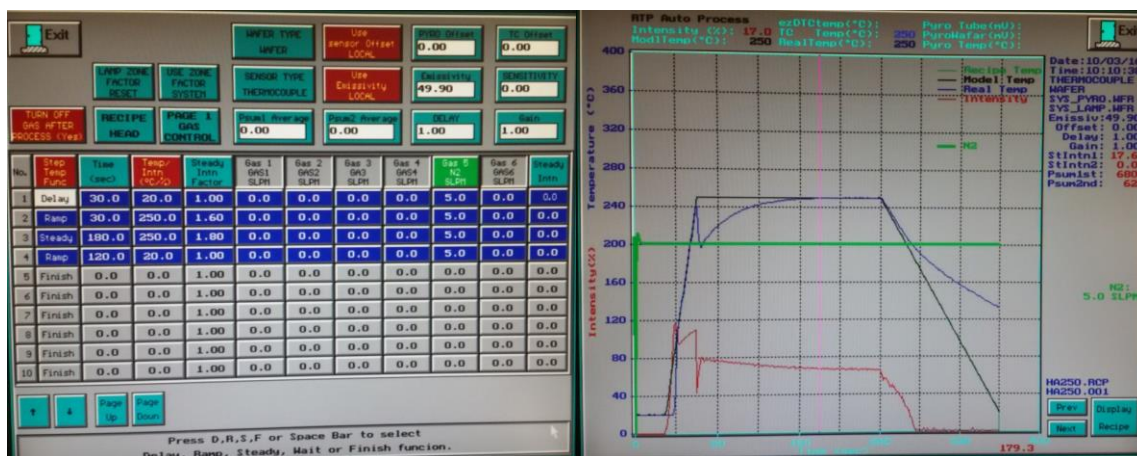


**Figure 36** Recipe and Graph for Annealing at 250°C

## 5. Testing

An accelerated lifetime test is needed to predict slow dissolution rates of ALD coatings in low-temperature water that would otherwise require unacceptable experimental measurement periods of up to years. Using ex situ measurements, it is difficult to investigate thin film dissolution dynamics for real systems that do not experience periodic interruptions in the dissolution process. Electrochemical techniques normally used can't be used in this case since it needs conductive electrodes and doesn't resolve location dependent dissolution. Transmission measurements would be a good fit for this project's requirements. Transmission measurements have the capability to measure location-dependent dissolution dynamics for different metal and ceramic thin films by monitoring nanometer-scale film thickness reductions in-situ. Dissolution rates are derived from normalized transmission changes rather than the absolute transmission itself. A constant error in the measurement will therefore not affect the results. Advantages of Transmission Measurements are that it is non-destructive: unless the sample is photo-sensitive, the measurement can be repeated endlessly without altering the sample; quantitative: more accurate than the human eye for comparing objects or surfaces and local: only the surface of the sample is measured, not its interior.

The most important thing about choosing a light source for transmission measurement is to find one with strong output over the wavelength range of interest. Except in a very few specific cases, a narrow light source will not offer enough useful information, so lasers and most LED's cannot be used. Since the wavelength range of interest for the structures used in this project is between 300 nm to 1000 nm, halogen lamp is used as the light source.

During testing the sample is affixed to a transparent container using optically transparent glue and the area of the sample on which measurements are to be made is marked with permanent marker

before immersion of the sample into PBS, so that the same spot can be monitored over the period of the sample's life time. The optically transparent glue used (Nor land Optical Adhesive 83HA) can be cured by using UV exposure or heat, UV exposure for 5 minutes using UVP Blak-Ray's B-100AP 100W high intensity UV lamp (365 nm) was used in this project. The test can be accelerated by changing the concentration of the PBS solution or by increasing the solution temperature (Arrhenius Equation), increased temperature is used for accelerated testing in this project. One set of samples are tested at the physiological temperature of 37°C (using Affymetrix's GeneChip incubator with the range of Ambient+5°C to 70°C) and another set of samples are tested in a higher accelerated temperature of 85.1°C (using Hybridization Oven 640 110V with the range of ambient to 99.9°C).



**Figure 37** Samples undergoing accelerated aging at higher temperatures in an incubator

There are 3 spectrometers in our lab: Portable (UV to near IR range), UV-Vis, Vis-IR (used for Raman and used as broad-range spectrometer). The grating inside the spectrometer determines the resolution. WITec's UHTS (Ultra-High Throughput Spectrometers) Vis-IR spectrometer was used for transmission tests in this project. 20X immersion lens from Zeiss was used for measurements.

The test set-up is as shown in Figure 38.

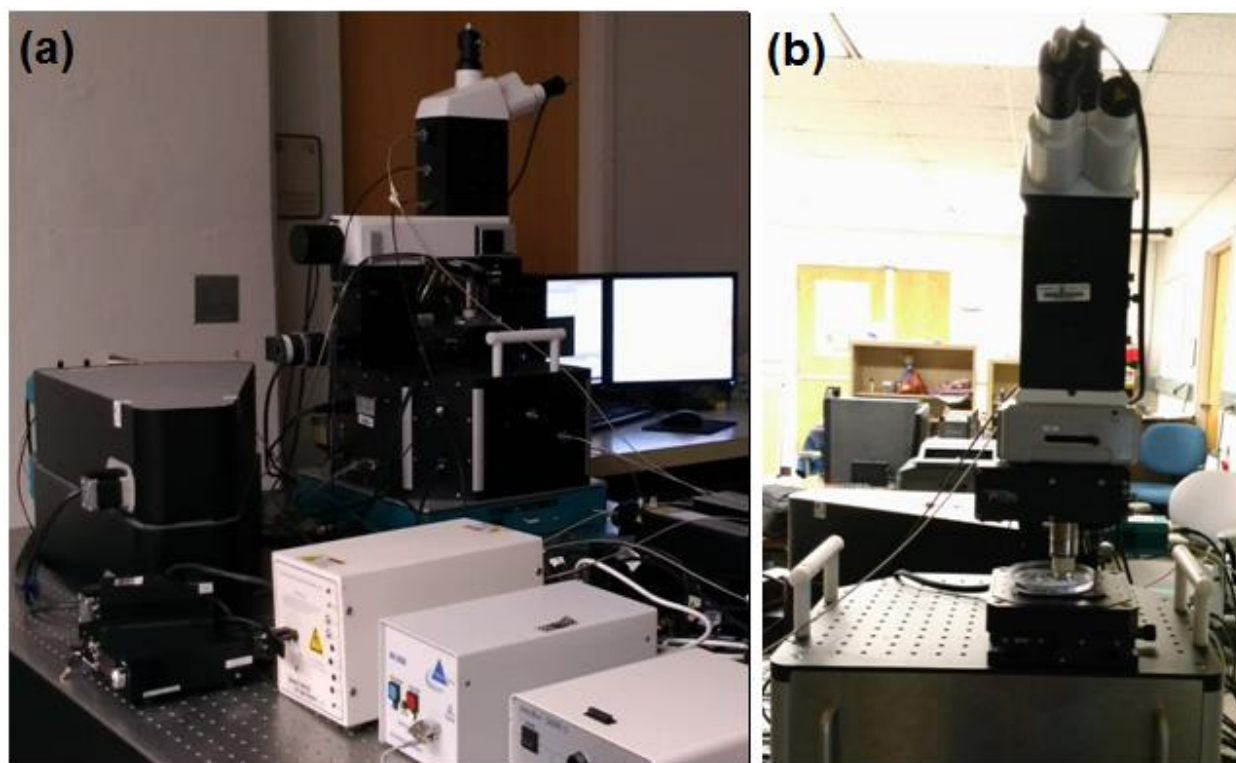


**Figure 38** Test set-up (a) Test set-up showing the light source, microscope and spectrometer.  
(b) Measurement of samples affixed to petri-dish immersion microscope

For the transmission measurements, the integration time, which determines the duration of a single measurement was taken to be 1 s and the number of accumulation, which determines how many times the sample is measured averaged was also set to 1. The transmission measurements were carried out in the wavelength range of 300 nm to 1000 nm. The transmittance of the samples were measured at various intervals of time starting at 0 hours depending on the rate of the reaction for each sample.

The normalized transmittance was calculated using the formula,

$$\text{Normalized Transmission} = \frac{\text{Sample Transmittance} - \text{Dark Current}}{\text{Reference Transmittance} - \text{Dark Current}}$$

Reference transmittance was measured using a plane glass substrate affixed on the petri-dish and was used to normalize the measured transmittance data, eliminating the errors present in the

measurement. Dark current measurement measures the inherent noise present in the spectrometer; it is subtracted from both the sample transmittance and the reference transmittance to compensate for the noise present in the spectrometer in the measurement.

The performance of the protective coating can be monitored using the shift of the FWHM (Full Width Half Maximum), wavelength, transmittance and extinction of the measured transmittance for each sample at different times. The relationship between transmittance and extinction is,  $\text{Extinction} = \text{Absorption} + \text{Scattering} = 1 - \text{Transmittance}$ . Normalized extinction gives the most consistent results, with less noise and variation for the samples in this project. It starts at a maximum value of one and as the sample deteriorates the normalized extinction tends to zero. It can be calculated using the following formula.

$$\text{Normalized Extinction} = \frac{\text{Extinction of day } n}{\text{Extinction of day } 0}$$

## 6. Results and Discussion

### 6.1. Dark Current

Dark current measurement is the measure of the inherent noise of the spectrometer. It is measured during each measurement by making the light intensity 0 and its value is subtracted from the sample and reference transmittance measurements to compensate for the effect of the inherent noise of the spectrometer on the measurement. It is usually measured with a 10 second integration time and its value divided by 10 is subtracted from the reference and sample transmittance measurements. Dark current measurement generally looks like random white noise as shown in Figure 39.

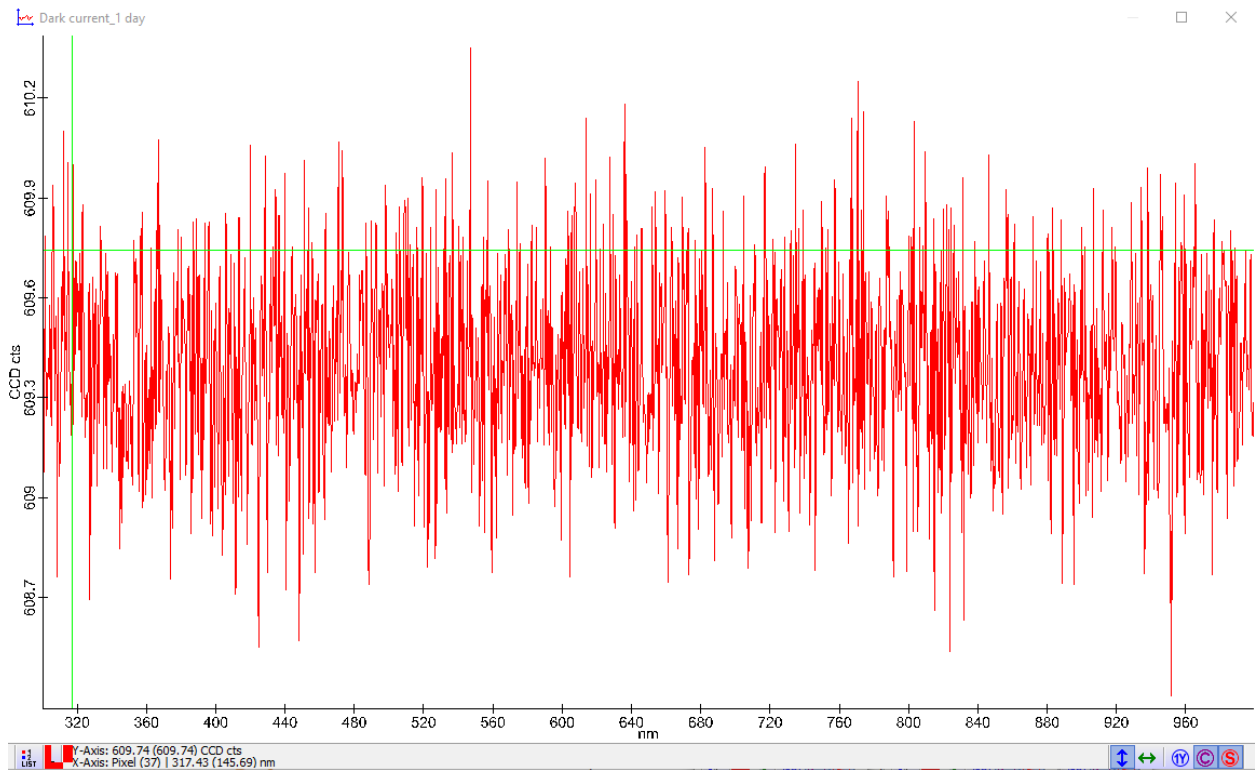


**Figure 39** Sample dark current measurement

## 6.2. Pure Cu 1X PBS Test

Plain copper uncoated by any protective coating was immersed in a 1X PBS solution with a pH of 7.2 at a temperature of 37°C to study its longevity in a corrosive physiological environment. It was monitored using transmission measurements using immersion lens at various time intervals of 0 hr, 2 hr, 3.5 hr, 4 hr, 5 hr and 1 day. The summary of the measured data is presented in Table 10. The graphical representation of the data and its real-time measured signal is given in Figure 40.

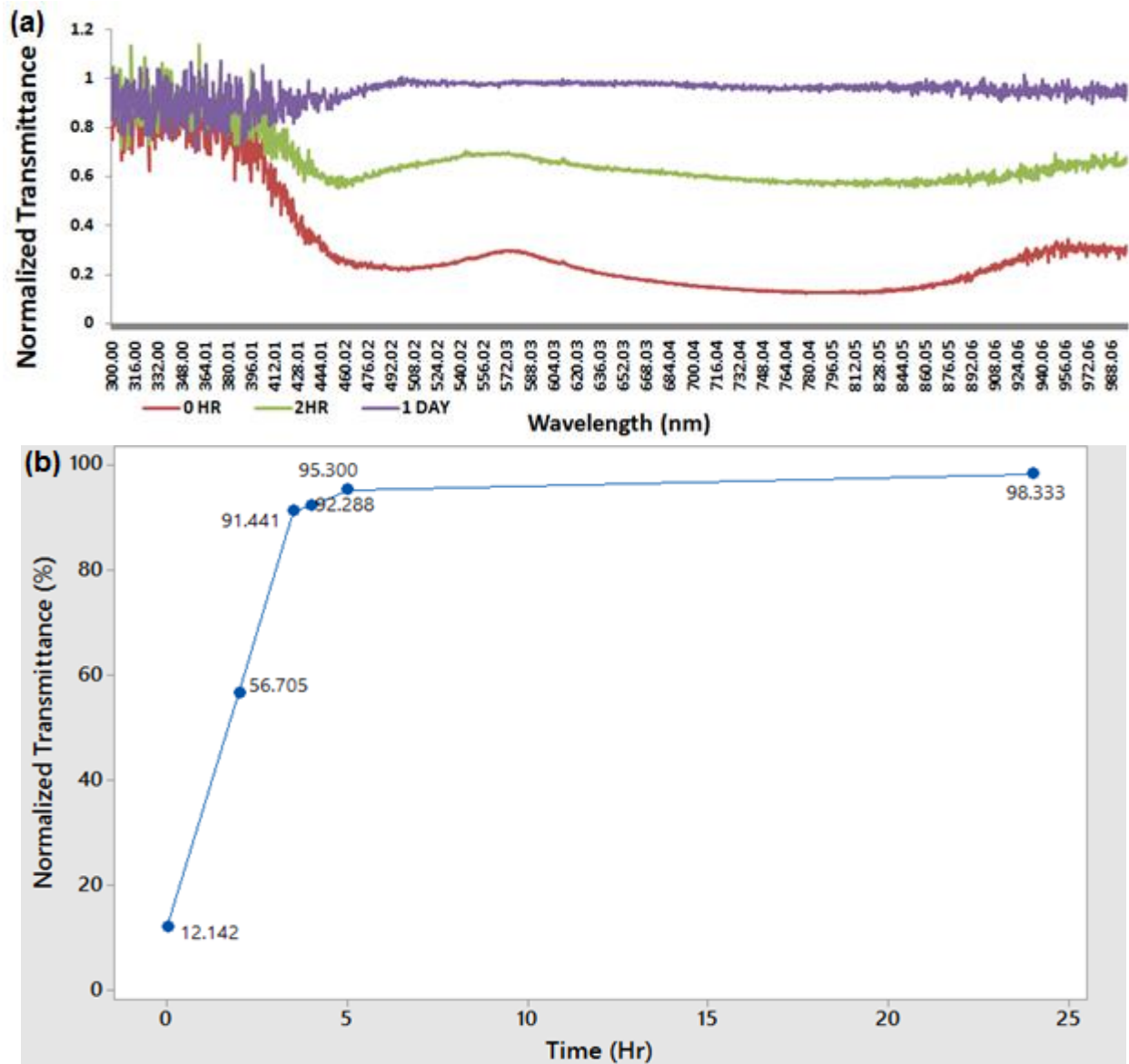


**Figure 40** Copper real-time transmission measurements and graphical summary of the measurement. (a) Real-time Cu transmission measurement at 0 hour, 2 hours and 1 day. (b) Graphical representation of the measured transmission values

Time (Hr)	0	2	3.5	4	5	24
Normalized Transmittance (%)	12.142	56.705	91.441	92.138	95.3	98.333

**Table 10** Cu transmittance measurement data summary

From the measured value of transmittance it can be seen that the 50 nm of Cu deposited having an initial normalized transmittance of only 12.142% deteriorates rapidly in the physiological environment and is almost completely corroded allowing a transmission of greater than 98% within a day. Thus protective coatings are necessary to increase copper plasmonic structure's lifetime in physiological and corrosive environments.

### 6.3. Initial Transmission Measurements

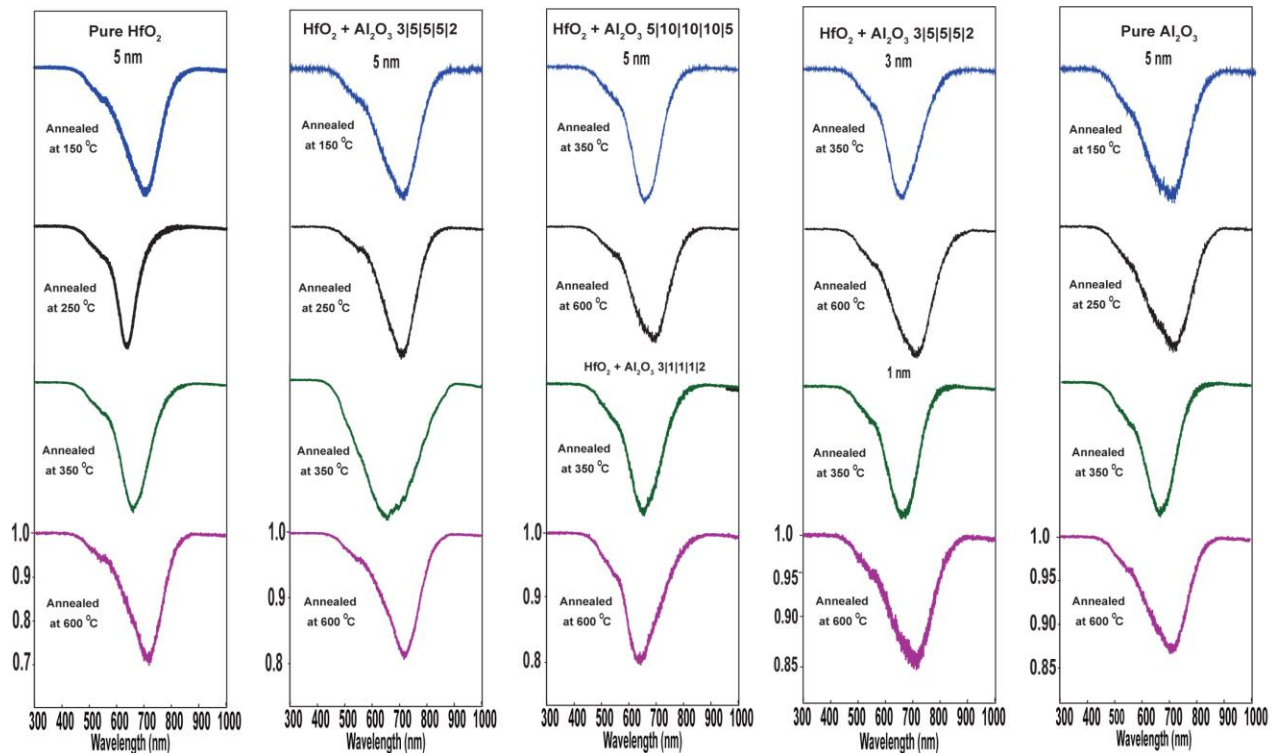


**Figure 41** Initial normalized transmittance of samples

Transmission measurements can be analyzed as a function of normalized wavelength shift, amplitude change, FWHM change or extinction change. After analysis it was found that

normalized extinction gives the most consistent results with lesser noise and variation for the samples in this project. It starts at a maximum value of one and as the sample deteriorates the normalized extinction tends to zero. Transmittance and extinction are related as, Extinction = Absorption + Scattering = 1 – Transmittance. Normalized extinction is calculated using the following formula.

$$\text{Normalized Extinction} = \frac{\text{Extinction of day } n}{\text{Extinction of day } 0}$$

Where extinction of day 0 is the initial extinction of the sample at 0 hours, with respect to which the normalized extinction will be calculated at other time intervals and extinction of day n is the extinction of the sample on day ‘n’.

#### 6.4. Effect of Annealing Temperature

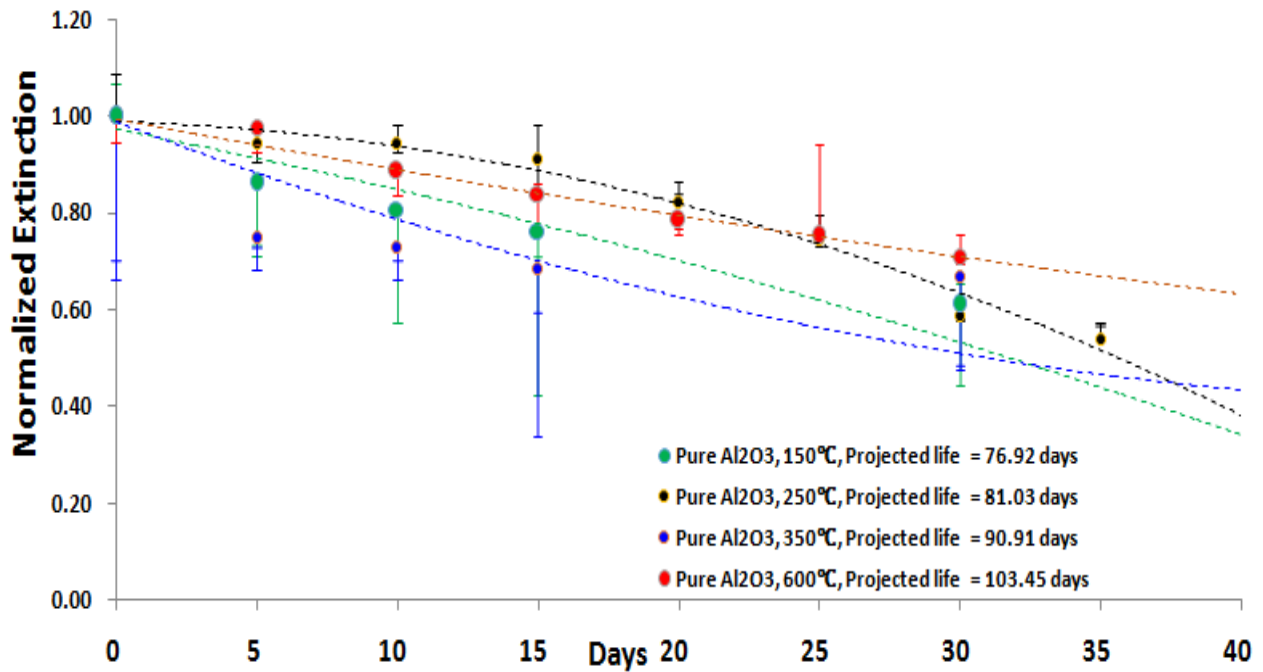


**Figure 42** Normalized extinction of pure Al<sub>2</sub>O<sub>3</sub> annealed at different temperatures in 1X PBS solution at 37°C at various time intervals

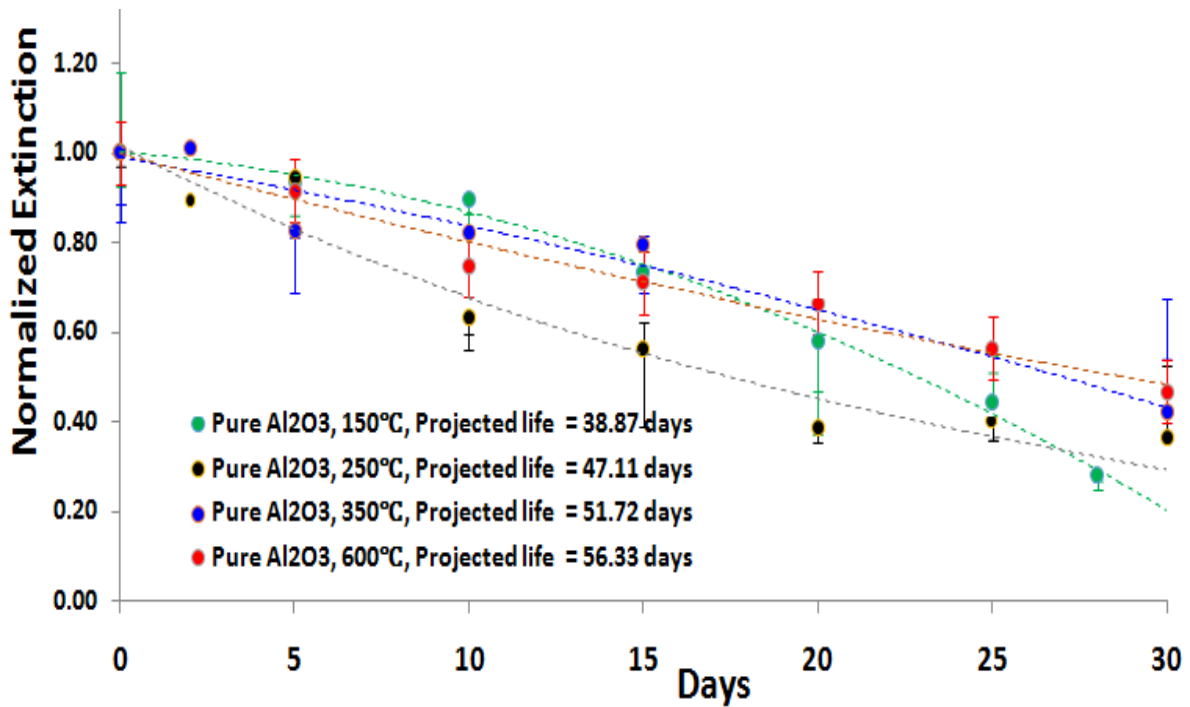


**Figure 43** Normalized extinction of pure Al<sub>2</sub>O<sub>3</sub> annealed at different temperatures in 1X PBS solution at 85.1°C at various time intervals

Comparing the normalized extinction trend of pure Al<sub>2</sub>O<sub>3</sub> samples annealed at 150°C, 250°C, 350°C and 600°C in 1X PBS solution, it can be said that the life-time of pure Al<sub>2</sub>O<sub>3</sub> in corrosive environments increases with increasing annealing temperature. This trend is consistent for both samples tested at the physiological temperature of 37°C (Figure 42) and an elevated temperature of 85.1°C (Figure 43) for accelerated testing. This is due to the structural changes that happen during annealing that expel the trapped gases from the Al<sub>2</sub>O<sub>3</sub> coating leading to lesser voids and a slightly increased density. Al<sub>2</sub>O<sub>3</sub> does not begin to crystallize until above 900°C and is hence essentially amorphous for all the tested conditions. As expected the life-time of the sample is lesser in the accelerated test temperature of 85.1°C than the physiological temperature of 37°C. Polynomial fitting was used to fit the data and calculate the projected life-time of the samples.

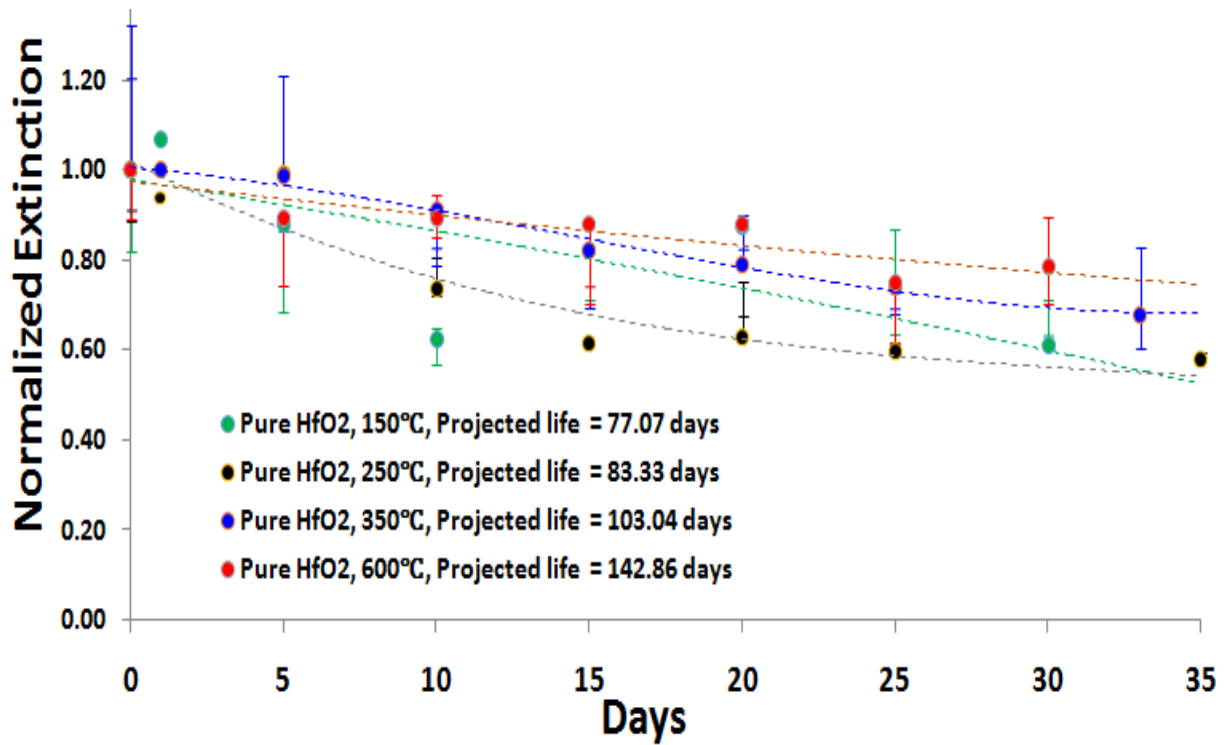


**Figure 44** Normalized extinction of pure HfO<sub>2</sub> annealed at different temperatures in 1X PBS solution at 37°C at various time intervals

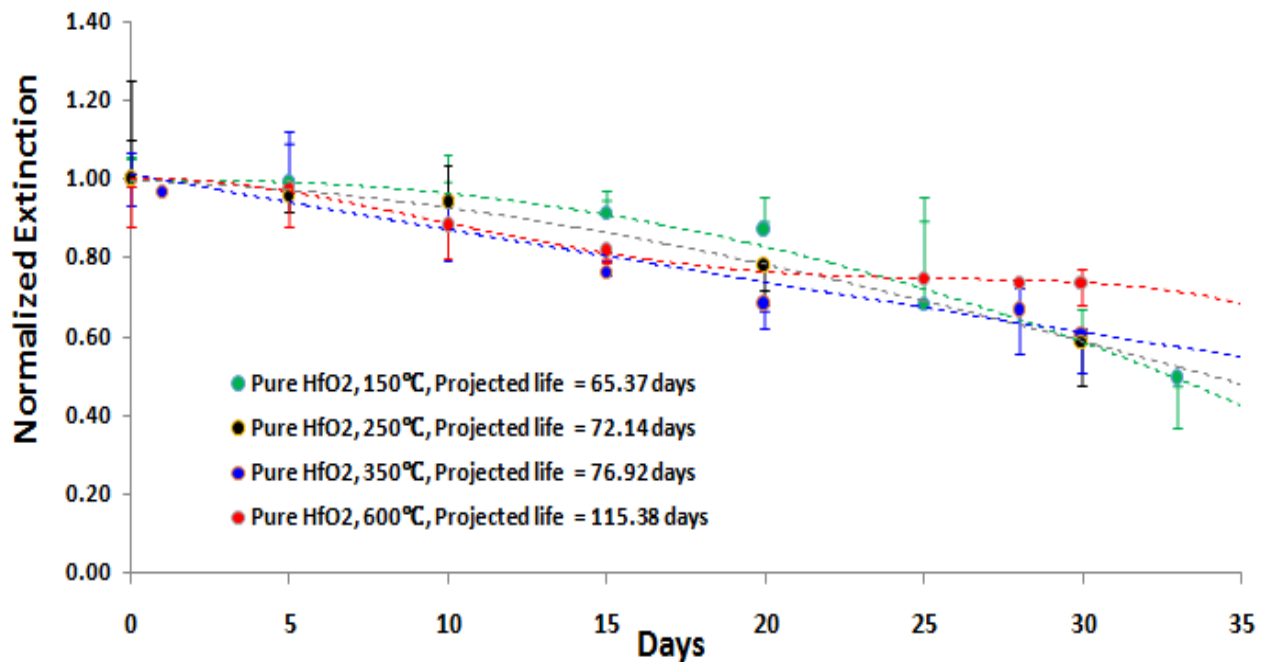


**Figure 45** Normalized extinction of pure HfO<sub>2</sub> annealed at different temperatures in 1X PBS solution at 85.1°C at various time intervals

Comparing the normalized extinction trend of pure HfO<sub>2</sub> samples annealed at 150°C, 250°C, 350°C and 600°C in 1X PBS solution, it can be said that the life-time of pure HfO<sub>2</sub> in corrosive environments increases with increasing annealing temperature. This trend is consistent for both samples tested at the physiological temperature of 37°C (Figure 44) and an elevated temperature of 85.1°C (Figure 45) for accelerated testing. At an annealing temperature of 250°C it is predominantly due to expulsion of trapped gases from the HfO<sub>2</sub> coating due to annealing leading to lesser voids and a slightly increased density. Above 350°C annealing it is due to the onset of crystallization with its associated structural changes that expel the trapped gases from the HfO<sub>2</sub> coating leading to lesser voids and the consequent change into a phase with increased structural density. HfO<sub>2</sub> begins to crystallize at 350°C and is completely crystalline at the annealing temperature of 600°C. As expected the life-time of the sample is lesser in the accelerated test temperature of 85.1°C than the physiological temperature of 37°C. Polynomial fitting was used to fit the data and calculate the projected life-time of the samples.

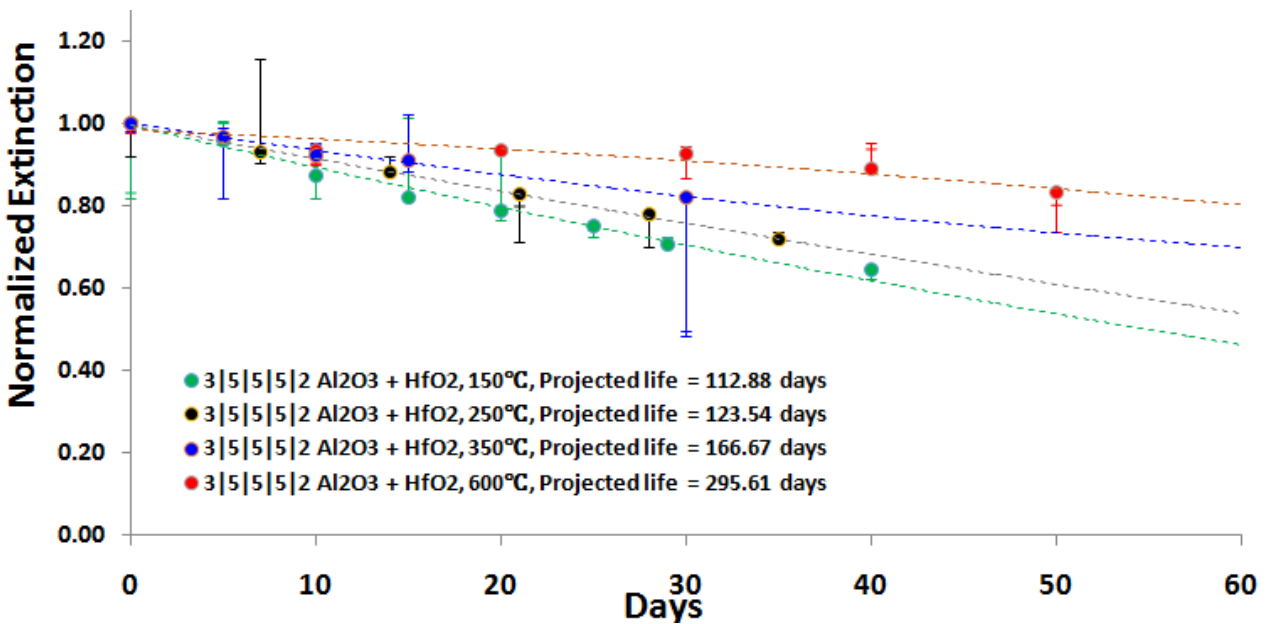


**Figure 46** Normalized extinction of Al<sub>2</sub>O<sub>3</sub> and HfO<sub>2</sub> nanolaminate structure in 3|5|5|5|2 ratio annealed at different temperatures in 1X PBS solution at 37°C at various time intervals

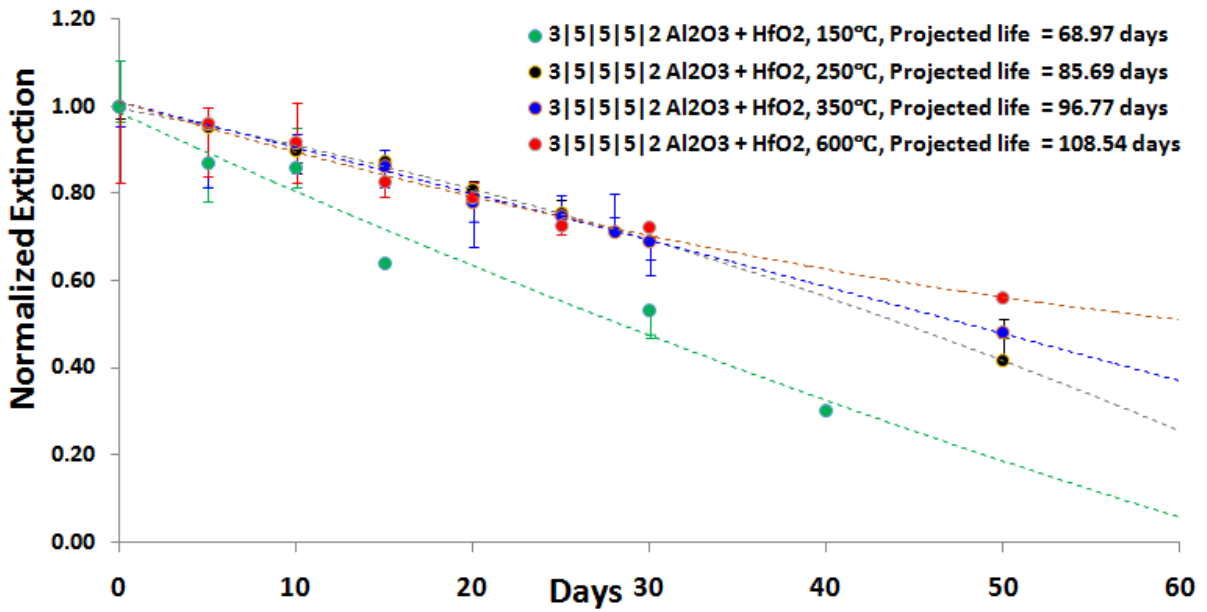


**Figure 47** Normalized extinction of Al<sub>2</sub>O<sub>3</sub> and HfO<sub>2</sub> nanolaminate structure in 3|5|5|5|2 ratio annealed at different temperatures in 1X PBS solution at 85.1°C at various time intervals

Comparing the normalized extinction trend of samples containing a mixture of Al<sub>2</sub>O<sub>3</sub> and HfO<sub>2</sub> in the form of 3|5|5|5|2 annealed at 150°C, 250°C, 350°C and 600°C in 1X PBS solution, it can be said that the life-time of the samples in corrosive environments increases with increasing annealing temperature. This trend is consistent for both samples tested at the physiological temperature of 37°C (Figure 46) and an elevated temperature of 85.1°C (Figure 47) for accelerated testing. This is due to the structural changes that happen during annealing that expel the trapped gases from the coating leading to lesser voids and an increased coating density. Al<sub>2</sub>O<sub>3</sub> does not begin to crystallize until above 900°C and is hence essentially amorphous for all the tested conditions, while HfO<sub>2</sub> in the mixture would tend to start crystallizing at 350°C in its pure form, but its crystallization is also suppressed by the Al<sub>2</sub>O<sub>3</sub> present in the nanolaminate structure. As expected the life-time of the sample is lesser in the accelerated test temperature of 85.1°C than the physiological temperature of 37°C. Polynomial fitting was used to fit the data and calculate the projected life-time of the samples.

## 6.5. Effect of Sample Composition

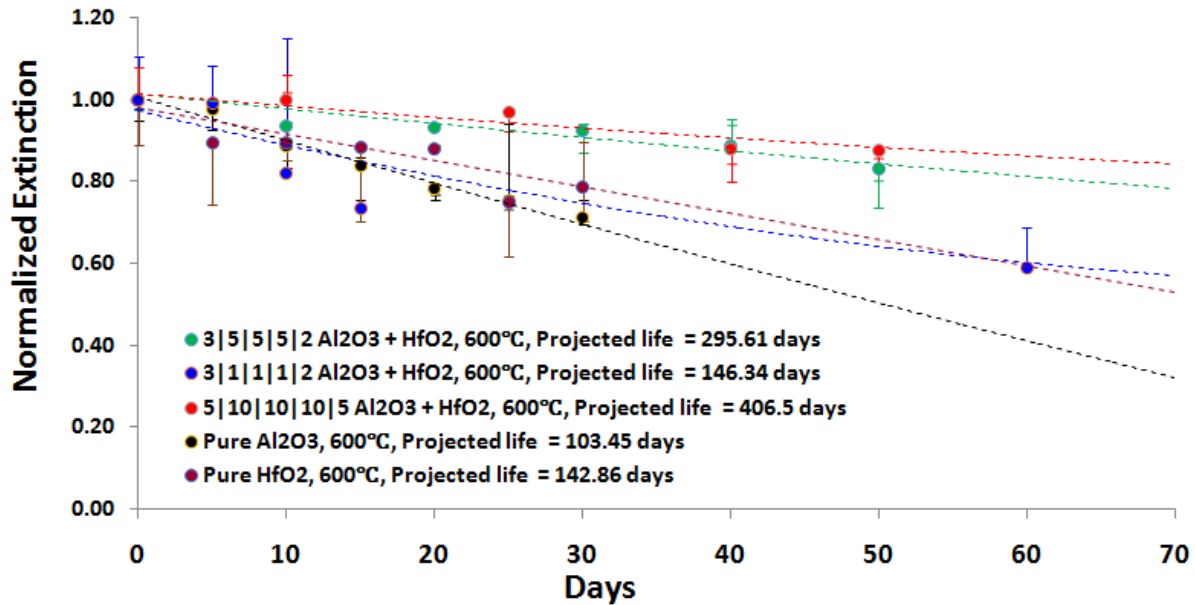


Figure 48 Normalized extinction of different sample compositions annealed at 600°C in 1X PBS solution at 37°C at various time intervals

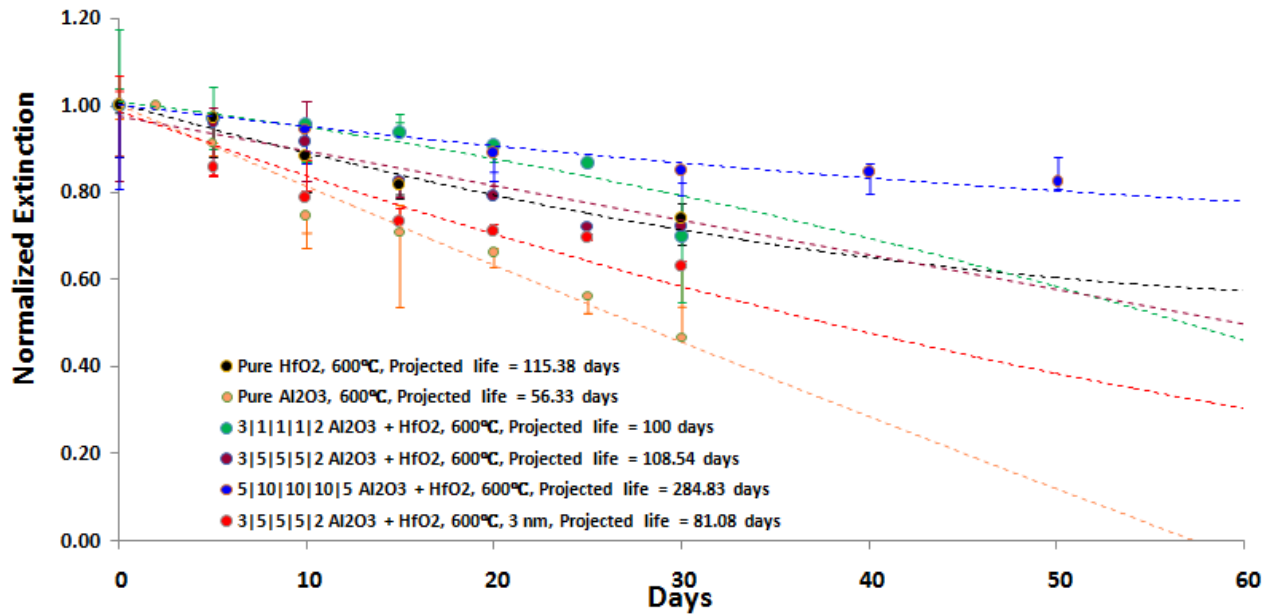


Figure 49 Normalized extinction of different sample compositions annealed at 600°C in 1X PBS solution at 85.1°C at various time intervals

From the transmission measurements and normalized extinction calculation of coating performance of pure HfO<sub>2</sub>, pure Al<sub>2</sub>O<sub>3</sub>, nanolaminate structures containing both Al<sub>2</sub>O<sub>3</sub> and HfO<sub>2</sub>

in the different proportions like 3|1|1|1|2, 3|5|5|5|2, 5|10|10|10|5 annealed at 600°C and 350°C immersed in 1X PBS solution at physiological temperature of 37°C and the accelerated test temperature of 85.1°C it is observed that the nanolaminate structure containing Al<sub>2</sub>O<sub>3</sub> and HfO<sub>2</sub> in the proportion of 5|10|10|10|5 gives best protection against permeation of water and ions and hence provides the best protection for the plasmonic structure underneath. Pure aluminum oxide is most permeable, because of the voids present in it due to ALD growth. The protection afforded by pure Hafnium Oxide and the nanolaminate structure containing Al<sub>2</sub>O<sub>3</sub> and HfO<sub>2</sub> in the proportion of 3|1|1|1|2 are comparable to each other and are better than the protective properties of pure Al<sub>2</sub>O<sub>3</sub>. Pure Hafnium Oxide is less permeable to water and ions than Aluminum Oxide because of its higher density and lesser voids due to crystallization. The 3|1|1|1|2 nanolaminate structure has extremely thin layers of Al<sub>2</sub>O<sub>3</sub> and HfO<sub>2</sub> inter-woven with each other and hence even pinholes would allow contact between multiple layers of Al<sub>2</sub>O<sub>3</sub> with Al<sub>2</sub>O<sub>3</sub> and HfO<sub>2</sub> with HfO<sub>2</sub>, and hence the formation of extended voids in Al<sub>2</sub>O<sub>3</sub> layers and crystallization of HfO<sub>2</sub> can only be partially suppressed, giving rise to somewhat better protection, but not the best protection. The nanolaminate structure containing Al<sub>2</sub>O<sub>3</sub> and HfO<sub>2</sub> sandwiched in the form of 3|5|5|5|2 gives better protection than pure HfO<sub>2</sub> and the 3|1|1|1|2 nanolaminate structure, but is inferior to the protection provided by 5|10|10|10|5 nanolaminate structure. The 5|10|10|10|5 nanolaminate structure effectively prevents the contact between different layers of Al<sub>2</sub>O<sub>3</sub> and HfO<sub>2</sub> in the protective coating and hence effectively suppresses the formation of extended voids in the Al<sub>2</sub>O<sub>3</sub> and effectively prevents the crystallization of HfO<sub>2</sub> with long crystal boundaries (were water and ion can permeate through and affect the plasmonic structure beneath) and hence it provides the best protection. This trend is consistent for both samples tested at the physiological temperature of 37°C (Figure 48 and Figure 50) and an elevated temperature of 85.1°C (Figure 51 and Figure 49) for accelerated testing. The life-time of the sample is lesser in the accelerated test temperature of

85.1°C than the physiological temperature of 37°C. Polynomial fitting was used to fit the data and calculate the projected life-time of the samples.

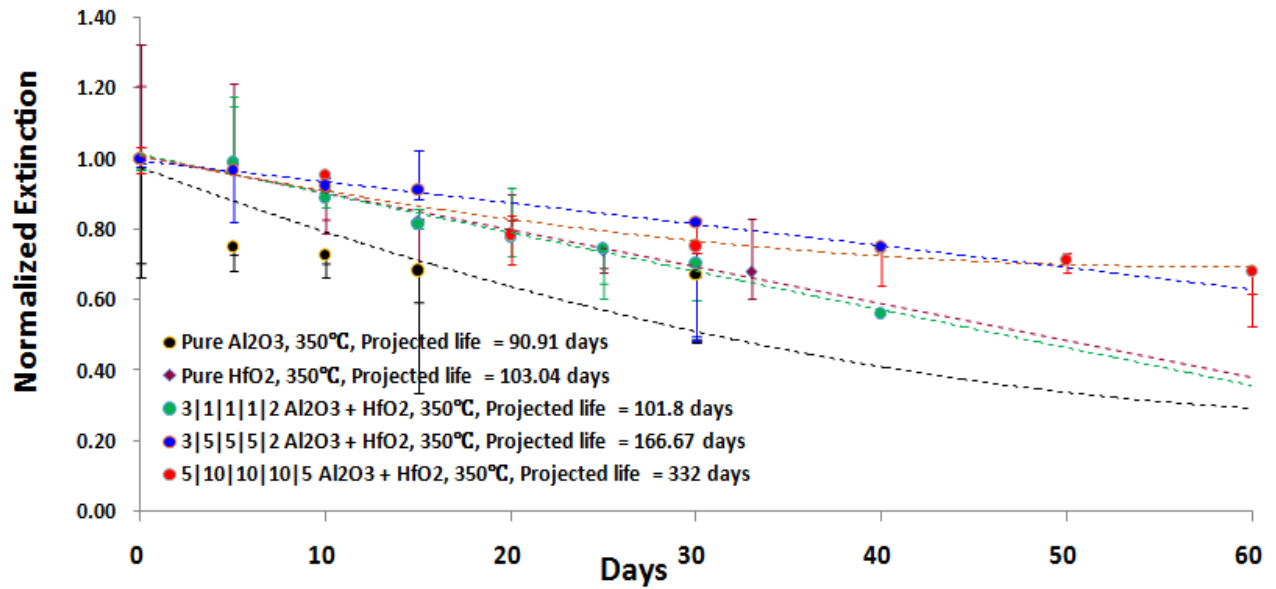


Figure 50 Normalized extinction of different sample compositions annealed at 350°C in 1X PBS solution at 37°C at various time intervals

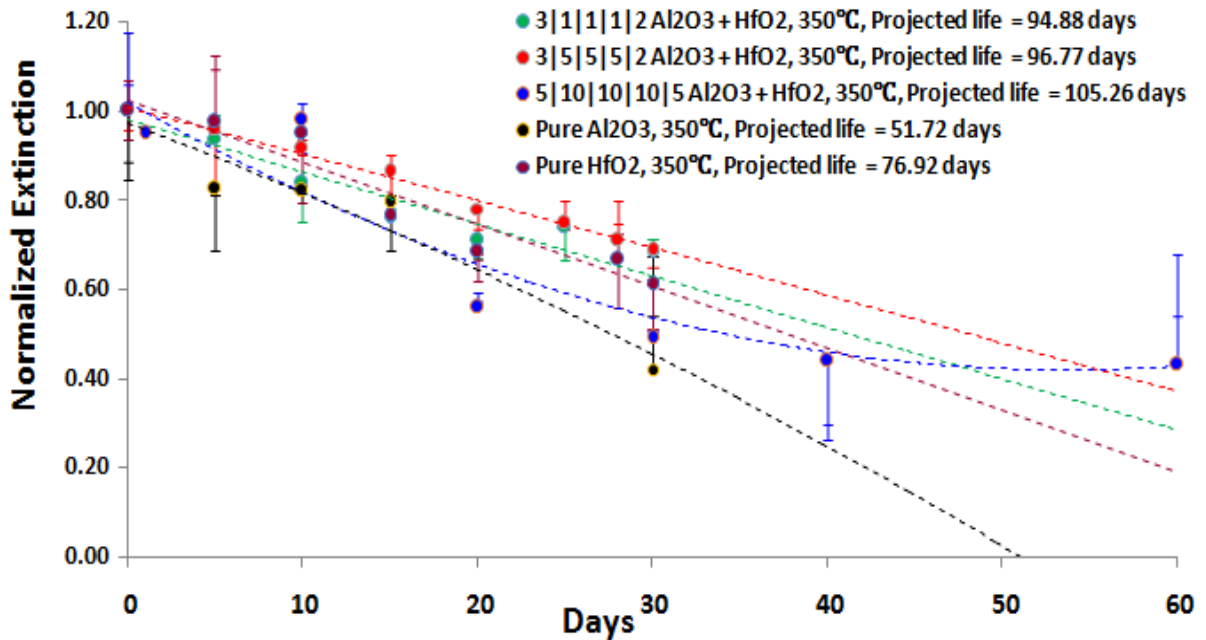
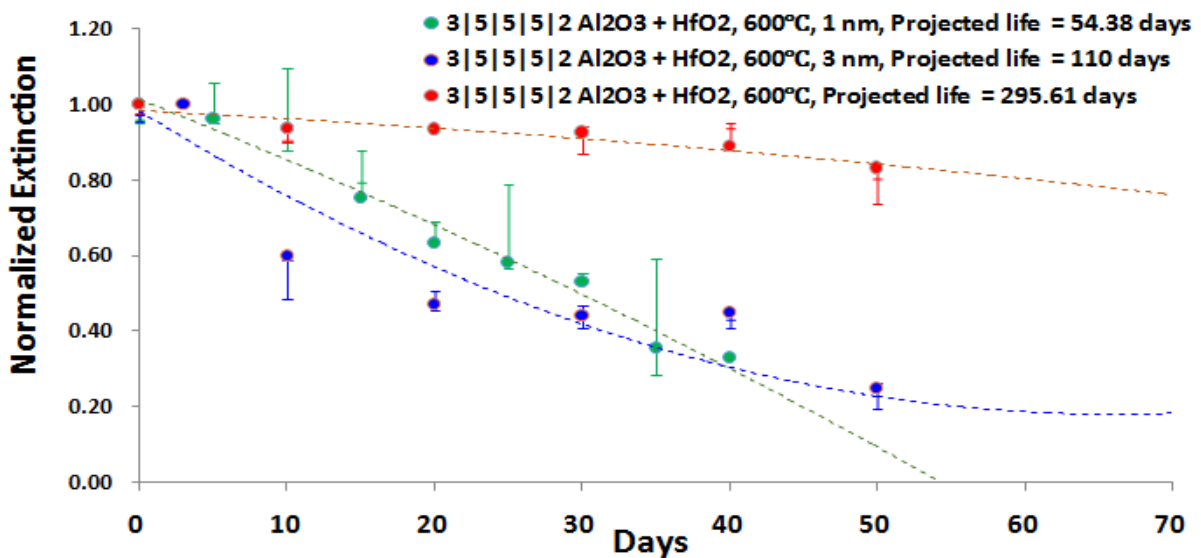


Figure 51 Normalized extinction of different sample compositions annealed at 350°C in 1X PBS solution at 85.1°C at various time intervals

## 6.6. Effect of Coating Thickness

Comparing the protective properties of 1 nm, 3nm and 5nm thick 3|5|5|5|2 nanolaminate protective coating annealed at 600°C and 350°C in 1X PBS solution at the physiological temperature of 37°C and the elevated temperature of 85.1°C it can be concluded that 5 nm coating provides better protection than 3 nm coating, which in turn provides much better protection than the 1 nm coating. 1 nm coating does not provide very good protection against diffusion of water and ions damaging the plasmonic structure because even pin-holes in a few layers of the coating are enough for a portion of the sample to become unprotected. Thicker coatings in addition to being less affected by pin-holes have more layers to be etched away by the water and ion, before allowing them to affect the plasmonic structure underneath and the water and ions have to permeate more layers to reach the plasmonic structure. It is also interesting to note that (from Figure 49) that only 3 nm of the 3|5|5|5|2 nanolaminate structure gives much better protection against diffusion of ions and water and gives better protection than 5 nm protective coating of pure Al<sub>2</sub>O<sub>3</sub>. Polynomial fitting was used to fit the data and calculate the projected life-time of the samples.



**Figure 52** Normalized extinction of samples of different thicknesses with Al<sub>2</sub>O<sub>3</sub> and HfO<sub>2</sub> in 3|5|5|5|2 ratio annealed at 600°C in 1X PBS solution at 37°C at various time intervals

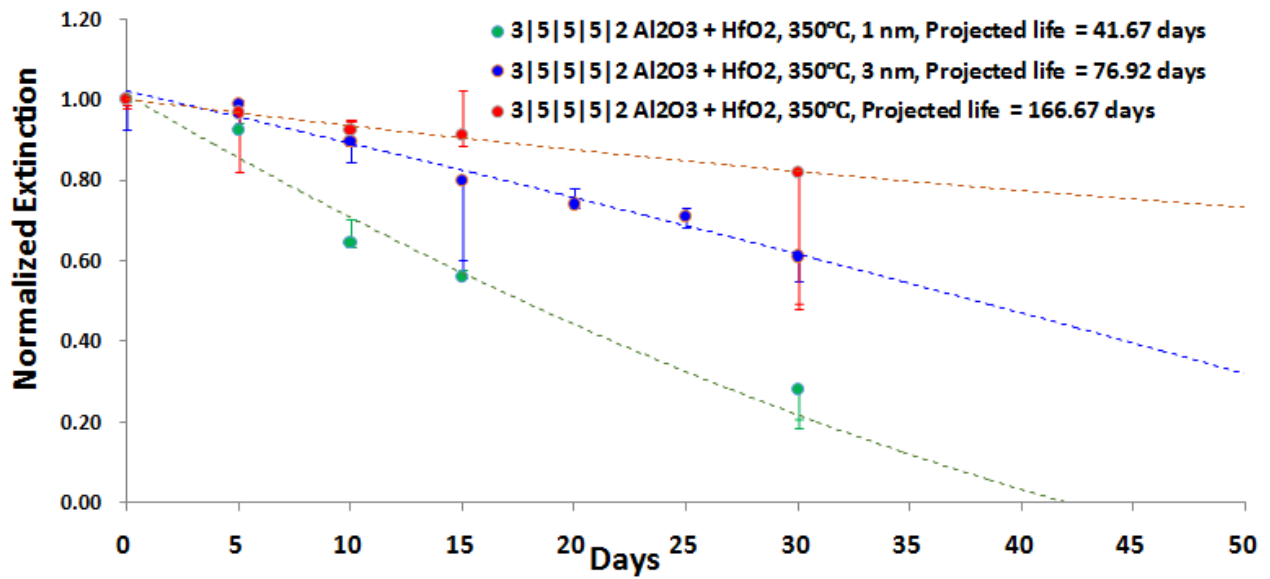


**Figure 53** Normalized extinction of samples of different thicknesses with Al<sub>2</sub>O<sub>3</sub> and HfO<sub>2</sub> in 3|5|5|5|2 ratio annealed at 350°C in 1X PBS solution at 37°C at various time intervals

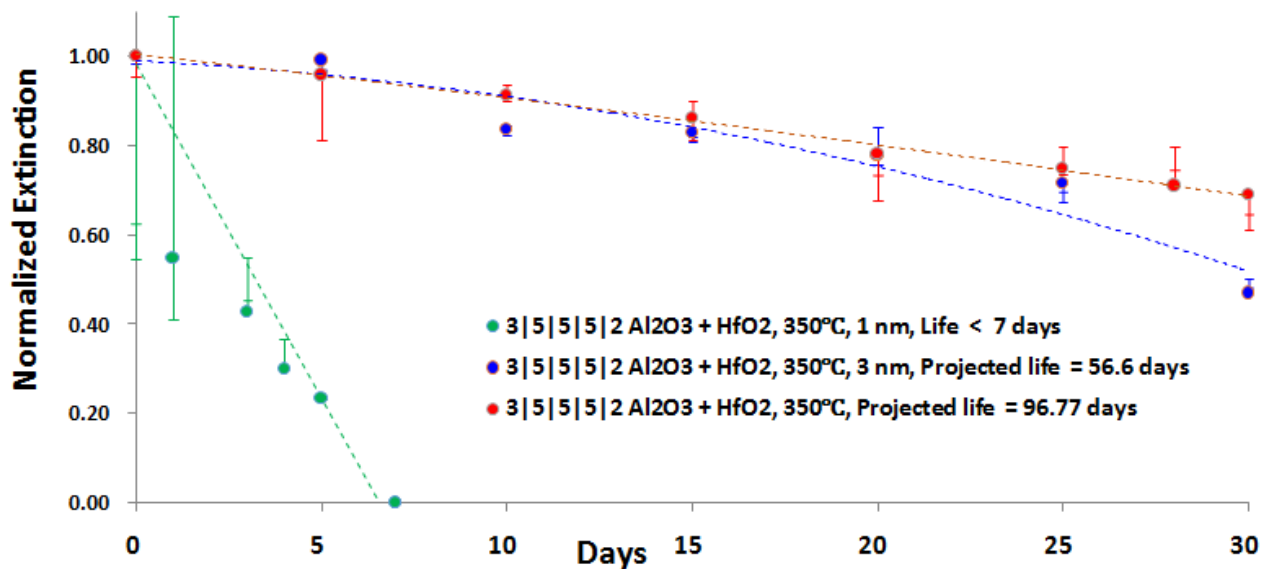


**Figure 54** Normalized extinction of samples of different thicknesses with Al<sub>2</sub>O<sub>3</sub> and HfO<sub>2</sub> in 3|5|5|5|2 ratio annealed at 350°C in 1X PBS solution at 85.1°C at various time intervals

General Note: The dotted line is used just as a visual guide. All fittings were done using polynomial fit. The lines resembling error bars indicate the corresponding values of the other measurements for the sample taken on the same day normalized with respect to the selected 0 hour measurement. Some data points have all the measured data close to each other and hence the error bars overlap with the data point and are not visible.

## 7. Conclusion

Pure Copper deteriorates at a rapid rate in the pH, ionic and temperature conditions of the physiological environment. It was found that 50 nm of Copper deteriorates within a day when it is subject to physiological conditions by immersing them in 1X PBS solution at 37°C. This limits their usage in plasmonic applications. The plasmonic properties are sensitive to the dimension changes of the plasmonic nano-structure and hence any protective coating on them should be kept as thin as possible. In this project nano-scale Periodic Particle Array (PPA) of Copper plasmonic nano-structures were fabricated using e-beam deposition process, fabrication using Nano-Sphere Lithography (NSL) and Hole-mask Colloidal Lithography (HCL) were also explored. Thin-film characterizations of the protective coatings were done using ellipsometry. 5 nm, 3 nm and 1 nm, Al<sub>2</sub>O<sub>3</sub> and HfO<sub>2</sub> dielectric protective coatings and their nano-laminate combinations were deposited using ALD. The stability of these coatings was tested in-situ by immersing them in a 1X PBS solution at 37°C and 85.1°C and monitoring the transmittance (extinction) of the samples at different time intervals. From the tests it was found that the performance of the protective coating increases with annealing temperature and increases with increasing thickness of the coating. The protective properties of the 5|10|10|10|5 Al<sub>2</sub>O<sub>3</sub> and HfO<sub>2</sub> nano-laminate coatings were better than the protective properties of 3|5|5|5|2 Al<sub>2</sub>O<sub>3</sub> and HfO<sub>2</sub> nano-laminate coatings, which was better than the protective properties of 3|1|1|1|2 Al<sub>2</sub>O<sub>3</sub> and HfO<sub>2</sub> multilayer coatings. The protective properties of 3|1|1|1|2 Al<sub>2</sub>O<sub>3</sub> and HfO<sub>2</sub> nano-laminate coatings were comparable to the protective properties of pure HfO<sub>2</sub> coatings. Pure Al<sub>2</sub>O<sub>3</sub> provided the least protection against permeation of water and ions. 5|10|10|10|5 Al<sub>2</sub>O<sub>3</sub> and HfO<sub>2</sub> nano-laminate coatings annealed at 600°C provided the best barrier against the diffusion of ions and water and has a projected life-time of more than a year (~ 407 days) in 1X PBS solution at the physiological temperature of 37°C. This is due to the effective suppression of voids in the Al<sub>2</sub>O<sub>3</sub> layers by the HfO<sub>2</sub> layers in the multilayer structure,

the prevention of onset of crystallization of  $\text{HfO}_2$  with crystal boundaries through which ions and water can diffuse through the protective coating and affect the Copper underneath, by the  $\text{Al}_2\text{O}_3$  layers in the nano-laminate structure and the formation of a dense  $(\text{Hf})\text{Al}_x\text{O}_y$ -aluminate phase at the interfaces which suppresses ion and water permeation through the barrier stack.

This work is important in that it explores the effectiveness and protective properties of extremely thin nanolaminate coatings on Copper plasmonic structures. It can easily be extended to other plasmonic structures made of Gold, Silver, Aluminum, etc. because the materials used for the coatings can be deposited by ALD which can also be used with the plasmonic structures made of other materials. The dielectric coatings used and the processes are CMOS compatible and scalable to have more sensors on a single device. This also has the advantage of less fabrication cost since the sensing and electronic parts can be integrated, the resulting smaller package size also has lesser resistive losses, RC time delay and less noise coupling. The materials of the coatings are also bio-compatible. Since the protective coatings are deposited at a relatively lower temperature of  $150^\circ\text{C}$ , they can be used with flexible PET polymer substrates as well (which could be important for implantable biological applications), and the lower temperature also ensures lower diffusion of impurities during processing. Since in-situ testing was used in this project, real-time uninterrupted physiological condition testing was carried out. This project can be used to enhance the life-time of the plasmonic structures used in biological sensing applications, lab-on-chip applications (chemical and biological sensing, pH measurements, real time binding kinetic studies), plasmonic solar cells, implantable plasmonic sensors (glucose level sensing, body pH sensing, sensing proteins like streptavidin), etc.

## 8. Future Work

The Al<sub>2</sub>O<sub>3</sub> and HfO<sub>2</sub> dielectric protective coatings used in this project on Copper plasmonic nanostructures are deposited using ALD and hence can be used as low temperature coating on other plasmonic structures like Gold, Silver, Aluminum and other structures made from novel materials like 2D-Chalcogenide crystals (used in optoelectronics applications), perovskite (used in photo-cell applications) etc. to enhance their long term stability in physiological environments. These other plasmonic structures can be made and the protective coating's efficiency on them in physiological environments can be tested. Right now testing is done in a PBS environment which simulates the physiological environment. Real-time testing in an actual physiological environment can also be done. The protective coating's performance in a real physiological environment has to be tested before using it in an actual implantable Plasmonics based sensor device. More coating compositions (like a nano-laminate protective coating of Al<sub>2</sub>O<sub>3</sub> and HfO<sub>2</sub> in the ratio of 5|15|15|15|5) can also be explored based on the trends obtained in this project to find the coating composition, thickness and annealing temperature combination that gives the best coating performance for the same overall thickness of the protective coating. Coatings using ZrO<sub>2</sub> instead of HfO<sub>2</sub> can also be studied, as ZrO<sub>2</sub> is known to be more stable than HfO<sub>2</sub> in ionic solutions.

The activation energy of water dissolution of Al<sub>2</sub>O<sub>3</sub> and HfO<sub>2</sub> were found to be 62 kJ/mole and 27 kJ/mole respectively from literature [22] [37]. Using these values in the Arrhenius equation ( $k=Ae^{-E/RT}$ , Where k=Rate Constant, A=Frequency factor, E= Activation energy, R=Gas Constant, T=Temperature in Kelvin), the rate constant for Al<sub>2</sub>O<sub>3</sub> at 85.1°C was found to be 25 times than that at 37°C. The rate constant for HfO<sub>2</sub> was calculated to be around 4 times than that at 37°C at 85.1°C. The activation energy of the nanolaminate structure should be lesser than that of HfO<sub>2</sub>, but its accurate value could be determined by monitoring the change of thickness of a film in physiological environment periodically using ellipsometry measurements. These values will

enable the prediction of the relationship between the temperature of the solution and the rate of the accelerated testing more accurately. Alternately 10 times accelerated endurance testing of the protective coatings can be done with 10X PBS solution with a pH value of 7.4. Quantitative study of the film stability was performed in this project. Qualitative study to know the dissolution process can be performed by using Density Function Theory (DFT) simulation and molecular dynamics study. In-situ real time measurements at the interface can also be obtained using Raman spectroscopic measurements.

## References

1. Bohren, C. F.; Huffman, D. R. Absorption and Scattering of Light by Small Particles; John Wiley & Sons: New York, 1983
2. Zeman, E. J.; Schatz, G. C., “An accurate electromagnetic theory study of surface enhancement factors for silver, gold, copper, lithium, sodium, aluminum, gallium, indium, zinc, and cadmium”, *J. Phys. Chem.* 1987, 91, 634-643
3. Chan, et al., “Plasmonic Properties of Copper Nanoparticles Fabricated by Nanosphere Lithography”, *Nano Lett.*, Vol. 7, No. 7, 2007
4. Matthew Rycenga, et al., “Controlling the Synthesis and Assembly of Silver Nanostructures for Plasmonic Applications”, *Chemical Reviews* 2011, 111, 3669–3712
5. Rich, et al., “Survey of the year 2003 commercial optical biosensor literature”, *Journal of Molecular Recognition*, 2005; 18: 1–39
6. Andrey A. Vyshnevyy, et al, Spontaneous Emission and Fundamental Limitations on the Signal-to-Noise Ratio in Deep-Subwavelength Plasmonic Waveguide Structures with Gain, *Physical Review Applied* (2016)
7. Rashid Zia, et al., “Plasmonics: the next chip-scale technology”, *Materials Today*, July-August 2006, Volume 9, Number 7-8
8. D.J. Bergman, M.I. Stockman, “Surface Plasmon Amplification by Stimulated Emission of Radiation: Quantum Generation of Coherent Surface Plasmons in Nanosystems”, *Phys. Rev. Lett.* 90 (2003), 027402
9. J. Seidel, et al., “Stimulated Emission of Surface Plasmons at the Interface between a Silver Film and an Optically Pumped Dye Solution”, *Phys. Rev. Lett.* 94 (2005) 177401
10. Luo, et al., “Surface plasmon resonant interference nanolithography technique”, *Applied Physics Letters*, Vol. 84, No. 23, 7 June 2004

11. Ramaccia, et al., "Core-shell super-spherical nanoparticles for LSPR-based sensing platforms", *IEEE Journal of Selected Topics in Quantum Electronics*, Vol. 23, No. 2, March/April 2017
12. Joachim Fritzsche et al., *Nano Letters* 2016, 16, 7857–7864
13. Wen-Jeng Ho, et al., "Performance-Enhanced Textured Silicon Solar Cells Based on Plasmonic Light Scattering Using Silver and Indium Nanoparticles", *Materials* 2015, 8(10), 6668-6676
14. T. Ishi, et al., "Reverse design of a bull's eye structure based on the plasmonic far-field pattern", *Journal of Applied Physics*, 44 (2005) L364–L366
15. Yersak, et al., "Characterization of Thin Film Dissolution in Water with in Situ Monitoring of Film Thickness Using Reflectometry", *ACS Applied Materials & Interfaces*, 2016, 8, 17622–17630
16. Jeon, et al., "Atomistic insights into aqueous corrosion of copper", *The Journal of chemical physics* 2011, 134
17. Pehkonen, et al., "Effect of Specific Water Quality Parameters on Copper Corrosion", *Corrosion* 2002, 58, 156
18. Sobue, et al., "Effect of Free Carbon Dioxide on Corrosion Behavior of Copper in Simulated Water", *Surf. Coat. Technol.* 2003, 169, 662
19. Feng, et al., "Corrosion mechanisms and products of copper in aqueous solutions at various pH values", *Corrosion* 1997, 53, 389
20. Boulay, et al., "Role of temperature, chlorine, and organic matter in copper corrosion by-product release in soft water", *Water Res.* 2001, 35, 683
21. Kim, et al., "Influence of particle oxide coating on light scattering by submicron metal particles on silicon wafers", *Appl. Phys. Lett.* 2004, 84, 1278-1280
22. Hoffmann, et al., "Gas Diffusion Barriers Prepared by Spatial Atmospheric Pressure Plasma Enhanced ALD", *ACS Appl. Mater. Interfaces* 2017, 9, 4171–4176

23. Abdulagatov, et al., “Al<sub>2</sub>O<sub>3</sub> and TiO<sub>2</sub> Atomic Layer Deposition on Copper for Water Corrosion Resistance”, *ACS Appl. Mater. Interfaces* 2011, 3, 4593–4601
24. Zhou, et al., “Long Term Stability of Nanowire Nanoelectronics in Physiological Environments”, *Nano Lett.* 2014, 14, 1614–1619
25. Carcia, et al., “Nanosphere Lithography: Permeability and corrosion in ZrO<sub>2</sub>/Al<sub>2</sub>O<sub>3</sub> nanolaminate and Al<sub>2</sub>O<sub>3</sub> thin films grown by atomic layer deposition on polymers”, *Journal of Vacuum Science & Technology A* 30, 041515 (2012), doi: 10.1116/1.4729447
26. Meyer, et al., Nanosphere Lithography: “Al<sub>2</sub>O<sub>3</sub>/ZrO<sub>2</sub> Nanolaminates as Ultrahigh Gas-Diffusion Barriers—A Strategy for Reliable Encapsulation of Organic Electronics”, *Adv. Mater.* 2009, 21, 1845–1849
27. Wan, et al., “Improved Corrosion Resistance and Mechanical Properties of CrN Hard Coatings with an Atomic Layer Deposited Al<sub>2</sub>O<sub>3</sub> Interlayer”, *ACS Applied Materials & Interfaces* 2015, 7, 26716–26725
28. Klumbies, et al., “Thickness dependent barrier performance of permeation barriers made from atomic layer deposited alumina for organic devices”, Elsevier, *Organic Electronics* 17 (2015) 138–143
29. John Robertson, “High dielectric constant gate oxides for metal oxide Si transistors”, Institute of Physics Publishing, *Rep. Prog. Phys.* 69 (2006) 327–396
30. Ouwens, J. D., et al., “Hydrogen Microstructure in Hydrogenated Amorphous Silicon.”, *Phys. Rev. B: Condens. Matter Mater. Phys.*, 1996, 54, 17759–17762
31. Hyungchul Kim, et al., “Experimental investigation of defect-assisted and intrinsic water vapor permeation through ultrabARRIER films”, *Review of Scientific Instruments* 87, 033902 (2016); doi: 10.1063/1.4942510

32. Yersak, et al., "Characterization of Thin Film Dissolution in Water with in Situ Monitoring of Film Thickness Using Reflectometry", *ACS Applied Materials & Interfaces*, 2016, 8, 17622–17630
33. M. Dragoman, D. Dragoman, "Plasmonics: Applications to nanoscale terahertz and optical devices", *Progress in Quantum Electronics* 32 (2008) 1–41
34. Colson, et al., "Nanosphere Lithography: A Powerful Method for the Controlled Manufacturing of Nanomaterials", *Journal of Nanomaterials* Volume 2013 (2013), Article ID 948510
35. C L Cheung, et al., "Fabrication of nanopillars by nanosphere lithography", *Institute of Physics Publishing, Nanotechnology* 17 (2006) 1339–1343
36. Fredriksson, et al., "Hole–Mask Colloidal Lithography", *Advanced Materials*, 2007, 19, 4297–4302
37. Raghu, et al., "Susceptibility of SiO<sub>2</sub>, ZrO<sub>2</sub>, and HfO<sub>2</sub> Dielectrics to Moisture Contamination", *American Institute of Chemical Engineers Journal*, August 2004 Vol. 50, No. 8, Page 1881

## Citations of Copyrighted Works

### **Figure 1** [fair use]

B. Lee et al., “The use of plasmonics in light beaming and focusing”, *Progress in Quantum Electronics* 34 (2010) 47–87. Fair use determination attached.

### **Figure 2** [fair use]

Stefan A. Maier, “Plasmonics: Fundamentals and Applications”, Published in 2007. Fair use determination attached.

### **Figure 3** [fair use]

Dragoman, “Plasmonics: Applications to nanoscale terahertz and optical devices, *Progress in Quantum Electronics* 32 (2008) 1–41. Fair use determination attached.

### **Figure 4** [fair use]

Moore’s Law over the years. M. Mitchell Waldrop, “The chips are down for Moore’s law”, *Nature News*, Nature Publishing Group, Feb 9, 2016. Used with permission from Nature Publishing Group. License attached

### **Figure 5** [fair use]

Luo, et al., “Surface plasmon resonant interference nanolithography technique”, *Applied Physics Letters*, Vol. 84, No. 23, 7 June 2004. Fair use determination attached.

### **Figure 6** [fair use]

Ramaccia, et al., “Core-shell super-spherical nanoparticles for LSPR-based sensing platforms”, *IEEE Journal of Selected Topics in Quantum Electronics*, Vol. 23, No. 2, March/April 2017. Fair use determination attached.

### **Figure 7** [fair use]

Joachim Fritzsche et al., *Nano Letters* 2016, 16, 7857–7864. Fair use determination attached.

### **Figure 8** [fair use]

Wen-Jeng Ho, et al., “Performance-Enhanced Textured Silicon Solar Cells Based on Plasmonic Light Scattering Using Silver and Indium Nanoparticles”, *Materials* 2015, 8(10), 6668-6676. Fair use determination attached.

**Figure 9** [fair use]

Yersak, et al., “Characterization of Thin Film Dissolution in Water with in Situ Monitoring of Film Thickness Using Reflectometry”, ACS Applied Materials & Interfaces, 2016, 8, 17622–17630. Fair use determination attached.

**Figure 24** [fair use]

Dragoman, “Plasmonics: Applications to nanoscale terahertz and optical devices, Progress in Quantum Electronics 32 (2008) 1–41. Fair use determination attached.

**Figure 25** [fair use]

General Schematics of NSL. “Nanoparticle fabrication by geometrically confined nanosphere lithography”, J. Micro/Nanolith. MEMS MOEMS. 12(3), 031106 (Jul 26, 2013). Fair use determination attached.